Bacteria in Shear Flow

by

Marcos

B. Eng. Mechanical and Production Engineering
Nanyang Technological University, Singapore, 2003
and
M. Eng. Mechanical Engineering
Nanyang Technological University, Singapore, 2005

Submitted to the Department of Mechanical Engineering
in Partial Fulfillment of the Requirements for the Degree of
Doctor of Philosophy in Mechanical Engineering

at the

Massachusetts Institute of Technology

February 2011

Signature of Author .....
Department of Mechanical Engineering
December 31, 2010

Certified by .....
Roman Stocker
Associate Professor of Civil and Environmental Engineering
Thesis Supervisor

.....
Anette Hosoi
Associate Professor of Mechanical Engineering
Chair

Accepted by .....
David E. Hardt
Chairman, Committee on Graduate Students
Department of Mechanical Engineering

This page intentionally left blank.

Bacteria in Shear Flow

by

Marcos

Submitted to the Department of Mechanical Engineering
on December 31, 2010 in partial fulfillment of the requirements for the
degree of Doctor of Philosophy in Mechanical Engineering

Abstract

Bacteria are ubiquitous and play a critical role in many contexts. Their environment is nearly always dynamic due to the prevalence of fluid flow: creeping flow in soil, highly sheared flow in bodily conduits, and turbulent flow in rivers, streams, lakes, and oceans, as well as anthropogenic habitats such as bioreactors, heat exchangers and water supply systems. The presence of flow not only affects how bacteria are transported and dispersed at the macroscale, but also their ability to interact with their local habitat through motility and chemotaxis (the ability to sense and follow chemical gradients), in particular their foraging. Despite the ubiquitous interaction between motility, foraging and flow, almost all studies of bacterial motility have been confined to still fluids.

At the small scales of a bacterium, any natural flow field (e.g. turbulence) is experienced as a linear velocity profile, or 'simple shear'. Therefore, understanding the interaction between a simple shear flow and motility is a critical step towards gaining insight on how the ambient flow favors or hinders microorganisms in their quest for food. In this thesis, I address this important gap by studying the effect of shear on bacteria, using a combination of microfluidic experiments and mathematical modeling.

In chapter 2, a method is presented to create microscale vortices using a microfluidic setup specifically designed to investigate the response of swimming microorganisms. Stable, small-scale vortices were generated in the side-cavity of a microchannel by the shear stress in the main flow. The generation of a vortex was found to depend on the cavity's geometry, in particular its depth, aspect ratio, and opening width. Using video-microscopy, the position and orientation of individual microorganisms swimming in vortices of various intensities were tracked. We applied this setup to the marine bacterium *Pseudoalteromonas haloplanktis*. Under weak flows (shear rates $< 0.1\ s^{-1}$), *P. haloplanktis* exhibited a random swimming pattern. As the shear rate increased, *P. haloplanktis* became more aligned with the flow.

In order to study the detailed hydrodynamic interaction between shear and bacteria, we developed a mathematical model employing resistive force theory. In general, the modeling of a bacterium requires consideration of two factors: the rotating flagellar bundle and the cell body to which the flagella are attached. To make the problem analytically tractable, we study the hydrodynamics around the head and the flagellum separately. In chapter 3, we present a combined theoretical and experimental investigation of the fluid

mechanics of a helix exposed to a shear flow. In addition to classic Jeffery orbits, resistive force theory predicts a drift of the helix across streamlines, perpendicular to the shear plane. The direction of the drift is determined by the direction of the shear and the chirality of the helix. We verify this prediction experimentally using microfluidics, by exposing *Leptospira biflexa flaB* mutant, a non-motile strain of helix-shaped bacteria, to a plane parabolic flow. As the shear in the top and bottom halves of the microchannel has opposite sign, we predict and observe the bacteria in these two regions to drift in opposite directions. The magnitude of the drift is in good quantitative agreement with theory. We show that this setup can be used to separate microscale chiral objects.

In chapter 4, a theoretical and experimental investigation of a swimming bacterium in a shear flow is presented. The presence of the cell body results in a novel phenomenon: chiral forces induce not only a lateral drift, but also a reorienting torque on swimming bacteria. For typical flagellated bacteria, the magnitude of this drift velocity is much smaller (~0.7 $\mu m\ s^{-1}$) than typical swimming speeds of bacteria (~50 $\mu m\ s^{-1}$). However, with the addition of a head, the chirality-dependent forces that lead to a lateral drift also lead to a reorienting torque. The model based on resistive force theory predicts that the drift velocity of swimming bacteria is in the same order of magnitude as the swimming speed. Experimental observations of the motile bacteria *Bacillus subtilis* exposed to shear flows show good agreement with the theoretical prediction. This process is a purely passive hydrodynamic effect, as demonstrated by further experiments showing that bacteria do not behaviorally (i.e. actively) respond to shear.

This newly discovered hydrodynamic reorientation can significantly affect any process that involves changes of swimming direction, so that bacterial 'steering' in a flow cannot be understood unless the effects of chiral reorientation are quantified. Because swimming and reorientation are central to the chemotaxis used by many bacteria for foraging, we expect this coupling of motility and flow to play an important role in the ecology of many bacterial species.

Thesis Supervisor: Roman Stocker
Title: Associate Professor

Acknowledgements

I would like to express my deepest gratitude to my advisor, Professor Roman Stocker, for his patience, enthusiasm, guidance, support, and friendship.

I thank my thesis committee members, Prof. Anette Hosoi, Prof. Pierre Lermusiaux, and Prof. Thomas Powers, for their insights and availability. I thank my collaborator Prof. Henry Fu from whom I learned a great deal about theoretical modeling. His patience, availability, and friendship are greatly appreciated. I thank Prof. Heidi Nepf, Prof. Ole Madsen, Dr. Eric Adams, the present and past members of the Stocker lab, the Environmental Fluid Mechanics Group in the Parsons Lab, and the HSP group for their comments and insights.

I would also like to thank Dr. Benjamin Kirkup, Dr. Justin Seymour, and Mr. Michael Couter for their guidance in microbiology. I thank Dr. Mathieu Picardeau for providing me Spirochetes *Leptospira biflexa* and Dr. George Glekas for providing me bacteria *Bacillus subtilis* used in the experiments of this work. Their help are greatly appreciated.

I would like to extend my appreciation to Dr. David Gonzalez-Rodriguez and Dr. Raymond Lam for many fruitful discussions. I thank my UROP student, Mr. Wesley Koo for a fun working experience together. I would also like to thank Mr. Scott Stransky for developing BacTrack, the particle tracking software used in this thesis.

I would like to thank Ms. Leslie Regan, Ms. Sheila Anderson, Ms. Victoria Murphy, and Mr. James Long for their professionalism, dedication, kindness, and help.

The financial support of the Martin Family Society Fellowship and the National Science Foundation under Grant Number OCE-0744641-CAREER (to Roman Stocker) are gratefully acknowledged.

I also thank all my friends at MIT, especially Aaron Chow, Crystal Ng, David Gonzalez-Rodriguez, Denvid Lau, Lawrence David, Piyatida Hoisungwan, Raymond Lam, and Yukie Tanino, for their support and for the enjoyable times we have spent together. Finally, I would like to dedicate this thesis to my parents, Sutina and Jaman, who always believe in me and provide me with ceaseless support.

This page intentionally left blank.

Contents

1 Introduction 15

2 Bacteria swimming in microvortices 20

2.1 Materials and procedures 20

2.1.1 Fabrication 20

2.1.2 Microchannel geometry 21

2.1.3 Experimental setup 21

2.1.4 Numerical modeling 22

2.1.5 Microorganisms 22

2.2 Assessment and discussion 22

2.2.1 Generation of a vortex 22

2.2.2 Effects of the cavity geometry 23

2.2.3 Trajectories and orientation of swimming microorganisms 25

2.3 Summary 28

3 Helix in shear 29

3.1 Model formulation 29

3.1.1 A rigid straight rod in shear flow 30

3.1.2 Helix in a shear flow 32

3.2 Experimental verification 37

3.2.1 Experimental setup 37

3.2.2 Experimental results and discussion 38

3.2.3 Comparison with theory 40

3.3 Application to chiral separation 42

3.4 Summary 44

4 Bacteria swimming in a shear flow 45

4.1 Model formulation 45

4.2 The effect of tumbling 52

4.3 Experimental verification 55

4.3.1 Experimental setup 55

4.3.2 Experimental results and discussion 56

4.4 Modeling cell head elongation and "wiggling" 59

4.5 Bacteria active response to shear 63

4.6 Summary 65

5 Summary and conclusion 66

Bibliography 68

Appendix 75

List of Figures

Figure 2-1. Geometry of the microchannel. Gravity is in the $-z$ direction (into the plane). The cavity and the channel have the same depth, H. The dashed line shows the field of view where microorganisms are tracked. Mean velocity in the main channel is U_F; characteristic velocity inside the cavity is U_C. (Marcos and Stocker 2006).....21

Figure 2-2. Schematic of the experimental setup. The microchannel is set on the stage of an inverted microscope and flow is driven by a syringe pump. Microorganisms in the cavity are imaged with a CCD camera. (Marcos and Stocker 2006).....21

Figure 2-3. The flow in a cavity of aspect ratio $\alpha = 1$, main flow speed $U_F = 21.4$ mm s^{-1}. The characteristic velocity in the cavity is $U_C = 363$ μm s^{-1}. Lengths of the cavity and the opening are $a = 200$ μm and $g = 120$ μm, respectively. Flow is from left to right. The cavity Reynolds number ($U_C\, a/\nu$) is 0.07. (a) Trajectories of 2 μm beads. The solid white line shows the outline of the channel. (b) Numerical streamlines at the mid-depth plane ($z = H/2 = 65$ μm). Imperfections in the streamlines result from small numerical errors in integrating the velocity field. (Marcos and Stocker 2006).....23

Figure 2-4. Velocity inside the cavity in the x – direction, as a function of the transverse position y (dashed line in the inset) for $U_C = 363$ μm s^{-1}. Experiments (circles) are compared with numerical results (solid line). (Marcos and Stocker 2006). 23

Figure 2-5. Numerical streamlines for $U_F = 21.4$ μm s^{-1} and two different depths: (a) $H = 70$ μm; (b) $H = 90$ μm. All other dimensions are as in Fig. 3. Crossing streamlines visible in panel (a) reflect small three-dimensional effects. 24

Figure 2-6. Two configurations in which no vortex formed, as shown by the trajectories of 2-μm beads: (a) $\alpha = 1$, $g = a = 200$ μm; (b) $\alpha = 2$, $g = a/2 = 200$ μm. For both cases, $H = 130$ μm and $U_F = 21.4$ mm s^{-1}. The scale is the same in the two panels. 24

Figure 2-7. Trajectories of the bacteria *P. haloplanktis* in vortices of different strength: (a) No flow; (b) $U_C = 36.3$ μm s^{-1}; (c) $U_C = 363$ μm s^{-1}. The field of view is shown in Fig. 1; (d) and (e) are magnified views of selected trajectories, showing the instantaneous orientations of individual bacteria; (f) A bacterium's orientation is further magnified to highlight misalignment with the direction of travel.....25

Figure 2-8. Trajectories of the alga *D. tertiolecta* swimming in the cavity: (a) No flow; (b) $U_C = 363$ μm s^{-1}. The field of view is shown in Fig. 2-1. The black spot inside each alga is a result of phase contrast microscopy. 26

Figure 2-9. The average streamline crossing angle of *P. haloplanktis* swimming in a microvortex under various shear rates. The size of the analysis region (blue box, upper inset) is chosen arbitrarily within the field of view. The shear rate is averaged over the

region of analysis. Red filled circles are the data obtained from the region of analysis. Green and yellow crosses are the data obtained by increasing and decreasing the region of analysis by 20%. The lower inset shows the definition of streamline crossing angle $\Delta\theta$....28

Figure 3-1. Schematic of a straight rod in a simple shear flow.....30

Figure 3-2. Schematic of helix in a body fixed frame *OXYZ*.....32

Figure 3-3. Euler angles describing the body orientation. The arrow represents the major axis of the body. 33

Figure 3-4. Schematic of a right-handed helix in simple shear flow. Red shading and black shading show the top and bottom halves of the helix. Upper inset: The net force acting on one pitch of the helix is along $-z$. Lower inset: Predicted normalized drift velocity v/v_0 versus helix orientation θ. θ is the angle between a helix in the x-y plane and the flow, and v_0 is the drift velocity of a helix aligned with the flow ($\theta = 0$, $\psi = \pi/2$). (Marcos et al. 2009). 35

Figure 3-5. Predicted lateral drift of a right-handed helix in simple shear flow in the absence of Brownian motion. The number of full turns is $n = 25$, pitch angle $\alpha = 45^{\circ}$, total contour length $l = 14.1$ μm, and we assumed $\zeta_{\perp}/\zeta_{//} = 2$. The helix is initially at (0,0,0) and pointing along the x axis ($\theta = 0$, $\psi = \pi/2$).....36

Figure 3-6. (a) Scanning electron micrograph (SEM) of *L. biflexa* flaB mutant, with typical dimensions (inset). The bent configuration is a result of SEM preparation and live organisms are nearly always straight. (b) Microchannel design with separate inlets for spirochetes and buffer. The color-coded squares refer to the locations of data collection (Fig. 3-7b). (c) Schematic of the separation process (for right-handed helices) in the microchannel ($W = 1$ mm, $H = 90$ μm, $w \approx 100$ μm). The lateral drift direction depends on the sign of the shear $\dot{\gamma}$, resulting in divergence of top and bottom streams. (Marcos et al. 2009). 37

Figure 3-7. Observed spirochete distributions across the channel width for (a) $x = 2$ cm and (c) $x = 107.5$ cm. Orange, black, and blue correspond to the top, mid, and bottom depths. The midpoint of each rectangle corresponds to the mean position ($\bar{z}$) of the distribution, while the half-width is 2 standard deviations (2σ). b) Probability distribution function, obtained from fifty images at each location, for various distances x along the channel. Over 10,000 spirochetes were imaged for each location x, y. The broadening of the population distribution is accounted for by the finite depth of focus of the imaging system, combined with variation of shear (hence, drift) with depth. (Marcos et al. 2009). 38

Figure 3-8. The standard deviation σ of the spirochete distribution versus distance x in the microchannel. Circles are experimental data, color-coded according to depth as in Fig. 3-6c. Solid and dashed lines refer to values calculated with a depth of focus $\delta = 10$ μm and 14 μm, respectively, while green and red lines correspond to $y = H/4$ (or, equivalently, $y = -H/4$) and $y = 0$, respectively. (Marcos et al. 2009).....39

Figure 3-9. Experimental quantification of spirochete distribution: a) Average lateral position at top, mid, and bottom depths, and b) separation between top and bottom populations, as a function of distance x along the channel. c) Hypothetical separation efficiency. In a), b), and c), full circles are data from spirochetes, lines are linear fits, and empty squares are control data from spherical beads. (Marcos et al. 2009). 40

Figure 3-10. The effect of the polar angle ψ on the drift velocity v. v_0 is the drift velocity of a helix aligned with the flow ($\theta = 0$; $\psi = \pi/2$). (Marcos et al. 2009). 41

Figure 3-11. Size limit for separation of isometric helices of length L and equivalent aspect ratio r = 70. Dashed contours show constant Re (spaced by a factor of 10) and the thick contour is Re = 0.1. Solid contours show constant Pe. The gray scale shows $\bar{v}/v_0$, where v_0 is the drift velocity of a helix aligned with the flow. The smallest helices which can be separated for a given shear rate, determined by $\bar{v}/v_0 = 0.66$ (Pe = 50, marked by circle on inset) and Re < 0.1, have $L \approx 20$ (square), 80 (circle), and 400 nm (diamond) for $\dot{\gamma} = 10^8$, 10^6, and 10^4 s^{-1}, respectively. Full symbols mark the parameter regimes of our experiments: Re = 0.03 (triangle) and Re = 5 (hexagon). Inset: $\bar{v}/v_0$ vs Pe. (Marcos et al. 2009).....43

Figure 4-1. Schematic of a bacterium in a simple shear flow. 45

Figure 4-2. Sketch showing the center of the helix (H) and the center of the sphere (S), which are separated by a distance $\Delta\mathbf{r}$ in 3D space. p is a general point on the helix.....46

Figure 4-3. a) The chirality-induced lateral drift force on a right-handed helical flagellum and the drag on the cell head lead to a reorienting torque on a bacterium. b) This chiral torque causes a swimming bacterium to preferentially point away from the x direction and thus to experience a net drift velocity V that is of the same order as the swimming velocity U. 49

Figure 4-4. Net drift velocity (V) of a population of swimming bacteria (black solid line), swimming ellipsoids (blue dashed line), and non-swimming bacteria (red dotted line) in a simple shear flow. The drift velocities of the three populations were normalized with the swimming speed of bacteria (U = 50 μm/s). The bacteria were modeled by assuming a 1 μm radius spherical head and a left-handed helical flagellum with 4 turns, pitch angle of 41°, and axial length of 10 μm, corresponding to the flagellar bundle of *E. coli*. For swimming bacteria, the angular rotation rate of the flagellum relative to the cell body ω_{rel} = 127 Hz. 50

Figure 4-5. Effects of cell swimming speed on the net drift velocity (normalized with average swimming speed) under various shear rates. The model assumes a 0.2 μm radius spherical head and a left-handed helical flagellum with 3 turns, pitch angle of 37°, and axial length of 6 μm, corresponding to the flagellar bundle *B. subtilis*. 51

Figure 4-6. Effect of head size on the net drift velocity, normalized with the swimming speed U, as a function of the shear rate. The model assumes a left-handed helical flagellum

with 3 turns, pitch angle of 37°, and axial length of 6 μm, corresponding to the flagellar bundle of *B. subtilis*. In all cases, U = 50 μm/s.....52

Figure 4-7. The effect of tumbles on the drift velocity. The net drift velocity (V) of a population of smooth- swimming bacteria (black) and run-and-tumble bacteria (blue). Effects of Brownian rotation are included in the model. The bacteria were modeled by assuming a 0.4 μm radius spherical head and a left-handed helical flagellum with 3 turns, pitch angle of 37°, and axial length of 6 μm, corresponding to the flagellar bundle of *B. subtilis*. The angular rotation rate of the flagellum relative to the cell body ω_{rel} = 250 Hz, giving swimming speed U = 50 μm/s. The run-and-tumble swimmer had an average change direction of 68° and a standard deviation of 39° with mean run time τ = 1 s. 54

Figure 4-8. (a) Schematic of the chiral reorientation process at a quarter depth in the channel, i.e. $y = -H/4$, for a left-handed flagellum. The microchannel had width W = 1 mm, height H = 90 μm. (b) Microchannel design showing inlet and outlet. Note that only one inlet was used in this experiment. The square refers to the location of data collection and was located 110 cm downstream of the inlet. (c) Two sample trajectories of *B. subtilis* bacteria in a shear flow, imaged at $y = -H/4$. The center of the colored circles corresponds to the locations obtained by the image processing routine. 56

Figure 4-9. Net drift velocity of *B. subtilis* OI4139 under various shear rates at $y = -H/4$, normalized by the mean average swimming speed U = 55 μm s^{-1}. Each set of colored squares indicates a separate batch of bacteria. Six replicates were performed. Solid lines refer to the theoretical prediction assuming a left-handed helical flagellum with 3 turns, pitch angle of 37°, and axial length of 6 μm, and a spherical head of radius 0.4 μm (black line) and 0.8 μm (blue line).....56

Figure 4-10. Net drift velocity of *B. subtilis* OI4139 under various shear rates at $y = H/4$ and $y = -H/4$, normalized by the mean average swimming speed U = 55 μm s^{-1}. Since the shear rates between the top and bottom layer are opposite in sign, we present the absolute values of the shear rate. Two separate sets of experiments (light and dark colors) were conducted at $y = H/4$ (red) and $y = -H/4$ (green). For each case, two replicates were performed. The two experiments at $y = -H/4$ were performed in addition to the ones shown in Fig. 4-9. 57

Figure 4-11. Swimming trajectory of *B. subtilis* OI4139 in the absence of flow. Several trajectories show a helical pattern, visualized as a sinusoidal path when viewed from the top.....58

Figure 4-12. Schematic of a generalized swimmers, based on three spheres to model an elongated cell head and on an off-axis flagellar bundle, which induces wiggling. Angle AA denotes the contact point between cell body and the flagellar bundle. Lower inset: Angles BB and CC are the polar and azimuthal angles of the flagellar bundle (thick green arrow) relative to the cell body (body fixed frame *OXYZ*).....59

Figure 4-13. Wiggling in the trajectory of a swimming bacterium in the absence of flow. The ellipsoid represents the cell head of the bacterium. The flagellar bundle is offset relative to the cell body axis by 18°. The red point shows the initial position of the bacterium at the start of the simulation and the solid line shows that trajectory of the center of the middle sphere. The inset shows the trajectory as viewed from the top. The model assumes a left-handed helical flagellum with 3 turns, pitch angle of 37°, and axial length of 6 μm, corresponding to *B. subtilis* flagellar bundle and a cell head made of three spherical heads of radius 0.5 μm. The three angles determining the flagella bundle offset are AA = CC = 0 and BB = 18°. Brownian motion was neglected in this simulation. 62

Figure 4-14. Effects of elongation and wiggle on the net drift velocity. The model assumes a left-handed helical flagellum with 3 turns, pitch angle of 37°, and axial length of 6 μm. The black line shows the theoretical prediction that agrees well with the experimental data (see Fig. 4-9). The 3-sphere model was calculated using 3 identical spheres of radius 0.5 μm (cyan). The three angles determining the flagellar bundle offset are AA = CC = 0 and BB = 5° (red). 63

Figure 4-15. Time evolution of the mean swimming speed of a bacterial population after exposure to a shear rate of 500 s^{-1} for 9 minutes. Colors refer to *Pseudoalteromonas haloplanktis* (blue), *Bacillus subtilis* (black), *Escherichia coli* (green), and *Pseudomonas aeruginosa* (red). Solid lines refer to the values before shear exposure. 64

List of Tables

Table 2-1. The influence of advection on P. haloplanktis and D. tertiolecta in vortices of various strengths. An equivalent dissipation rate ε is calculated based on UC. Symbols indicate the importance of advection by the vortex over motility as inferred from trajectories, from '++' (advection dominates) to '- -' (motility dominates). 27

Table 3-1. Comparison of $\overline{v} / v_0$ between 2D and 3D models. v_0 is the drift velocity of a helix aligned with the flow ($\theta = 0$, $\psi = \pi/2$). (Marcos et al. 2009).....42

Chapter 1

Introduction

Microorganisms are ubiquitous in the environment. Despite their tiny size, their combined biomass is enormous. The functions performed by microorganisms play a critical role in nearly every environment (Weeks and Alcamo 2008). In soil, almost every chemical transformation involves active contributions from microorganisms. In particular, microbes play a fundamental role in soil fertilization by mediating the cycle of nutrients like carbon and nitrogen, which are crucial for plant growth (Wheelis 2008). In the ocean, microorganisms are important not only because they form the base of the marine food web, but also because they drive biogeochemical cycles, including carbon, nitrogen, sulfur and iron (Willey et al. 2008). Their activities can affect local meteorological patterns and potentially influence changes in global climate. Other microorganisms are pathogenic and negatively affect humans, such as *Salmonella*, which contaminates water supply systems, or *Helicobacter,* which gives ulcers, or *Pseudomonas*, implicated in cystic fibrosis (Willey et al. 2008). Many species of bacteria form biofilms, surface-attached microbial colonies encased in a polymeric matrix, which arise on nearly every surface in a wide range of environments and cause huge economics losses resulting from equipment damage, product contamination, and energy dissipation (Hui 2006).

Microbes nearly always inhabit a dynamic environment and are exposed to a range of flow conditions: creeping flow in soil, highly sheared flow in bodily conduits, and turbulent flow in rivers, streams, lakes, and oceans, as well as in anthropogenic habitats such as bioreactors, heat exchangers, and water supply systems. The presence of flow not only affects how microorganisms are transported and dispersed at the macroscale, but also their ability to interact with their local habitat through motility and chemotaxis (the ability to sense and follow chemical gradients), in particular their foraging. For example, the development of biofilms in pipes and channels depends on the flow conditions (primarily shear) at the surface on which the biofilm lives. For free-living (or 'planktonic') microorganisms, motility has evolved as an important trait in escaping predators, finding refuges and exploring new environments. Most importantly, microbes swim to take advantage of spatially heterogeneous nutrient sources, which are often patchy down to scales of micrometers (Azam 1998; Blackburn et al. 1998; Seymour et al. 2000; Stocker et al. 2008).

Many microorganisms use one or more appendages to swim. At the length scales of microorganisms, the inertia of both the cell and the fluid is unimportant and viscous effects dominate: the Reynolds number is very low. The Reynolds number is a dimensionless quantity defined as $\mathrm{Re} = \rho UL/\mu$, where ρ and μ are the density and dynamic viscosity of the fluid, respectively, and U and L are the velocity and length scales of the flow, respectively. In water ($\rho \approx 1000$ kg m^{-3}, $\mu \approx 10^{-3}$ kg m^{-1}s^{-1}), a swimming bacterium such as *Escherichia coli* with $U \approx 10$ μm s^{-1} and $L \approx 1$–10 μm has a Reynolds number $\mathrm{Re} \approx 10^{-5}$–

10^{-4}. A human spermatozoon with $U \approx 200$ μm $s^{-1}$and $L \approx 50$ μm moves with Re $\approx 10^{-2}$ (Brennen and Winet 1977; Lauga and Powers 2009). Given the smallness of the inertial effects, it is appropriate to study bacterial fluid dynamics in the limit of zero Reynolds number, for which the governing equations of fluid motion are the Stokes equations

$$-\nabla p + \mu \nabla^2 \mathbf{u} = 0, \qquad \nabla \cdot \mathbf{u} = 0, \tag{1.1}$$

where $\mathbf{u}$ and p are the velocity and pressure of the fluid.

Since Eq. (1.1) is linear, hydrodynamic forces are linearly related to the flow velocities. In addition to this linearity, one other important property in Stokes flow is drag anisotropy, a crucial ingredient for biological locomotion at zero Reynolds number (Hancock 1953; Lauga and Powers 2009). For example, at low Reynolds number a rod has more resistance when moving perpendicular rather than parallel to the flow. Therefore, to obtain the same velocity, moving the rod in the perpendicular direction requires more applied force than moving it in the parallel direction.

The linear and time-independent nature of the Stokes equations lead to kinematic reversibility (Happel and Brenner 1965), where the distance travelled by a swimmer does not depend on the rate of the motion, but only on the geometrical motion itself. Furthermore, if the sequence of motions displayed by a swimmer in a time-periodic fashion is identical when viewed after a time-reversal transformation, then the swimmer cannot move on average. This property is also known as the 'scallop theorem', where reciprocal motion, such as a clapping scallop that opens and closes its shell periodically, generates no net motion (Purcell 1977; Lauga and Powers 2009). Therefore, in order to swim in the low Reynolds number regime, microorganisms must adopt non-reciprocal body motions. Well-known examples include sperm cells, which swim by sending traveling waves of bending down flexible flagella (Bray 2001), and bacteria, which swim by rotating helical flagella (Berg 2004). The detailed morphology of bacterial flagella varies from one species to another (Fujii et al. 2008). For example, *Escherichia coli* forms a left-handed helical flagellar bundle with 4 turns, a pitch angle of 41°, and an axial length of 10 μm. *Bacillus subtilis* forms a 3-turn left-handed helical bundle, with a pitch angle of 37° and an axial length of 6 μm (Fujii et al. 2008).

Wild-type swimming bacteria, such as *E. coli* and *B. subtilis*, typically display a so-called 'run-and-tumble' swimming behaviour (Berg 2004). During runs, the bacterium swims along a roughly straight path, and its flagellar filaments are bundled together tightly behind the cell. During a tumbling event, the flagella come out of the bundle, resulting in a random reorientation of the cell before the next run. In the absence of chemical gradients, a bacterium's trajectory has many characteristics of a random walk. In the presence of chemical gradients, bacteria are able to swim up/down the gradients (i.e. performing positive/negative chemotaxis) by biasing their random walk. When bacteria move towards a food source, they prolong the duration of runs in that direction (or, equivalently, tumble less often when going in the right direction). This allows them to head towards the food source, with a net drift velocity or 'chemotactic velocity'. The chemotactic velocity

typically ranges between 6-23% of the swimming speed, but can be as high as 35% (Ahmed et al. 2010b).

In addition to chemical gradients, the life of microorganisms is governed by flow. A naïve treatment would only consider flow as a source of advection, which transports bacteria along streamlines. However, fluid flow also involves velocity gradients (i.e. shear), which could significantly alter bacterial swimming trajectories. The shear intensity varies from one environment to another. For example, the shear rate can be as large as 1 s^{-1} in the open ocean (Lazier and Mann 1989) and in lakes (MacIntyre et al. 1999, 2002), ~ 4 s^{-1} in the coastal ocean (Kunze et al. 2006), ~ 20 s^{-1} in human's gastric tract (Kozu et al. 2010), and shear rates above 40 s^{-1} are usually found in engineered water treatment systems (Crittenden et al. 2005).

At low Reynolds number shear flows, objects undergo periodic rotations known as Jeffery orbits (Jeffery 1922): a sphere rotates with constant angular velocity, whereas for an elongated body, the velocity depends on orientation. The more elongated a body, the longer its relative residence time when aligned with streamlines. Non-chiral objects, such as spheres and ellipsoids, follow streamlines in a low Reynolds number shear flow (Jeffery 1922). On the other hand, chiral objects, such as helices, drift across streamlines when exposed to shear (Brenner 1964; Kim and Rae 1991; Makino and Doi 2005; Marcos et al. 2009). The interaction between the morphology of microbes and a shear flow is therefore important in determining swimming trajectories, in particular the ability of bacteria to swim across streamlines.

Despite the ubiquitous presence of flow in the environment of microorganisms, very few studies have focused on the hydrodynamic interaction between flow and swimming in microbes. The existing studies are prevalently numerical. It was shown that bacteria can cluster around phytoplankton cells (Bowen et al. 1993; Luchsinger et al. 1999) and around sinking aggregates such as marine snow particles (Kiørboe and Jackson 2001). Meanwhile, solution of the stochastic evolution equations for a bacterial population (Bearon and Pedley 2000; Bearon 2003; Locsei and Pedley 2008) has shown that reorientation due to Jeffery orbits can render run-and-tumble chemotaxis ineffective at high shear rates (Locsei and Pedley 2008). However, in these studies, bacteria were simply modeled as either spheres (Bowen et al. 1993; Kiørboe and Jackson 2001) or ellipsoids (Luchsinger et al. 1999; Locsei and Pedley 2009), neglecting the detailed morphology of bacterial cells, and thus chirality.

A small number of studies have considered the effects of flow on microbial motility. Among these are the discovery of rheotaxis in spermatozoa (Bretherton and Rothschild 1961) and gyrotaxis in biflagellated swimming algae (Kessler 1985). Rheotaxis refers to the tendency of organisms to align with the direction of flow. The organism exhibits a positive/negative rheotaxis when its head points upstream/downstream, respectively. For example, in a horizontal Poiseuille flow, live spermatozoa have been observed to exhibit positive rheotaxis (Bretherton and Rothschild 1961). Rheotaxis can be either a hydrodynamic or a behavioral effect. Gyrotaxis is a process in which the preferred orientation of a bottom-heavy cell is determined by a balance between the viscous torque

and the gravitational torque. Due to gyrotaxis, in a downward cylindrical Poiseuille flow, uniformly suspended algae swim towards the axis of the tube, whereas they swim toward the periphery in an upward flow (Kessler 1985).

Other examples of the effect of flow on microbial motility concern phytoplankton and spermatozoa. Using a Taylor-Couette apparatus, it was found that the orientation of swimming dinoflagellates in a shear flow was significantly different from random, with a preferential alignment at an angle with the flow (Karp-Boss et al. 2000). This observation was rationalized as differences in drag forces on the body and flagella (Karp-Boss et al. 2000). Other studies found that fertilization success in the purple sea urchin depends on intensity of the shear (Mead and Denny 1995; Riffel and Zimmer 2007). Low shear rates improve fertilization through mixing enhancement and thus increasing the encounter rates between sperms and eggs. On the other hand, large shear rates overwhelm the sperm's ability to reach the egg. (Riffel and Zimmer 2007).

It has been known for some time that surfaces affect how nearby bacteria swim, giving rise to circular trajectories in horizontally unconfined environments, or the "swimming on the right" behavior in microchannels (Ramia et al. 1993; DiLuzio et al. 2005; Lauga et al. 2006). The circles result from the cell body and flagella rolling along the surface in opposite directions, creating a torque that makes the cell swim in circular trajectories (Lauga et al. 2006). In the presence of shear, this behaviour changes drastically: *E. coli* were found to swim upstream in a microfluidic channel under shear flow (Hill et al. 2007). This ability to swim upstream could be crucial in colonizing urinary tracts, causing infection. These studies demonstrated that novel processes are uncovered and important new insight is gained by 'simply adding flow' to the microbial world.

Most techniques used to date do not allow direct observation of bacterial movement patterns in flow, due to the difficulty in setting up accurate and controllable flow fields while visualizing and quantifying the microorganisms' response. Here we propose that microfluidics enables one to work at the appropriate scales, both in terms of the manipulation of flow, as well as the direct visualization of how microorganisms are affected by flow.

Microfluidics has triggered important advances in a range of fields, from cellomics to chemical engineering, due to the opportunity to carefully control geometries, flows and chemical gradients, while observing the response of the system at the scale of micrometers (Whitesides et al. 2001; Marcos and Stocker 2006; Seymour et al. 2007). Yet, the application of microfluidics to understand fundamental interactions between flow and swimming microorganisms has been lagging. This thesis takes a first step in this direction by exploiting microfluidics to study the effects of shear on bacteria.

This research began with the use of microfluidic technology to understand the response of microorganisms, such as bacteria and algae, to a highly simplified model turbulent environment. At the small scales of these organisms, turbulence is experienced simply as shear: understanding the interaction between shear and swimming is then a critical step towards gaining insight in how the ambient flow favors or hinders microorganisms in their

quest for food. Realizing that microbial morphology plays an important role, this thesis seeks to understand the hydrodynamic interaction between shear and shape in the bacterial world.

The goal of this thesis is to investigate the role of flow on the motility of bacteria, both experimentally and theoretically. The specific aims of this research were to:

1. Develop a mathematical model of a swimming bacterium in a shear flow.
2. Design and carry out experiments to study the effect of shear on bacterial motility.
3. Investigate whether bacteria display a behavioural response to hydrodynamic shear, as evidence that they can sense hydrodynamic shear.

In chapter 2, we develop a new method to generate microscale vortices (akin to the smallest components of turbulence in the ocean) using a microfluidic setup, with accurate control and visualization of the flow. We discuss the effects of vortex strength on the swimming of marine bacteria and algae.

In chapter 3, we develop a mathematical model employing resistive force theory to study the hydrodynamic effect of shear on a rigid, non-swimming helix, relevant to the helical shape of bacterial flagella and some species of microorganisms, such as *spirochetes* and *Spirulina*. An experimental verification of the theory by exposing the non-motile, helically shaped bacteria *Leptospira biflexa flaB* mutant to shear in a microfluidic channel is given.

We present the full model of bacteria swimming in a shear flow in chapter 4. We discuss the role of randomness in swimming and the effect of cell size on the cell's ability to swim across streamlines. A set of experiments is presented to verify the model by exposing the smooth swimming bacterium *Bacillus subtilis* OI4139 to a microfluidic shear flow. Finally, to confirm whether the observations are the result of purely hydrodynamics effects, we present a separate experiment to probe the bacteria's ability to actively respond to shear.

Chapter 2

Bacteria swimming in microvortices

Eddies at the Kolmogorov scale (e.g. Yamazaki et al. 2002) are the smallest remnants of the turbulent cascade in the ocean, with time scales in the order of 1-100 s, depending on the intensity of turbulence (Karp-Boss et al. 1996). Kolmogorov eddies represent fluid motion at the scale most directly relevant to microbial dynamics, affecting nutrient redistribution by shear (Bowen et al. 1993; Luchsinger et al. 1999), encounter rates with predators and nutrient patches (Rothschild and Osborn 1988), and the ability of microorganisms to swim and chemotactically orient in the flow. Quantitative experimental information on microbial dynamics at these scales is still lacking. We propose to use microfluidics as a first step in understanding the response of microorganisms to microscale vortices. The generation of vortices at small Reynolds numbers has been investigated both experimentally and numerically (Higdon 1985; Shen and Floryan 1985). At the microscale, great attention has been devoted to flows that enhance mixing (e.g.: Liu et al. 2000; Stroock et al. 2002), but the time-scales do not reflect those relevant in the environment (e.g. Shelby et al. 2003). Yu et al. (2005) used side cavities to generate vortices in microchannels and mapped out the regime in which flow separation is to be expected. Here we apply a similar technique to generate stable microvortices on scales relevant to microbial dynamics in the aquatic environment, and show that we can obtain detailed information on the microorganisms' response.

2.1 Materials and procedures

2.1.1 Fabrication

Channels were fabricated using soft lithography (Whitesides et al. 2001, Seymour et al. 2007). Fabrication begins by creating a blueprint for the microchannels using computer-aided design (CAD) software and printing it on transparency film with a high-resolution image setter to create a 'mask' (Fineline Imaging, Colorado Springs, CO). A silicon wafer is spin-coated with a layer of negative photoresist (SU8-2100, MicroChem, Newton, MA), the thickness of which corresponds to the final depth of the channels. With the mask laid on the coated wafer, the latter is exposed to UV light, polymerizing exposed regions of the photoresist. After dissolving the unpolymerized photoresist, the channel structure is left on the wafer (the 'master'). The soft polymer polydimethylsiloxane (PDMS, Sylgard 184; Dow Corning, Midland, MI) is prepared according to the manufacturer's instructions and poured on the master to cast PDMS channels. After curing the PDMS by baking for 12 h at 65°C, the PDMS layer containing the channels is peeled off from the master, and holes for inlets and outlets are punched with a gauge 16, sharpened luer tip. Finally, channels are bonded to a glass slide after treating both the PDMS layer and the glass slide with oxygen plasma for 1 min (HARRICK Plasma Cleaner/Sterilizer, Harrick Scientific, Ossing, NY).

2.1.2 Microchannel geometry

The channel has a rectangular cross section of width W and a rectangular side cavity of length a and width b (Fig. 1). The depth, H, is the same for the main channel and the cavity. Differently from Yu et al. (2005), we partially closed the area between the cavity and the main channel, leaving an opening of length g. In our basic configuration, L = 10 mm, a = W = 200 μm, H = 130 μm, d = 25 μm, g = 120 μm, and the cavity aspect ratio $\alpha = a/(b+d)$ = 1. We also considered two additional configurations, g = a = 200 μm and α = 2, respectively.

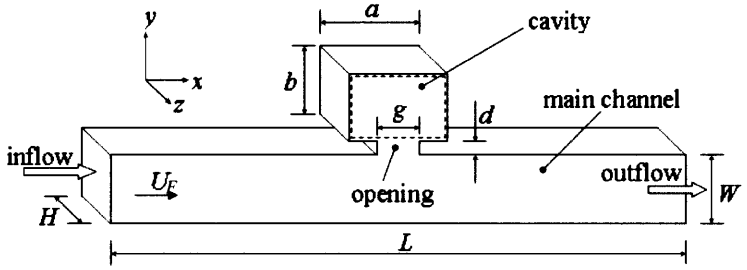

Figure 2-1. Geometry of the microchannel. Gravity is in the $-z$ direction (into the plane). The cavity and the channel have the same depth, H. The dashed line shows the field of view where microorganisms are tracked. Mean velocity in the main channel is U_F; characteristic velocity inside the cavity is U_C. (Marcos and Stocker 2006).

2.1.3 Experimental setup

The microchannel was set on the stage of a Nikon Eclipse TE2000-E inverted microscope (Nikon, Japan). PEEK tubing (0.762 mm ID, 1.59 mm OD, Upchurch Scientific, Oak Harbor, WA) was used to connect the inlet to a 10 mL syringe (BD Luer-Lok Tip) via a fitting (Part P-704-01, Upchurch Scientific, Oak Harbor, WA) and the outlet to a constant-depth reservoir, to avoid capillary and gravity effects (Fig. 2-2). A constant flow rate in the main channel was generated using a syringe pump (PHD 2000 Programmable, Harvard Apparatus, Holliston, MA). For the appropriate geometrical configuration, the shear stress of the main flow produced a vortex in the cavity of strength proportional to the mean velocity U_F in the main channel.

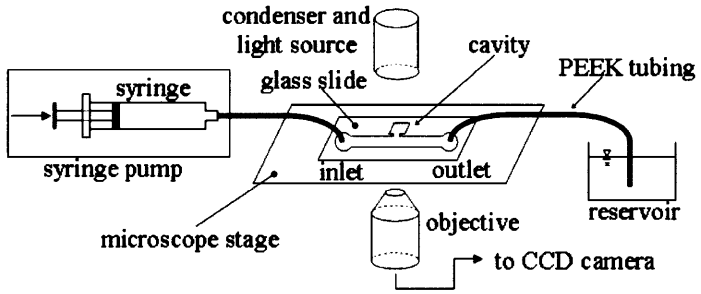

Figure 2-2. Schematic of the experimental setup. The microchannel is set on the stage of an inverted microscope and flow is driven by a syringe pump. Microorganisms in the cavity are imaged with a CCD camera. (Marcos and Stocker 2006).

The flow field within the channel was visualized using 2-μm diameter beads (Polysciences, Warrington, PA). Phase contrast was used to image the beads and the microorganisms,

with long-working-distance 20× (NA = 0.45) and 40× (NA = 0.6) objectives. The depth of field can be calculated following Meinhart et al. (2000): for 2-μm beads, we obtained 28 μm (20×) and 19 μm (40×). Sequences of images ('movies') were captured with a 1600 × 1200 pixels, 14 bit, cooled CCD camera (pixel size 7.4 × 7.4 μm^2; PCO 1600, Cooke, Romulus, MI) at 30 to 62 frames s^{-1} and processed using IPLab software (Scanalytics, Fairfax, VA). In the images, beads or microorganisms appear as bright regions on a darker background. Images of the trajectories were obtained by assigning to each pixel the maximum light intensity recorded in that pixel over the duration of the movie (*3D Time Stacked View* command in IPLab).

2.1.4 Numerical modeling

For preliminary screening of a range of design configurations, as well as for accurate characterization of the flow field, we carried out a computational fluid dynamics simulation of the cavity flow. We used the finite-element code Comsol Multiphysics (Burlington, MA) to solve the steady-state Navier-Stokes equations in three-dimensional space. The model geometry was that described above, except for L = 1 mm to save computational time (we verified that the flow field in the cavity is the same as for L = 10 mm). The boundary conditions were no-slip on all solid boundaries, uniform velocity at the inflow and zero pressure at the outflow. We adopted a multigrid solver using between 13,000 and 22,000 elements, each at most 30 μm in size.

2.1.5 Microorganisms

The marine bacterium *Pseudoalteromonas haloplanktis* (2 μm length) was grown to exponential phase in 1% Tryptic Soy Broth (TSB) at room temperature, before being diluted 1:10 in Artificial Seawater. Experiments were performed 72 hours later. The motile marine alga *Dunaliella tertiolecta* (5 μm diameter) was grown to exponential phase in f/2 medium.

2.2 Assessment and discussion

2.2.1 Generation of a vortex

Using the setup described above we were able to generate a stable and reproducible vortex in a cavity of aspect ratio α = 1 (Fig. 2-3a). The numerical streamlines (Fig. 3b) closely match the experimental trajectories, as expected for a steady flow. Good agreement is further demonstrated by comparing the velocity measured experimentally at different locations in the cavity with its numerical counterpart (Fig. 2-4). We can therefore use the numerical model to investigate the vortex in more detail. For our geometry, the maximum velocity in the cavity is U_C = 1.7% U_F for a main-channel Reynolds number Re = $U_F W/\nu$ < 6 (where ν is the kinematic viscosity), corresponding to U_F < 30 mm s^{-1}. In contrast to higher Reynolds number designs (e.g. Shelby et al. 2003), generation of the vortex does not rely on inertial effects. While the flow inside the cavity is in principle three dimensional, the vertical velocity (along z) is always much smaller than the horizontal velocity at the mid-depth plane, where all observations are made.

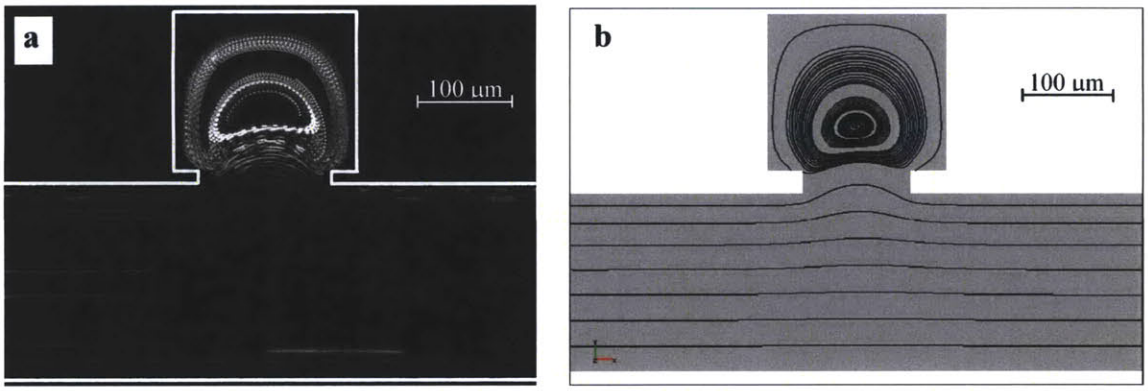

Figure 2-3. The flow in a cavity of aspect ratio $\alpha = 1$, main flow speed $U_F = 21.4$ mm s^{-1}. The characteristic velocity in the cavity is $U_C = 363$ µm s^{-1}. Lengths of the cavity and the opening are $a = 200$ µm and $g = 120$ µm, respectively. Flow is from left to right. The cavity Reynolds number ($U_C\, a/\nu$) is 0.07. (a) Trajectories of 2 µm beads. The solid white line shows the outline of the channel. (b) Numerical streamlines at the mid-depth plane ($z = H/2 = 65$ µm). Imperfections in the streamlines result from small numerical errors in integrating the velocity field. (Marcos and Stocker 2006).

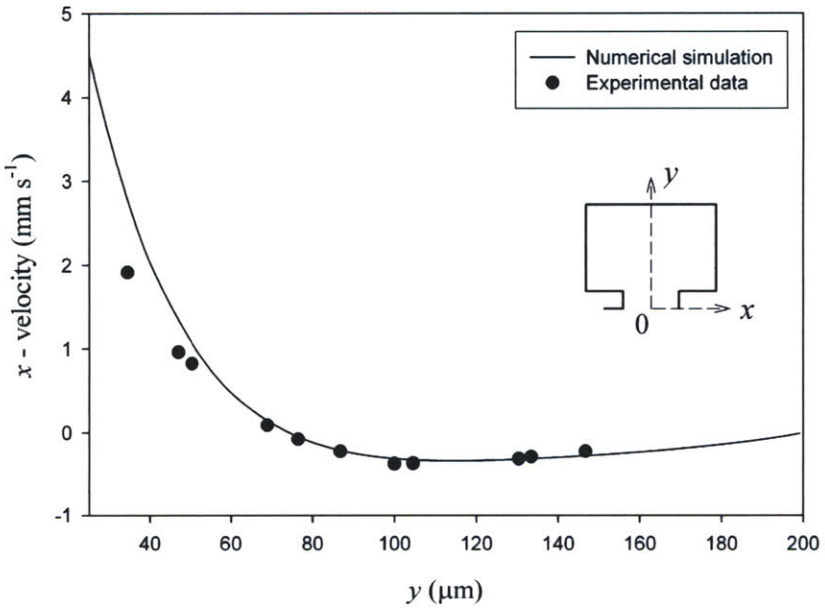

Figure 2-4. Velocity inside the cavity in the x – direction, as a function of the transverse position y (dashed line in the inset) for $U_C = 363$ µm s^{-1}. Experiments (circles) are compared with numerical results (solid line). (Marcos and Stocker 2006).

2.2.2 Effects of the cavity geometry

Because of the fabrication processes involved in soft lithography, shallower channels are easier and faster to fabricate and, in general, the depth H is limited to about 1 mm. On the other hand, a minimum depth is required to generate a vortex. For our basic configuration, a vortex starts to form for $H = 80$ µm (not shown) and is fully developed for $H \geq 90$ µm (= 0.45 a; Fig 5b).

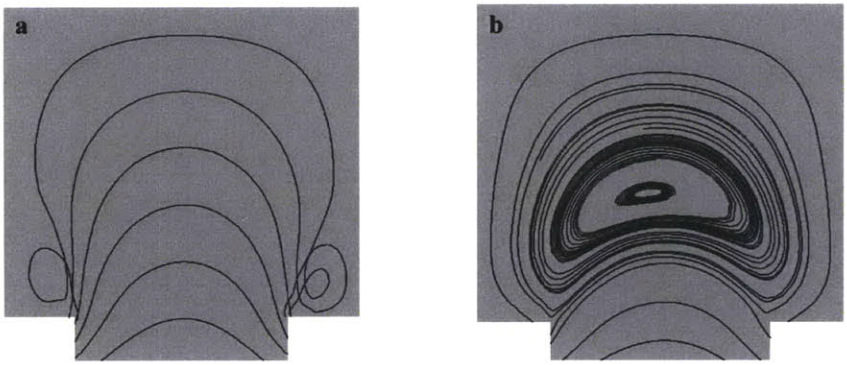

Figure 2-5. Numerical streamlines for U_F = 21.4 μm s^{-1} and two different depths: (a) H = 70 μm; (b) H = 90 μm. All other dimensions are as in Fig. 3. Crossing streamlines visible in panel (a) reflect small three-dimensional effects.

It is interesting to note that this minimum depth changes with the cavity opening length g, not considered in previous studies. It has been shown that a two-dimensional flow (i.e., $H \rightarrow \infty$) in a fully open cavity ($g = a$) generates a vortex for aspect ratios $\alpha < 2$ (Higdon 1985; Shen and Floryan 1985; Yu et al. 2005). In three-dimensional low Reynolds number flow (Re* = Re A_C < 10), however, a vortex is expected only for $A_C = (H/a)^2 > 0.327$, predicting a minimum depth $H = 0.57a$ for Re < 30.6 (Yu et al. 2005). We confirmed this prediction numerically by testing the case $g = a$ for H = 90 μm (A_C = 0.203, Re^* = 1.25), finding indeed no vortex. Partially closing the cavity opening g, on the other hand, introduces an additional degree of freedom, which we discovered reduces the minimum depth required for vortex formation. This can be seen by comparing Fig. 2-3 (g = 120 μm; a vortex forms) with Fig. 2-6a (g = 200 μm; no vortex), both obtained with H = 130 μm. Finally, no vortex formed for $\alpha = 2$, even for $g = a/2$ (Fig. 2-6b).

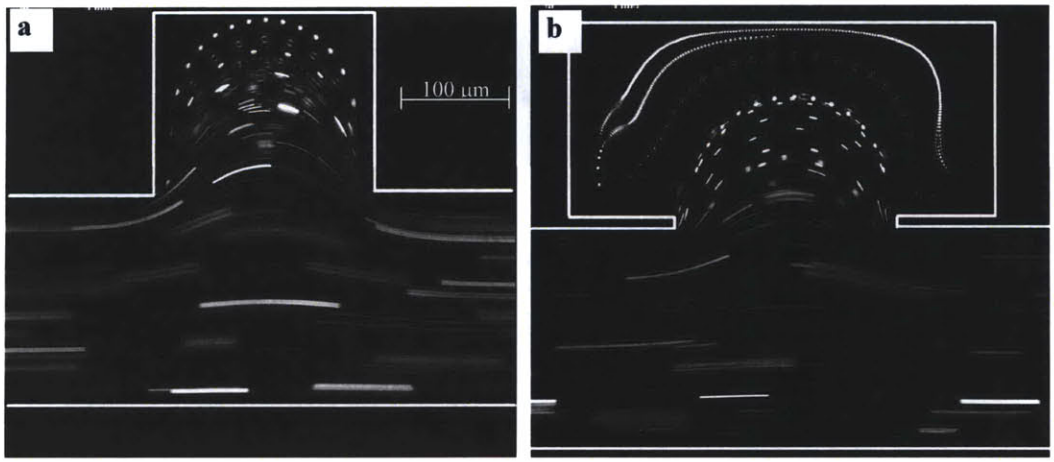

Figure 2-6. Two configurations in which no vortex formed, as shown by the trajectories of 2-μm beads: (a) α = 1, $g = a$ = 200 μm; (b) $\alpha = 2$, $g = a/2$ = 200 μm. For both cases, H = 130 μm and U_F = 21.4 mm s^{-1}. The scale is the same in the two panels.

2.2.3 Trajectories and orientation of swimming microorganisms

Our aim in designing the cavity flow was to obtain a controlled, well-characterized flow field to study the response of microorganisms. In the previous sections, we have analyzed the formation of the vortex numerically and experimentally. Here we show that this setup also allows accurate visualization and quantification of the trajectories and instantaneous orientation of microorganisms swimming in the vortex, by applying it to the marine bacterium *P. haloplanktis* and the marine alga *D. tertiolecta*.

In order to have only motile organisms inside the cavity, we pre-filled the channel with fluid, injected the microorganisms, then stopped the flow: this procedure allowed some motile cells to spontaneously enter the cavity, at which point the flow was turned on again. Trajectories were imaged in the field of view shown in Fig. 2-1 (dashed line) at mid-depth ($z = H/2$). A 40× objective was used for the bacteria and a 20× objective for the algae. No effect of the microscope light on the microorganisms was observed.

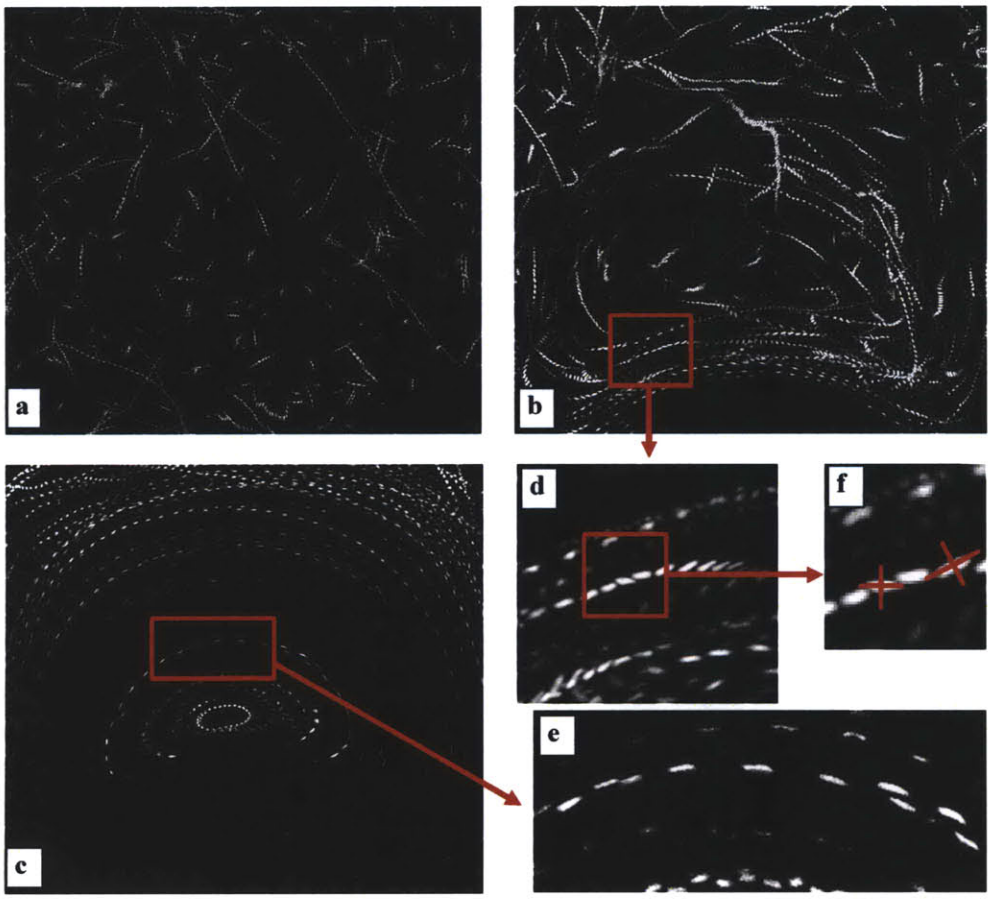

Figure 2-7. Trajectories of the bacteria *P. haloplanktis* in vortices of different strength: (a) No flow; (b) U_C = 36.3 μm s^{-1}; (c) U_C = 363 μm s^{-1}. The field of view is shown in Fig. 1; (d) and (e) are magnified views of selected trajectories, showing the instantaneous orientations of individual bacteria; (f) A bacterium's orientation is further magnified to highlight misalignment with the direction of travel.

In the absence of flow (Fig. 2-7a), *P. haloplanktis* swims in a random fashion, exhibiting a combination of long, straight runs, reversals and changes of direction, with a mean speed

of 55 μm s^{-1} and a maximum of 280 μm s^{-1}. When the flow velocity in the vortex is considerably larger than the swimming speed (Fig. 2-7c), advection by the flow overwhelms motility and trajectories tend to streamlines. The elongated shape of *P. haloplanktis*, characteristic of many species of bacteria, also allows detection of its orientation in the flow field. In a strong vortex, bacteria not only follow streamlines, but they are aligned with them as a result of the shear in the vortex (Fig. 2-7e), except for the corner regions in the cavity, which the vortex does not reach (e.g. the top corners in Fig. 2-7c). The most interesting case is that of a vortex of intermediate strength (Fig. 2-7b), where bacteria can partially 'fight the flow': several trajectories cross streamlines and, even for those that do not, the shear is not strong enough to always align bacteria with the flow direction (Figs. 2-7d and 2-7f).

We further applied the microfluidic setup to the motile alga *D. tertiolecta* (Fig. 2-8), which swims up to 375 μm s^{-1} using two flagella. Its large size (5 μm) makes it easy to capture using video-microscopy, but its instantaneous orientation is more difficult to quantify due to its nearly symmetrical shape. Many species of phytoplankton in the ocean are known to use motility for phototaxis or chemotaxis, resulting in migration and clustering in preferential regions of the water column (Sjoblad et al. 1978; Eggersdorfer and Hader 1991). Phytoplankton motility is altered by small scale vortices, and the proposed setup can help to quantify these changes (Fig. 2-8b).

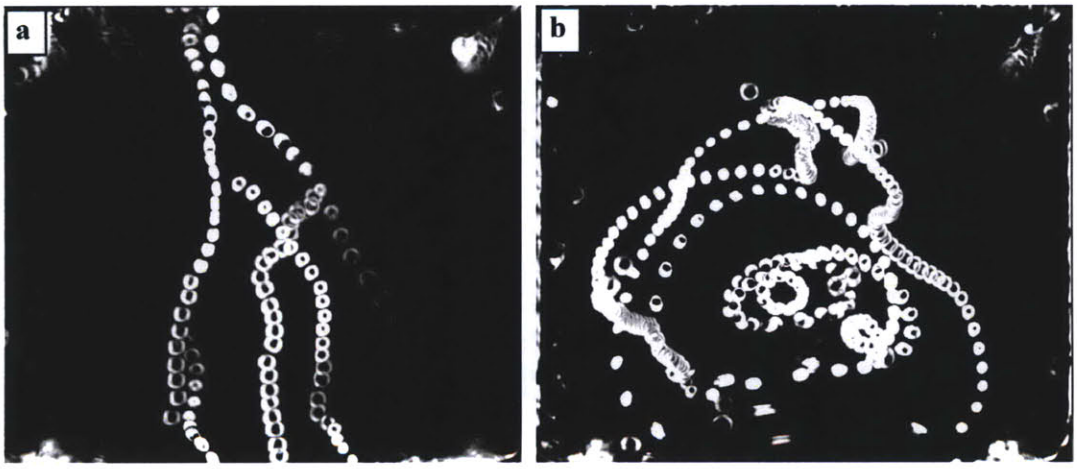

Figure 2-8. Trajectories of the alga *D. tertiolecta* swimming in the cavity: (a) No flow; (b) U_C = 363 μm s^{-1}. The field of view is shown in Fig. 2-1. The black spot inside each alga is a result of phase contrast microscopy.

A preliminary quantification of the role of advection on motility can be obtained by visual inspection of the trajectories and is summarized in Table 2-1. Motility of *P. haloplanktis* is not significantly affected for U_C < 36 μm s^{-1}, while advection dominates for U_C > 182 μm s^{-1}. *D. tertiolecta*, on the other hand, can swim faster and exhibits higher thresholds (182 – 363 μm s^{-1}) before being passively advected by the flow. In the ocean, turbulent dissipation rates ε range from 10^{-2} to 10^{-5} cm^2 s^{-3} (Lazier and Mann 1989), corresponding to Kolmogorov velocity scales of 1000 to 178 μm s^{-1} (Yamazaki et al. 2002), respectively. While the main purpose of this calculation is to demonstrate the viability of the

experimental setup and not to provide a thorough quantitative analysis of the data, Table 2-1 suggests that bacteria would be mostly advected and aligned in a turbulent flow, while motile algae can overcome mild turbulence levels.

Table 2-1. The influence of advection on P. haloplanktis and D. tertiolecta in vortices of various strengths. An equivalent dissipation rate ε is calculated based on UC. Symbols indicate the importance of advection by the vortex over motility as inferred from trajectories, from '++' (advection dominates) to '- -' (motility dominates).

U_C ($\mu m\ s^{-1}$)	ε ($cm^2\ s^{-3}$)	*P. haloplanktis* (bacterium)	*D. tertiolecta* (alga)
9	6.8×10^{-11}	- -	- -
18	1.1×10^{-9}	- -	- -
36	1.7×10^{-8}	-	- -
91	6.8×10^{-7}	+	-
182	1.1×10^{-5}	+ +	+
363	1.7×10^{-4}	+ +	+

Shear flows are known to affect the orientation of elongated bodies. Rigid spheroids undergo periodic rotation depending on their elongation (Jeffery 1922). In the case of swimming bacteria, orientation is governed by motility in addition to shear, and no theoretical prediction is available. We quantified the effects of shear on the ability of *P. haloplanktis* to control its trajectory by determining the streamline-crossing angle $\Delta\theta$ between a bacterium's trajectory and the local streamline (Fig. 2-9, inset). This angle is between 0^o and 180^o. When the bacteria are good swimmers or when the flow is weak, we expect the bacteria to swim randomly without following streamlines and thus the average $\Delta\theta$ would be 90^o. On the other hand, when the bacteria are slow swimmers or when the flow is strong, we expect the bacteria to follow the streamlines of the flow and thus small values of $\Delta\theta$. Under weak flows, *P. haloplanktis* shows a random swimming pattern resulting in an average streamline-crossing angle close to 90^o. As the shear rate increases, *P. haloplanktis* becomes more aligned with flow and thus $\Delta\theta$ decreases.

This result suggests that motile bacteria could stop swimming under highly turbulent conditions where swimming becomes energetically inefficient, as swimming consumes energy but no longer allows bacteria to move across streamlines into nutrient-rich environments. To ascertain this hypothesis, we plan to conduct experiments of bacterial active response to shear. Such experiments will be conducted in a parabolic flow field, since the flow field in the microvortex described above is complex and difficult to characterize.

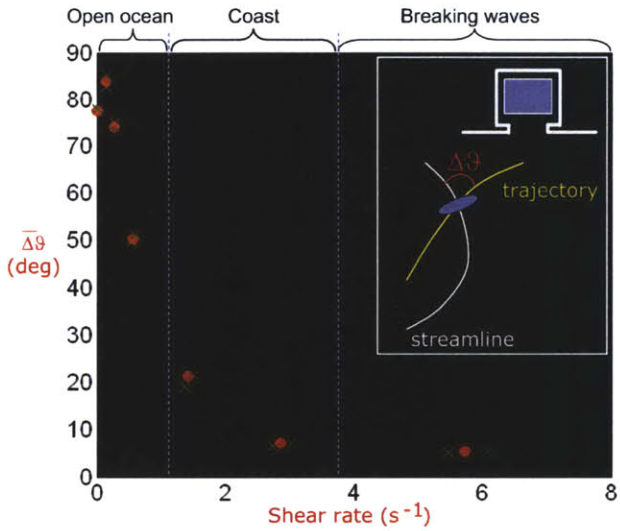

Figure 2-9. The average streamline crossing angle of *P. haloplanktis* swimming in a microvortex under various shear rates. The size of the analysis region (blue box, upper inset) is chosen arbitrarily within the field of view. The shear rate is averaged over the region of analysis. Red filled circles are the data obtained from the region of analysis. Green and yellow crosses are the data obtained by increasing and decreasing the region of analysis by 20%. The lower inset shows the definition of streamline crossing angle $\Delta\theta$.

2.3 Summary

We presented a microfluidic setup to generate vortices on scales relevant to microbial dynamics, while at the same time tracking responses of individual swimming microorganisms. We found that the formation of a vortex in the side cavity is dependent on the depth to width ratio (*H/a*) of the cavity, as well as the length of the opening (*g*) to the main channel.

We illustrated the ability of the setup to yield quantitative single-cell information on the behavior of microbes exposed to a recirculating shear flow. Steady flow in the cavity is only an approximation of Kolmogorov-scale eddies in the ocean, which are three-dimensional and unsteady (Karp-Boss et al. 1996), with time scales in the order of 1-100 s. While it would be possible to incorporate unsteadiness by modulating the flow in the microchannel over time using a programmable syringe pump, we believe the current setup in itself offers valuable insight on the fundamental interaction between microorganisms and their fluid dynamical environment (in particular the mean shear) at scales relevant to microbial dynamics, at least over times shorter than the Kolmogorov time-scale.

We envisage that microfluidic methods such as the one presented here will provide novel insight into the bounds that ambient flow imposes on the motility of microorganisms and on the behavioral strategies and dynamics of motile microbes living in a turbulent ocean. They will in turn impact our understanding of the role of microorganisms in the biogeochemistry of aquatic environments.

Chapter 3

Helix in shear

At the small scales of a bacterium, any natural flow field (e.g. turbulence) is experienced as a linear velocity profile, or `simple shear'. Therefore, understanding the interaction between a simple shear flow and swimming is a critical step towards gaining insight on how the ambient flow favors or hinders microorganisms in their quest for food. We develop a mathematical model to study the microhydrodynamics of a flagellated bacterium in a shear flow. In general, the modeling of a bacterium requires consideration of two factors: first, flagella revolve around their long axis to generate thrust and propulsion; second, a bacterium often has an inert head to which the flagella are attached. Because the Reynolds numbers are small ($\sim 10^{-4}$), the flow is described by the Stokes equation. To make the problem analytically tractable, we study the hydrodynamics around the head and the flagellum separately, neglecting the hydrodynamic interactions between the two. This is a good approximation as long as the length of the flagellum is much larger than the diameter of the head. In this chapter, we present a combined theoretical and experimental investigation of the fluid mechanics of a helix exposed to a shear flow. In addition to classic Jeffery orbits, resistive force theory predicts a drift of the helix across streamlines, perpendicular to the shear plane. The direction of the drift is determined by the direction of the shear and the chirality of the helix. We verify this prediction experimentally using microfluidics, by exposing *Leptospira biflexa flaB* mutant, a non-motile strain of helical-shaped bacteria, to a plane parabolic flow. As the shear in the top and bottom halves of the microchannel has opposite sign, we predict and observe the bacteria in these two regions to drift in opposite directions. The magnitude of the separation is in good quantitative agreement with theory. This setup can be used to separate microscale chiral objects.

3.1 Model formulation

We computed the hydrodynamic forces due to a shear flow on a helix by employing resistive force theory (RFT). RFT is the lowest order approximation of slender body theory, which provides an accurate solution of the Stokes equations for filaments with radius small compared to the length scale of filament's deformation (i.e. the pitch length of the helix) and total filament length (Gray and Hancock 1955; Childress 1981). RFT expresses the drag force per unit length as $\mathbf{f} = \zeta_{/\!/}\, \mathbf{v}^{r}_{/\!/} + \zeta_{\perp}\, \mathbf{v}^{r}_{\perp}$, with $\zeta_{/\!/}$, $\zeta_{\perp}$ being the resistive force coefficients, and $\mathbf{v}^{r}_{/\!/}$, $\mathbf{v}^{r}_{\perp}$ the velocities relative to the fluid, parallel and perpendicular to a segment of the helix (Childress 1981). Drag on a thin rod in low Reynolds number flow is anisotropic, with a greater resistance when the rod is oriented perpendicular rather than parallel to the flow ($\zeta_{\perp} \approx 2\zeta_{/\!/}$). Integrating the local force and torque per unit length along the entire helix yields the total force and torque on the helix. This yields the center-of-mass linear velocity and angular velocity as a function of the orientation of the helix and the shear rate.

In low Reynolds number world, a moving object ceases to move as soon as the applied force or the propulsion force vanishes (i.e. no inertia). To see why this is the case, consider an object or a swimmer of mass m and size L swimming with velocity U through a viscous fluid of density ρ and viscosity μ. When the swimmer suddenly stops propelling itself, it will then decelerate according to Newton's law $F_{drag} = m\ a$. The drag force F_{drag} is the viscous drag and it has the scaling of μUL. For simplicity, let's assume the swimmer is of spherical geometry with density $\rho_s \approx \rho$ (which is true for bacteria) and therefore $m \sim \rho L^3$. This gives $a \sim \mu U/(\rho L^2)$. We can now estimate the typical length scale over which the swimmer will cruise due to the inertia of its movement: $d \sim U^2/a = \rho U L^2/\mu$. For many bacteria, $U \sim 10 - 100L$ and the typical length scale for a bacterium $L \sim 1\mu m$. Using properties of water (ρ = 1000 kg m^{-3}, $\mu = 10^{-3}$ kg m^{-1} s^{-1}) leads to $d \approx 0.01 - 0.1$ nm (Purcell 1977; Lauga and Powers 2009). The corresponding time scale can be estimated as $t \sim d/U \approx 1$ μs. This analysis shows that inertia is completely negligible and as a result, the total force and torque on a body would equate to zero in low Reynolds number world.

In the following, a general introduction to RFT is presented by solving the simpler two-dimensional problem of a rigid straight rod in shear flow. We discuss the similarity of a rod and an ellipsoid in shear flow by comparing with Jeffery's solution (Jeffery 1922). We then solve the spatial evolution of a three-dimensional rigid helix in shear flow. We shall see that a helix will drift across streamline due to its chirality.

3.1.1 A rigid straight rod in shear flow

Consider a rod of unit length in a simple shear flow $\mathbf{V} = (\dot{\gamma} y, 0, 0)$, where $\dot{\gamma}$ is the shear rate (Fig. 3-1). Using RFT, the force per unit length $\mathbf{f}$ on the rod obeys

$$\mathbf{f} = \zeta_{/\!/}(\mathbf{V} - \dot{\mathbf{x}})_{/\!/} + \zeta_{\perp}(\mathbf{V} - \dot{\mathbf{x}})_{\perp} \tag{3.1}$$

where $\mathbf{x} = \mathbf{x}(s, t)$ is the position of a point on the rod with arclength s. Measure length in units of the rod length, with s running from -1/2 to 1/2.

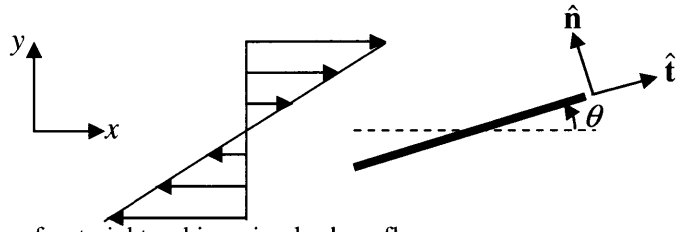

Figure 3-1. Schematic of a straight rod in a simple shear flow

Denote the tangent to the rod as $\hat{\mathbf{t}} = (\cos\theta, \sin\theta, 0)$; thus

$$\mathbf{x} = \mathbf{x}_0 + s\hat{\mathbf{t}} \qquad \dot{\mathbf{x}} = \dot{\mathbf{x}}_0 + s\dot{\theta}\hat{\mathbf{n}}$$

where $\mathbf{x}_0$ denotes the center of mass, $\dot{\theta}$ is the rotation rate of the rigid body, and $\hat{\mathbf{n}} = (-\sin\theta, \cos\theta, 0)$ is the perpendicular direction to the rod. Thus

$$f_{//} = \zeta_{//}\left(\mathbf{V} - \dot{\mathbf{x}}_0\right)_{//} \qquad f_{\perp} = \zeta_{\perp}\left(\mathbf{V} - \dot{\mathbf{x}}_0\right)_{\perp} + \zeta_{\perp} s\dot{\theta}$$

Since the direction of the rod tangent is constant (the rod is straight), we may get the parallel and perpendicular total forces by integrating $f_{//}$ and $f_{\perp}$ over s. Terms that are linear in s will vanish. Note that we need to evaluate $\mathbf{V}$ at $y = y_0 + s\sin\theta$. Integrating and setting the total force equal to zero, we find that $\dot{\theta}$ drops out of the force balance equation and

$$\dot{\mathbf{x}} = (\dot{\gamma} y, 0, 0) = \mathbf{V}$$

The center of mass moves with the flow velocity at the center of mass.

To find the rotation, we demand that the total moment vanish:

$$\int \mathbf{r} \times \mathbf{f} ds = 0$$

where we use the center of mass as the origin for calculating moments. Note that only the perpendicular component $f_{\perp}$ enters here. Plugging in $\mathbf{r} = s\hat{\mathbf{t}}$ and our expression for $f_{\perp}$ yields

$$\dot{\theta} = -\dot{\gamma}\sin^2\theta \tag{3.2}$$

These results are consistent with Jeffery's solution (Jeffery 1922; Visser and Jonsson 2000), which describes the kinematics of an ellipsoid in simple shear flow and predicts that the ellipsoid follows the streamline with the local fluid velocity and rotates with an angular velocity (Trevelyan and Mason 1951)

$$\dot{\theta} = -\frac{\dot{\gamma}}{r^2 + 1}\left(r^2 \sin^2\theta + \cos^2\theta\right) \tag{3.3}$$

where r here is the aspect ratio of the ellipsoid. The more elongated a body, the longer its residence time when aligned with streamlines. Note that when $r \to \infty$, we obtain Eq. (3.2).

The analysis of the fixed points $\theta = 0$ and $\theta = \pi$ is interesting. They are physically equivalent. Each one is half-stable and half-unstable, since $\dot{\theta}$ is always decreasing. For example, for small θ ($\theta \to 0$), Eq. (3.2) becomes $\dot{\theta} = -\dot{\gamma}\theta$ and thus $\theta^{-1} = t + \theta_0^{-1}$. If θ is small and positive, the shear will align the rod with the flow. The time it takes to align (i.e. to reach $\theta = 0$), blows up, because $t = 0^{-1} - \theta_0^{-1} \to \infty$. Therefore, when θ is small and positive, it is stable. However, if θ is small and negative, the shear will flip the rod around to the opposite orientation and thus makes it unstable.

3.1.2 Helix in a shear flow

The general equations for the evolution of the orientation of a helix in shear flow in terms of Euler angles are presented. We will see that unlike the rod, the center of mass of the helix does not move at the speed of the flow velocity at the center of mass.

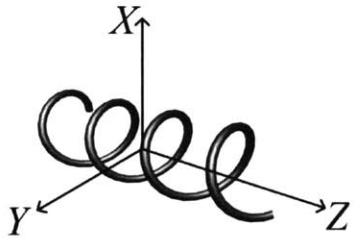

Figure 3-2. Schematic of helix in a body fixed frame *OXYZ*

Suppose that the helix has an integer number n of full turns and a total contour length of l and furthermore that the helix axis is parallel to the Z-axis (Fig. 3-2). In a body fixed frame *OXYZ*, with the center of the helix as the origin O, the helix is given by (Kim and Powers 2005)

$$\mathbf{r}_{helix} = \left(R\cos\left(\frac{2\pi\chi ns}{l}\right), R\sin\left(\frac{2\pi\chi ns}{l}\right), s\cos\alpha \right) \tag{3.4}$$

where s runs from $-l/2$ to $l/2$, R is the helix radius, α is the pitch angle, and $\chi = \pm 1$ is the handedness; it is convenient to keep $\alpha > 0$ no matter what the handedness. Note that $2\pi Rn/l = \sin\alpha$, where l/n is the contour length for one turn of the helix. Thus, the tangent to the helix is

$$\hat{\mathbf{t}}_{helix} = \left(-\chi\sin\alpha\sin\left(\frac{2\pi\chi ns}{l}\right), \chi\sin\alpha\cos\left(\frac{2\pi\chi ns}{l}\right), \cos\alpha \right) \tag{3.5}$$

Now consider the helix in an arbitrary position and orientation in a 3D fixed inertial space *oxyz*. The center of the helix in the inertial frame is $\mathbf{x}_0 = (x_G, y_G, z_G)$. The orientation of the helix can be expressed through three sets of Euler angles, such that the position of any point on the helix can be expressed in the inertial frame *oxyz* by the following relation

$$\mathbf{r} = \mathbf{x}_0 + \left[T_{Euler}\right]^{tr} \cdot \mathbf{r}_{helix}$$

and the tangent vector is given by

$$\hat{\mathbf{t}} = \left[T_{Euler}\right]^{tr} \cdot \hat{\mathbf{t}}_{helix}$$

where the Euler rotation matrix $[T_{Euler}] = [T_\phi] .[T_\psi] .[T_\theta]$ is a result of three consecutive rotations:

$$[T_\theta]=\begin{bmatrix}\cos\theta & \sin\theta & 0\\ -\sin\theta & \cos\theta & 0\\ 0 & 0 & 1\end{bmatrix};\ [T_\psi]=\begin{bmatrix}\cos\psi & 0 & -\sin\psi\\ 0 & 1 & 0\\ \sin\psi & 0 & \cos\psi\end{bmatrix};\ [T_\phi]=\begin{bmatrix}1 & 0 & 0\\ 0 & \cos\phi & \sin\phi\\ 0 & -\sin\phi & \cos\phi\end{bmatrix} \quad (3.6)$$

The Euler rotations are performed as follows (Fig. 3-3):

- Rotation about the z axis through an angle $\theta \in [0,2\pi]$
- Rotation about the new y axis through an angle $\psi \in [0,\pi]$
- Rotation about the new z axis (the Z axis in the $OXYZ$ frame) through an angle $\phi \in [0,2\pi]$

Since the transformation is orthogonal $[T_{Euler}]^{-1} = [T_{Euler}]^{tr}$

In the standard spherical polar coordinate system, ψ and θ would be the polar and the azimuthal angles describing the orientation of the major axis of the helix. The angle ϕ is the rotation along the axis of the helix (Fig. 3-3). When all angles are zero ($\theta = \psi = \phi = 0$), the body fixed frame coincides with the inertial frame, i.e. $OXYZ = oxyz$ and the helix axis is along the z axis. The helix axis is pointing along the y axis when $\theta = \psi = \pi/2$ and along the x axis when $\theta = 0$, $\psi = \pi/2$.

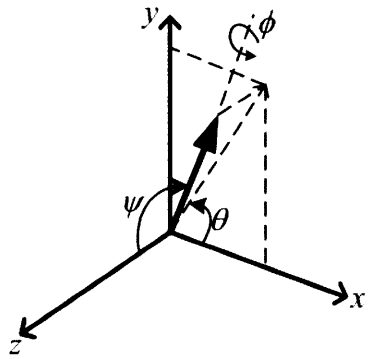

Figure 3-3. Euler angles describing the body orientation. The arrow represents the major axis of the body.

Consider the helix in a simple shear flow $\mathbf{V} = (\dot{\gamma} y, 0, 0)$. The velocity of the flow relative to the helix in the inertial frame is

$$\mathbf{v}_{rel} = \mathbf{V} - \mathbf{v} - \boldsymbol{\omega} \times \mathbf{r} \quad (3.7)$$

where $\mathbf{v}$ and $\boldsymbol{\omega}$ are the linear and angular velocities of the center of the helix given by

$$\mathbf{v} = (v_x, v_y, v_z); \qquad \boldsymbol{\omega} = (\omega_x, \omega_y, \omega_z) \quad (3.8)$$

Note that $y = y_G + \left[T_{Euler}\right]^{tr} \cdot \mathbf{r} \cdot (0,1,0)$

In resistive force theory, the force per unit length acting on the helix is given by the fluid velocity relative to the helix velocity, with anisotropic resistance coefficients as previously described. Therefore, the total forces on the helix are

$$F_i = \int_{-l/2}^{l/2} \left(\zeta_{//} \mathbf{v}_{rel//} + \zeta_{\perp} \mathbf{v}_{rel\perp} \right) ds \cdot \hat{\mathbf{e}}_i \tag{3.9}$$

where $\hat{\mathbf{e}}_i$ (i = 1,2,3) is the space fixed basis vector. Noting that $\mathbf{v}_{rel//} = \left(\mathbf{v}_{rel} \cdot \hat{\mathbf{t}} \right) \hat{\mathbf{t}}$ and $\mathbf{v}_{rel} = \mathbf{v}_{rel//} + \mathbf{v}_{rel\perp}$, Eq. (3.9) becomes

$$F_i = \int_{-l/2}^{l/2} \zeta_{//} \left[\frac{\zeta_{\perp}}{\zeta_{//}} \mathbf{v}_{rel} + \left(1 - \frac{\zeta_{\perp}}{\zeta_{//}} \right) \mathbf{v}_{rel//} \right] ds \cdot \hat{\mathbf{e}}_i \tag{3.10}$$

Similarly, the total torques on the helix are

$$M_i = \int_{-l/2}^{l/2} \mathbf{r} \times \zeta_{//} \left[\frac{\zeta_{\perp}}{\zeta_{//}} \mathbf{v}_{rel} + \left(1 - \frac{\zeta_{\perp}}{\zeta_{//}} \right) \mathbf{v}_{rel//} \right] ds \cdot \hat{\mathbf{e}}_i \tag{3.11}$$

Equations (3.10) and (3.11) can be written in matrix form as:

$$\begin{pmatrix} F_x \\ F_y \\ F_z \\ M_x \\ M_y \\ M_z \end{pmatrix} = \begin{pmatrix} \zeta_{11} & \zeta_{12} & \zeta_{13} & \zeta_{14} & \zeta_{15} & \zeta_{16} \\ \zeta_{12} & \zeta_{22} & \zeta_{23} & \zeta_{24} & \zeta_{25} & \zeta_{26} \\ \zeta_{13} & \zeta_{23} & \zeta_{33} & \zeta_{34} & \zeta_{35} & \zeta_{36} \\ \zeta_{14} & \zeta_{24} & \zeta_{34} & \zeta_{44} & \zeta_{45} & \zeta_{46} \\ \zeta_{15} & \zeta_{25} & \zeta_{35} & \zeta_{45} & \zeta_{55} & \zeta_{56} \\ \zeta_{16} & \zeta_{26} & \zeta_{36} & \zeta_{46} & \zeta_{56} & \zeta_{66} \end{pmatrix} \begin{pmatrix} v_x \\ v_y \\ v_z \\ \omega_x \\ \omega_y \\ \omega_z \end{pmatrix} + \begin{pmatrix} A_1 \\ A_2 \\ A_3 \\ A_4 \\ A_5 \\ A_6 \end{pmatrix} \tag{3.12}$$

where $\{\zeta\}$ is the 6×6 symmetric resistance matrix and $\{A\}$ is the contribution due to the shear flow.

Stokes flow requires total forces and total torques to be zero, which sets the left-hand-side of Eq. (3.12) to zero and allows us to solve for the linear and angular velocities of the helix. In the following, we will see that a helix drifts across streamlines when exposed to a shear flow. We will present an intuitive explanation why this would be the case before looking at the drift trajectory of a helix using the solution to Eq. (3.12).

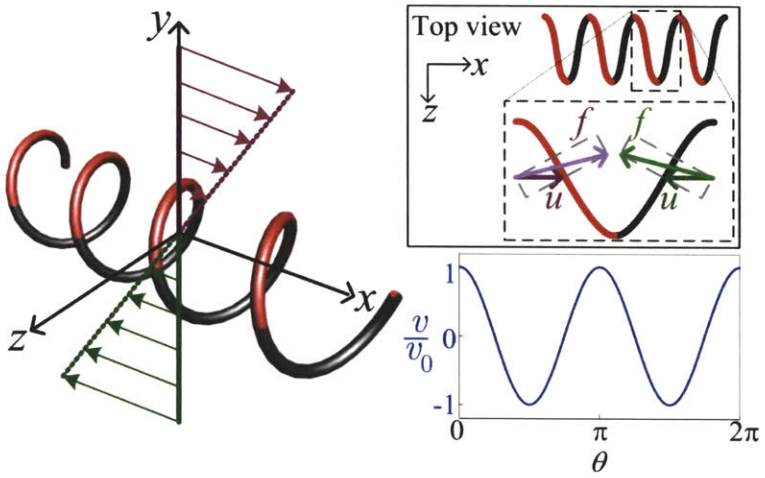

Figure 3-4. Schematic of a right-handed helix in simple shear flow. Red shading and black shading show the top and bottom halves of the helix. Upper inset: The net force acting on one pitch of the helix is along $-z$. Lower inset: Predicted normalized drift velocity v/v_0 versus helix orientation θ. θ is the angle between a helix in the x-y plane and the flow, and v_0 is the drift velocity of a helix aligned with the flow ($\theta = 0$, $\psi = \pi/2$). (Marcos et al. 2009).

As described earlier, in a shear flow, objects undergo periodic rotations known as Jeffery orbits (Jeffery 1922): a sphere rotates with constant angular velocity, whereas for an elongated body, such as a helix, the velocity depends on orientation. The more elongated a body, the longer its residence time when aligned with streamlines (see Eq. (3.3)). In addition to undergoing Jeffery orbits, a helix drifts across streamlines, due to its chirality. To see why, consider a right-handed helix aligned with a simple shear flow (Fig. 3-4), and decompose the velocity at a segment of the helix into components perpendicular and parallel to the segment. We have discussed that drag on a thin rod in low Reynolds number flow is anisotropic, with a greater resistance when oriented perpendicular rather than parallel to the flow (Childress 1981). Since the flows at the top (red) and bottom (black) halves of the helix are in opposite directions, both halves have a drag component along $-z$ (Fig. 3-4, top inset). Thus, a right-handed helix aligned with the shear flow drifts in the $-z$ direction. Reversing the chirality of the helix or the sign of the shear produces a drift along $+z$. Furthermore, the drift depends on the orientation of the helix. Suppose the right-handed helix is reoriented by 90 degrees so that it is aligned with the y-axis. In this orientation, the halves formerly labeled "upper" and "lower" are now the halves split in the $+x$ and $-x$ directions, and the shear flow tends to rotate the helix in the vorticity direction of the shear flow ($-z$ direction). Due to the rotation, the component of the relative flow along the helix axis past the formerly upper and lower halves is in the opposite direction compared to when the helix was aligned with the x-axis. Therefore the force, and the drift, are in the $+z$ direction for the right-handed helix aligned with the y-axis. In general, the drift velocity v of a helix lying in the x-y plane is a function of the angle θ between the helix and the flow (Fig. 3-4, bottom inset). Hence, the mean drift depends on the distribution of the orientation of the helix relative to the flow. When the helix is preferentially aligned with streamlines, for example due to Jeffery orbits, it has a net drift (Fig 3-5). When all orientations are equally likely, for example due to strong Brownian rotational diffusion, the

net drift is zero (Makino and Doi 2005). The mean drift depends on the probability distribution of orientations of the helix relative to the flow (see section 3.2.3). This distribution is determined by the competition between the two timescales: preferential alignment due to shear ($\tau_{shear} = 1/\dot{\gamma}$) and isotropic distribution due to Brownian rotational diffusivity ($\tau_{Brown} = 1/D_R$). From these two timescales, we can form a dimensionless number: Peclet number Pe = $\tau_{Brown} / \tau_{shear} = \dot{\gamma} / D_R$, which determines the relative importance between shear alignment and Brownian rotational diffusivity. For large Pe, alignment by shear dwarfs rotational diffusion and for small Pe, diffusion destroys the alignment, resulting in zero net drift.

Figure 3-5 shows the lateral position of the center of a right-handed helix (z_G) when exposed to a positive shear flow neglecting Brownian diffusion, obtained from the RFT solution. The helix is initially at the origin (0, 0, 0) with its orientation pointing along the x axis. The simulation shows that the helix drifts in the $-z$ direction as predicted. The small "bumps" in the trajectory are due to the fact that the helix performs a Jeffery orbit and at some point the axis is aligned with the y axis, hence the helix briefly drifts in the $+z$ direction. However, due to its large aspect ratio, the helix is preferentially aligned with the flow and thus experiences a net drift in the $-z$ direction. The mean drift velocity $\bar{v}$ for this helix is $0.008\,\dot{\gamma}$ μm s^{-1} (e.g. for $\dot{\gamma} = 10$ s^{-1}, $\bar{v} = 0.08$ μm s^{-1}) in the $-z$ direction. For an *E. coli* flagellar bundle (a left-handed helix with 4 turns, pitch angle of 41°, and contour length of 13 μm), the mean drift velocity $\bar{v}$ is $0.07\,\dot{\gamma}$ μm s^{-1} in the $+z$ direction.

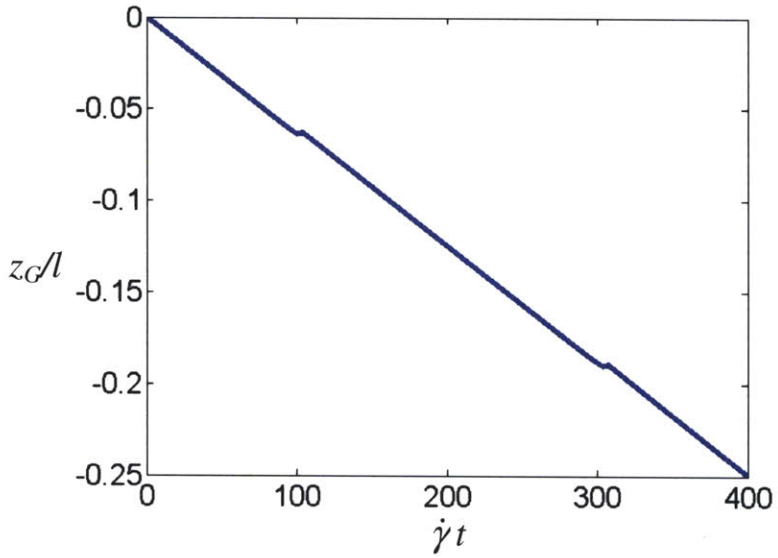

Figure 3-5. Predicted lateral drift of a right-handed helix in simple shear flow in the absence of Brownian motion. The number of full turns is $n = 25$, pitch angle $\alpha = 45°$, total contour length $l = 14.1$ μm, and we assumed $\zeta_\perp/\zeta_{//} = 2$. The helix is initially at (0,0,0) and pointing along the x axis ($\theta = 0$, $\psi = \pi/2$).

In the next section, we present a microfluidic setup to verify this prediction by exposing helically shaped bacteria to shear flows and measuring the associated lateral drift (Marcos et al. 2009). We will also discuss the comparison with the model developed here and the effect of Brownian rotational diffusivity.

3.2 Experimental verification

3.2.1 Experimental setup

We use a nonmotile, right-handed, helically shaped bacterium, *Leptospira biflexa* flaB mutant (Picardeau et al. 2001) (Fig. 3-6a), as the microscale helix. These spirochetes have an average length of 16 μm, thickness of 150 nm, and diameter of 200 nm (Fig. 3-6a and Wolgemuth et al. 2006). Here *L. biflexa* flaB mutant acts as a convenient model organism because of its helical shape.

To expose spirochetes to a shear flow, we fabricated a 110 cm long, serpentine-shaped microfluidic channel via soft lithography (see section 2.1.1) (Figs. 3-6b,c). The channel has a rectangular cross section with large aspect ratio ($W/H \approx 11$; Fig. 3-6c), such that the flow is uniform across the width, except for a 150 μm thick boundary layer at the sidewalls (Doshi et al. 1978). Across the channel depth, the flow has a parabolic profile $u(y) = (3U_F/2)[1-(2y/H)^2]$, leading to a shear rate which varies linearly, $\dot{\gamma}(y) = du/dy = -12yU_F/H^2$, negative in the top half of the channel and positive in the bottom half. We performed experiments in a channel with dimensions shown in Fig. 3-6c, where a mean flow speed of 3.09 mm s^{-1} generated shear rates of order 100 s^{-1}. The microchannel is equipped with two inlets, one for spirochetes and one for buffer solution (EMJH liquid medium: Picardeau et al. 2001 and see the Appendix for the media recipe). Spirochetes were introduced through a microinjector, forming a band of width $w \approx 100$ μm at the center of the channel, uniform over the depth, with buffer streams on either side. Due to the linear variation in shear over depth, the lateral drift of the spirochetes is expected to vary with depth: spirochetes should move laterally in opposite directions in the top and bottom halves of the channel (Fig. 3-6c).

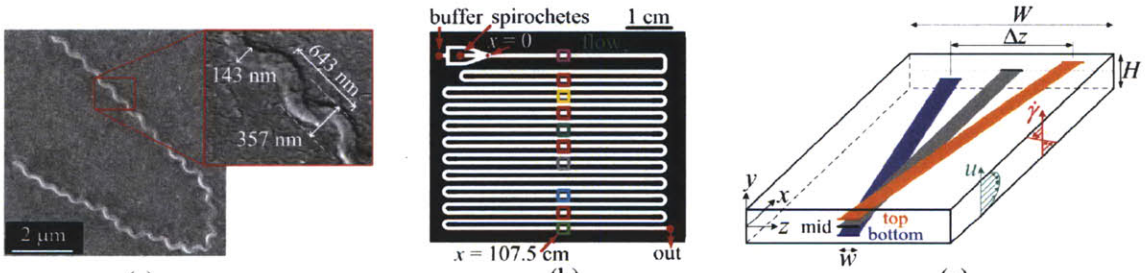

Figure 3-6. (a) Scanning electron micrograph (SEM) of *L. biflexa* flaB mutant, with typical dimensions (inset). The bent configuration is a result of SEM preparation and live organisms are nearly always straight. (b) Microchannel design with separate inlets for spirochetes and buffer. The color-coded squares refer to the locations of data collection (Fig. 3-7b). (c) Schematic of the separation process (for right-handed helices) in the microchannel (W = 1 mm, H = 90 μm, $w \approx 100$ μm). The lateral drift direction depends on the sign of the shear $\dot{\gamma}$, resulting in divergence of top and bottom streams. (Marcos et al. 2009).

We imaged the spirochete population using phase contrast microscopy with a 40× long-working distance objective (NA = 0.6) and a CCD camera (PCO 1600, Cooke, Romulus, MI). At ten locations along the channel (Fig. 3-6b), sets of 50 images were recorded at 1.5 s intervals at three depths: $y = -H/4$ ("bottom"), $y = 0$ ("mid"), and $y = H/4$ ("top").

3.2.2 Experimental results and discussion

Experiments revealed a clear and reproducible drift, with direction determined by the sign of the local shear rate. A superposition of 50 images acquired at x = 107.5 cm shows drift of comparable magnitude and opposite direction in the top and bottom halves, and no drift at midplane, where $\dot{\gamma} = 0$ (Fig. 3-7c). Using image analysis to obtain the z position of individual spirochetes, we determined the probability density function of the across-channel distribution of cells, their mean position $\overline{z}$, and the one-standard-deviation spread σ, for each imaging location (x, y). The drift of the top and bottom populations increases monotonically with x or, equivalently, with time.

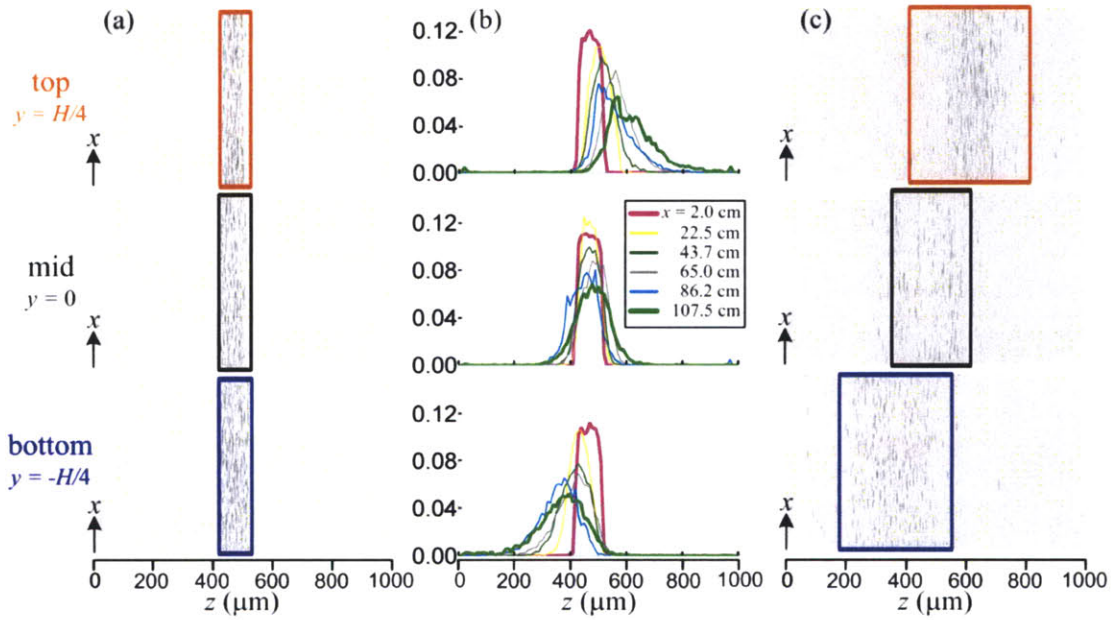

Figure 3-7. Observed spirochete distributions across the channel width for (a) x = 2 cm and (c) x = 107.5 cm. Orange, black, and blue correspond to the top, mid, and bottom depths. The midpoint of each rectangle corresponds to the mean position ($\overline{z}$) of the distribution, while the half-width is 2 standard deviations (2σ). b) Probability distribution function, obtained from fifty images at each location, for various distances x along the channel. Over 10,000 spirochetes were imaged for each location x, y. The broadening of the population distribution is accounted for by the finite depth of focus of the imaging system, combined with variation of shear (hence, drift) with depth. (Marcos et al. 2009).

The spread in the spirochete distribution with increasing distance x (Figs. 3-7b,c) was not caused by an actual broadening of the spirochete band, but rather resulted from the combined effect of a depth-variable drift velocity (v varies linearly with $\dot{\gamma} = -12yU_F/H^2$, hence with y) and the finite depth of focus δ of the objective. The resulting standard deviation in the distribution is $\sigma(x) = \sigma_0 + \left|v^+/u^+ - v^-/u^-\right| x/2$, where σ_0 = 25 μm is the initial (x = 0) standard deviation, the superscripts ± refer to positions $y \pm \delta/2$ at the top and bottom of the focus plane, and u and v are the local axial velocity (along x) and lateral drift velocity (along z), respectively. The depth of focus of the 40× objective (NA = 0.6) taking a particle diameter of 357 nm (Fig. 3-6a) was $\delta \approx$ 10 μm (Meinhart et al. 2000). Using the observed value v = 0.41 μm s^{-1} at $y = H/4$, we obtain $v^{\pm}$ = 0.50 and 0.32 μm s^{-1} at $y = H/4$

$\pm \delta/2$, respectively. The associated $\sigma(x)$ (Fig. 3-7) differs from observations by less than 20%, confirming the predicted effect of the objective's depth of focus. The best fit to the data corresponds to $\delta = 14$ μm, which is within the uncertainty bounds in the estimate of δ, as its theoretical prediction (Meinhart et al. 2000) relies on an arbitrary cut-off intensity. Furthermore, $\sigma(x)$ increases linearly with x, ruling out Brownian motion as the cause of the increase in the spread. These observations also apply to the population at mid-depth ($y = 0$). Brownian motion was negligible and can be calculated from the lateral and rotational drag coefficients of a helix obtained from the resistance matrix Eq. (3.12) derived through RFT. The linear and rotational Brownian diffusion coefficients can be estimated using the Stokes-Einstein equations, $D = kT/\zeta_{33}$ and $D_R = kT/\zeta_{66}$, respectively. With the parameters from Fig. 3-6a and assuming $\zeta_\perp/\zeta_{//} = 1.5$ (see section 3.2.3), one obtains $D = 5\times10^{-14}$ m^2 s^{-1} and $D_R = 2.3 \times 10^{-3}$ s^{-1}. This corresponds to a spread in the spirochete band of $\sigma = \sqrt{2Dt} \approx$ 6 μm after $t = x/U_F = 348$ s ($x = 107.5$ cm, $U_F = 3.09$ mm s^{-1}).

Turns in the serpentine-shaped channel had no effect on the observed drift, for two reasons. First, particle inertia was negligible, as the particle Reynolds number $\mathrm{Re} = \dot{\gamma}L^2/\nu << 1$, where $\dot{\gamma} = 103$ s^{-1} is the shear rate at $y = H/4$, $L = 16$ μm is the axial length of the helix and $\nu = 1.0 \times 10^{-6}$ m^2 s^{-1} is the kinematic viscosity of the fluid (Di Carlo et al. 2007). Second, while Dean vortices could in principle form when flow changes direction, they were precluded by the high aspect ratio of the microchannel ($W/H = 11$), large radius of curvature ($R = 1$ mm) and the low Reynolds and Dean number of the flow ($\mathrm{Re_F} = U_F H/\nu = 0.3$ and $\mathrm{De} = (H/R)^{0.5}\mathrm{Re_F} = 0.09$) (Howel et al. 2004; Sudarsan and Ugaz 2006). Separate experiments with neutrally buoyant 1 μm spheres and fluorescent dye further confirmed the absence of secondary flows. In addition, the bends can not influence separation because they affect the top and the bottom spirochete populations in the same way.

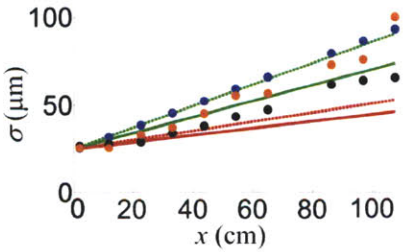

Figure 3-8. The standard deviation σ of the spirochete distribution versus distance x in the microchannel. Circles are experimental data, color-coded according to depth as in Fig. 3-6c. Solid and dashed lines refer to values calculated with a depth of focus $\delta = 10$ μm and 14 μm, respectively, while green and red lines correspond to $y = H/4$ (or, equivalently, $y = -H/4$) and $y = 0$, respectively. (Marcos et al. 2009).

Since drift ($\overline{z}$) increases linearly with distance x along the channel (Fig. 3-9a), the mean drift velocity is constant ($\overline{v} = 0.41$ μm s^{-1}), resulting in a linearly increasing separation distance Δz between the top and bottom populations (Fig. 3-9b). Control experiments with neutrally buoyant, spherical (i.e. achiral) 1 μm beads showed no drift at any depth (Fig. 3-9a, empty squares), and thus no separation (Fig. 3-9b, empty squares), supporting the conclusion that drift is a result of chirality.

The top and bottom streams separate linearly with distance down the channel (Fig. 3-9b). We calculated a separation efficiency, $\eta = |N_L - N_R|/(N_L + N_R)$, with N_L and N_R the number of spirochetes on the left and right sides of the mean position of the mid population; $\eta = 0$ for no separation, and $\eta = 1$ for complete separation. Whereas $\eta < 0.2$ for spheres, for spirochetes η increases along the channel, plateauing at $\eta \approx 0.8$ after $x \approx 70$ cm (Fig. 3-9c) and demonstrating effective separation of the top and bottom populations over the length of the channel. While we have demonstrated the lateral drift of right-handed helices in this microchannel, this setup can also be used to separate racemic mixtures of chiral particles relevant to pharmaceutical and agricultural industries (see section 3-3).

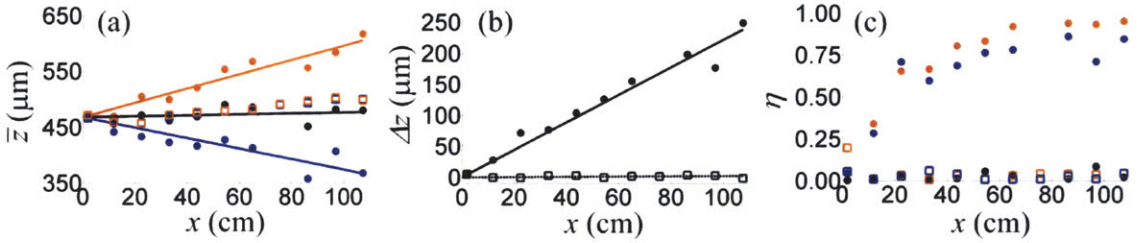

Figure 3-9. Experimental quantification of spirochete distribution: a) Average lateral position at top, mid, and bottom depths, and b) separation between top and bottom populations, as a function of distance x along the channel. c) Hypothetical separation efficiency. In a), b), and c), full circles are data from spirochetes, lines are linear fits, and empty squares are control data from spherical beads. (Marcos et al. 2009).

3.2.3 Comparison with theory

To confirm that the observed lateral drift is due to the coupling of shear and chirality, we use resistive force theory as described in Section 3.1.2 and model a spirochete as a 25-turn helix with dimensions shown in Fig. 3-6a. The resistive coefficients $\zeta_{//}$, $\zeta_{\perp}$ can be calculated by (Childress 1981)

$$\zeta_{//} = \frac{4\pi\mu}{\ln\left(4\lambda^2/a^2\right) - 1} \qquad \zeta_{\perp} = \frac{8\pi\mu}{\ln\left(4\lambda^2/a^2\right) + 1} \tag{3.13}$$

or

$$\zeta_{//} = \frac{2\pi\mu}{\ln\left(2\lambda/a\right)} \qquad \zeta_{\perp} = \frac{4\pi\mu}{\ln\left(2\lambda/a\right) + \frac{1}{2}} \tag{3.14}$$

where a and λ are the half-thickness and wavelength of the helix, respectively.

Thus the drag anisotropy $\zeta_{\perp}/\zeta_{\parallel}$ depends on the thickness of the spirochete body and varies between 1.4 [Eq. (3.13)] and 1.7 [Eq. (3.14)]. As mentioned earlier, in Stokes flow, the linear and angular velocities of the helix are determined by total force and total moment balance. This yields the drift velocity v of a spirochete for an arbitrary orientation relative to the flow. Since we observe that the spirochetes lie in the x-y plane to within 10°, we adopt a two-dimensional model with orientations limited to the x-y plane. The mean

drift velocity then depends on the probability distribution $c(\theta)$ of orientations of the helix relative to the flow. This distribution obeys

$$\partial_t c = D_R \partial_\theta^2 c - \partial_\theta \left(\dot{\theta} c \right) \tag{3.15}$$

where $D_R = 2.3 \times 10^{-3}$ s^{-1} is the rotational diffusivity of an $L = 16$ μm long spirochete and $\dot{\theta}$ is the rotation rate caused by the shear flow. We approximate $\dot{\theta}$ as the rotation rate of an ellipsoid with aspect ratio r, $\dot{\theta} = -\dot{\gamma}\left(\cos^2\theta + r^2 \sin^2\theta\right)/\left(1 + r^2\right)$ [Eq. (3.3), (Jeffery 1922)], with $r = 70$, as computed from the ratio of the rotation rates of the spirochetes at $\theta = 0$ and $\theta = \pi/2$ obtained from resistive force theory. The steady-state solution ($\partial_t c = 0$) for $c(\theta)$ was obtained numerically (using COMSOL Multiphysics) and the mean drift velocity computed as $\overline{v} = \int_0^{2\pi} v(\theta) c(\theta) d\theta$. This resulted in $\overline{v} = 0.81$–1.22 μm s^{-1}, which is of the same order of the measured value (0.41 μm s^{-1}). The residual discrepancy might be associated with the flexibility of the spirochetes and irregularities in their geometry.

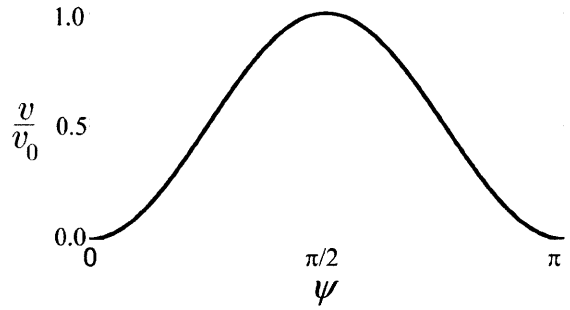

Figure 3-10. The effect of the polar angle ψ on the drift velocity v. v_0 is the drift velocity of a helix aligned with the flow ($\theta = 0$; $\psi = \pi/2$). (Marcos et al. 2009).

For the purpose of discussion, here we present the corresponding three-dimensional (3D) model to justify the accuracy of the 2D model. The probability distribution c of orientations of a helix in 3D can be described using the azimuthal and polar angles, θ and ψ (Fig. 3-3): $c(\psi, \theta)$ obeys

$$\partial_t c = D_R \nabla^2 c - \nabla \cdot \left(\dot{\boldsymbol{\omega}} c \right) \tag{3.16}$$

where $\dot{\boldsymbol{\omega}} = \dot{\psi} \hat{\mathbf{e}}_\psi + \dot{\theta} \hat{\mathbf{e}}_\theta$. We approximate $\dot{\boldsymbol{\omega}}$ as the rotation rate of an ellipsoid with aspect ratio $r = 70$, $\dot{\theta}$ given by Eq. (3.3), and

$$\dot{\psi} = \dot{\gamma}\left(r^2 - 1\right)\left(\cos\theta \sin\theta \cos\psi \sin\psi\right)/\left(1 + r^2\right) \tag{3.17}$$

The drift velocity v is now also a function of ψ (Fig. 3-10), in addition to θ (Fig. 3-4, bottom inset). v is maximum when the helix is aligned with the flow and zero when it is parallel to the z axis. The steady-state solution ($\partial_t c = 0$) for $c(\psi, \theta)$ was obtained

numerically (using COMSOL Multiphysics) and the mean drift velocity computed as $\overline{v} = \int_0^{2\pi} \int_0^{\pi} v(\psi,\theta)c(\psi,\theta)\sin\psi d\psi d\theta$. The mean drift velocity $\overline{v}$ is always lower in 3D compared to 2D (Table 3-1), irrespective of the Peclet number Pe = $\dot{\gamma}/D_R$. The difference between 2D and 3D decreases with increasing Pe, as helices spend more time aligned with the flow and thus in the x-y plane. This explains the observation that the spirochetes lie within 10^o in the x-y plane. For our experimental conditions (Pe $\approx 4 \times 10^4$) results from the 2D and 3D models are within 0.7%.

Table 3-1. Comparison of $\overline{v} / v_0$ between 2D and 3D models. v_0 is the drift velocity of a helix aligned with the flow ($\theta = 0$, $\psi = \pi/2$). (Marcos et al. 2009).

Pe	0.01	0.1	1	10	100	1000	10000	40000
$\overline{v}_{3D} / v_0$	0.0000	0.0001	0.0137	0.3063	0.6532	0.8255	0.9236	0.9508
$\overline{v}_{2D} / v_0$	0.0000	0.0003	0.0289	0.4169	0.7275	0.8722	0.9377	0.9571

3.3 Application to chiral separation

Many biochemically active molecules are naturally chiral and can only bind to target chiral molecules of a specific handedness (Ahuja 1997). The other enantiomer (i.e., the molecule having opposite handedness) may be inactive or cause undesirable effects. Chemical synthesis of chiral molecules usually produces a racemic mixture, with equal amounts of both enantiomers, and their separation based on chirality is of importance in fields ranging from agriculture to food and pharmaceutical industries. Currently favored approaches rely on gas, liquid, or capillary electromigration chromatography (Scriba 2008), requiring costly chiral media. Thus, simpler, alternative approaches to chiral separation are desirable.

Several alternative proposals for chiral separation exploit hydrodynamic forces. Some of these, yet untested experimentally, rely on the presence of a surface (de Gennes 1999) or array of microvortices (Kostur et al. 2006), while there has been successful chiral separation of centimeter-sized crystals in a rotating drum (Howard et al. 1976). Other methods (Kim and Rae 1991; Makino and Doi 2005) stem from the prediction that a chiral particle in a simple shear flow experiences a lateral drift (Brenner 1964). However, the feasibility of this approach has remained questionable, as measurements in Couette cells reported that the drift of millimeter-sized chiral objects (Makino et al. 2008) and the forces on centimeter-sized ones (Chen and Chao 2007) differ from predictions by 2 orders of magnitude (Makino et al. 2008) or even in sign (Chen and Chao 2007).

Here we report that microscale chiral objects, 3 orders of magnitude smaller than previous studies (Makino et al. 2008; Chen and Chao 2007), experience a lateral drift in a microfluidic shear flow, and that the magnitude of the drift is in agreement with our theory. Previous work has demonstrated the ability of microfluidics to separate and sort colloids by size (Di Carlo et al. 2007), spermatozoa by motility (Cho et al. 2003), and microbes by their preference for dissolved chemicals (Stocker et al. 2008). Our method uses microchannels to sort particles by chirality (See section 3.2). We have shown that an

enantiomer (right-handed spirochete) drifts with direction determined by the local shear, demonstrate the feasibility of this method for chiral separation, and indicate how the high shear rates achievable in microchannels (>10^6 s^{-1} (Kang et al. 2005)) allow our method to be extended to smaller scales (<40 nm).

For chirality-induced separation to take place, preferential alignment of helices with the flow is required. In our experiments, spirochetes were aligned hydrodynamically via Jeffery orbits. For smaller particles, rotational Brownian motion is more effective at randomizing orientation. To determine the size of the smallest helical particles that can be separated in this manner, we find the steady distribution for helices with $r = 70$ and length L. The mean drift velocity $\overline{v}$ is uniquely determined by the Peclet number Pe = $\dot{\gamma}/D_R$ (Fig. 3-11, inset). For Pe >> 1, alignment by shear dwarfs rotational diffusion and $\overline{v} \approx v_0$, where v_0 is the drift velocity of a helix aligned with the flow. Our experiments are in this limit, with Pe ≈ 4×10^4 ($\dot{\gamma} \approx 103$ s^{-1} at $y = H/4$). In contrast, for Pe < 10, diffusion destroys the alignment and $\overline{v} \to 0$. Assuming isometrically scaled helices of length L, D_R scales as L^{-3}, decreasing Pe for smaller helices. This can be partially counteracted by increasing $\dot{\gamma}$, but the particle Reynolds number Re = $\dot{\gamma}L^2/\nu$ (Di Carlo et al. 2007) must remain small (Re << 1) to operate in the Stokes regime. Hence, as L decreases, $\dot{\gamma}$ can be increased as L^{-2}. The competition between Pe and Re determines the smallest helices that can be separated for a given shear rate, which we estimate as $L \approx 20$, 80, and 400 nm for $\dot{\gamma} \approx 10^8$, 10^6, and 10^4 s^{-1}, respectively (Fig. 3-11, open symbols). Shear rates as high as 10^6 s^{-1} have been reported (Kang et al. 2005) in microchannels, and current technology allows pressure heads of 2×10^8 Pa (Microfluidics Corp., Newton, MA), such that a 10 μm deep, 5 cm long channel could generate shear rates of 10^7 s^{-1}, sufficient to separate 40 nm particles.

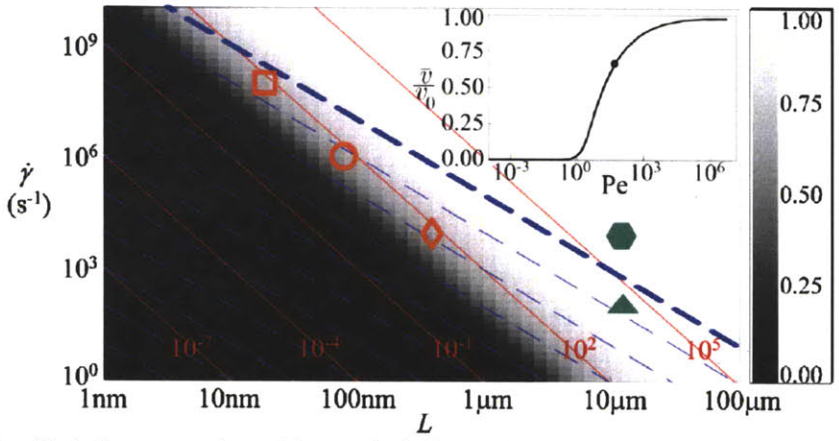

Figure 3-11. Size limit for separation of isometric helices of length L and equivalent aspect ratio $r = 70$. Dashed contours show constant Re (spaced by a factor of 10) and the thick contour is Re = 0.1. Solid contours show constant Pe. The gray scale shows $\overline{v}/v_0$, where v_0 is the drift velocity of a helix aligned with the flow. The smallest helices which can be separated for a given shear rate, determined by $\overline{v}/v_0 = 0.66$ (Pe = 50, marked by circle on inset) and Re < 0.1, have $L \approx 20$ (square), 80 (circle), and 400 nm (diamond) for $\dot{\gamma}$ = 10^8, 10^6, and 10^4 s^{-1}, respectively. Full symbols mark the parameter regimes of our experiments: Re = 0.03 (triangle) and Re = 5 (hexagon). Inset: $\overline{v}/v_0$ vs Pe. (Marcos et al. 2009).

While we have demonstrated the lateral drift of chiral objects, one is ultimately interested in separating a mixture of enantiomers. Because the top and bottom halves of the channel produce drift in opposite directions, a racemic mixture would separate into four quadrants, with opposite quadrants containing the same enantiomer. While we believe our technique represents a significant step forward in enabling reliable chiral separation by shear, it remains to be seen whether it can extend to the molecular scale (<10 nm). To this end, in addition to increasing shear rates via improved manufacturing techniques, it will be interesting to explore the feasibility of using alternative alignment mechanisms to counteract rotational diffusion. One could operate at higher Reynolds number: preliminary experiments show successful separation at Re = 5, but further research is required to elucidate the role of inertia on separation and any constraints on microchannel operation, such as Dean vortices and performance under high pressure. Finally, not all chiral particles are helical, so it would be useful to understand what geometries lead to the best separation.

3.4 Summary

In this chapter, we develop a model based on resistive force theory to study the dynamics of a helix in a simple shear flow. We find that shear flow produces a lift force on chiral objects such as a helix. This provides a novel mechanism for transport across streamlines in low Reynolds number. We verify this prediction by exposing a non-motile helical bacterium in plane parabolic shear. The experiments are in good agreement with the theoretical prediction. We discuss the application of such microfluidic setup in separating chiral particles relevant to agricultural and pharmaceutical industries.

For typical flagellated bacteria, the magnitude of this drift velocity is much smaller (~ 0.7 $\mu m\ s^{-1}$, when exposed to shear rate of 10 s^{-1}) than typical swimming speed of bacteria (~ 50 $\mu m\ s^{-1}$). However, with the addition of a head, the chirality-dependent forces that lead to a lateral drift also lead to a reorienting torque. We shall see in chapter 4 that the drift velocity induced by chiral *reorientation* can be of the same order as the swimming speed.

Chapter 4

Bacteria swimming in a shear flow

We have seen in the previous chapter that the interaction between shear flow and a chiral object, such as a helical flagellum, results in a lateral lift force, and therefore a lateral drift. Here we show that the presence of the cell head results in a novel phenomenon: chiral forces induce not only a lateral drift, but also a reorienting torque on bacteria. This reorientation can qualitatively change swimming trajectories. Without chiral reorientation, the drift velocity is small, but when chiral reorientation is accounted for, the drift velocity becomes of the same order as the swimming speed. Because swimming and reorientation are central to the chemotaxis used by many bacteria for foraging, it is important to understand under what environmental conditions chiral reorientation affects motility. In this chapter, a theoretical and experimental investigation of a swimming bacterium in a shear flow is presented. Experimental observations of the motile bacteria *Bacillus subtilis* exposed to microfluidic shear flows revealed a clear bacteria drift velocity across streamlines. These results were in good agreement with the theoretical prediction. Finally, to confirm whether the observations are purely hydrodynamics effects, we present a separate experiment to probe bacterial ability to actively response to shear.

4.1 Model formulation

In the simplest form, a bacterium can be modeled as a rigid helix attached to a spherical head (Fig. 4-1). To make the problem analytically tractable, we study the hydrodynamics around the head and the flagellum separately, neglecting the hydrodynamic interactions between the two. This is a good approximation as long as the length of the flagellum is much larger than the diameter of the head (Childress 1981).

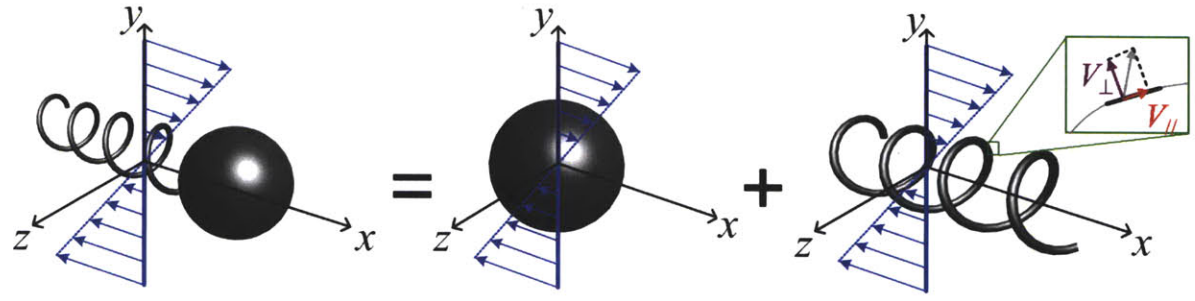

Figure 4-1. Schematic of a bacterium in a simple shear flow.

Consider a sphere of radius a in a simple shear flow $\mathbf{V} = (\dot{\gamma} y, 0, 0)$. The center of the sphere in the inertial frame is $\mathbf{x}_0 = (x_G, y_G, z_G)$ and the linear and angular velocities of the center of the sphere are $\mathbf{v} = (v_x, v_y, v_z)$ and $\boldsymbol{\omega} = (\omega_x, \omega_y, \omega_z)$, respectively. The total hydrodynamic force and torque due to the shear flow on the sphere are

$$\begin{pmatrix} \mathbf{F} \\ \mathbf{M} \end{pmatrix} = \{\xi\} \begin{pmatrix} \mathbf{v} \\ \boldsymbol{\omega} \end{pmatrix} + \{B\} \tag{4.1}$$

where

$$\{\xi\} = -\begin{pmatrix} C_F & 0 & 0 & 0 & 0 & 0 \\ 0 & C_F & 0 & 0 & 0 & 0 \\ 0 & 0 & C_F & 0 & 0 & 0 \\ 0 & 0 & 0 & C_M & 0 & 0 \\ 0 & 0 & 0 & 0 & C_M & 0 \\ 0 & 0 & 0 & 0 & 0 & C_M \end{pmatrix} \qquad \{B\} = \begin{pmatrix} y_G C_F \\ 0 \\ 0 \\ 0 \\ 0 \\ -\dot{\gamma} C_M \end{pmatrix}$$

and $C_F = 6\pi\mu a$ and $C_M = 8\pi\mu a^3$ (Happel and Brenner 1965).

Here, $\{\xi\}$ and $\{B\}$ are the resistance matrix and the matrix capturing the effect of shear on the sphere. The translational drag of the sphere in shear flow is the same as in uniform flow, and that the effect of shear flow on rotational drag is to change the rotational rate by the vorticity.

The dynamics of a bacterium swimming in a shear flow can be obtained by adding the total forces and torques on the helix and the sphere and equating them to zero. We computed the hydrodynamic forces and torques due to the shear flow on a helix using resistive force theory (RFT), as shown Chapter 3 (Eq. (3.12)). It should be noted that the linear velocities in Eq. (3.12) are computed at the center of the helix. Therefore, before we can add the total forces and torques on the helix and the sphere, we need to choose one and the same point where to compute velocities for both the helix and the sphere. For convenience, we shall choose the center of the sphere to be the location where we calculate the linear velocities of the bacterium. This will also facilitate comparison with experiments, since the flagellum is not visible under light microscopy.

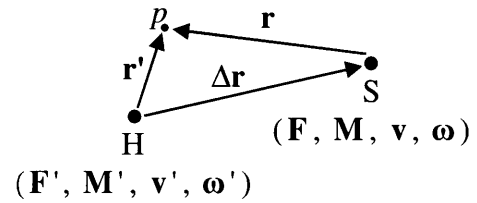

Figure 4-2. Sketch showing the center of the helix (H) and the center of the sphere (S), which are separated by a distance $\Delta\mathbf{r}$ in 3D space. p is a general point on the helix.

Let us denote the quantities computed at the center of the helix with an apostrophe and those computed at the center of the sphere without an apostrophe (Fig. 4-2). Therefore the forces and the torques are related by the following expression

$$\mathbf{F}' = \int \mathbf{f}'(\mathbf{r}')d\mathbf{r}' \qquad : \qquad \int \mathbf{f}(\mathbf{r})d\mathbf{r} = \int \mathbf{f}'(\mathbf{r}')d\mathbf{r}' \;\rightarrow\; \mathbf{F} = \mathbf{F}'$$

Note that $d\mathbf{r} = d\mathbf{r}'$ and $\mathbf{r} + \Delta\mathbf{r} = \mathbf{r}'$

$$\mathbf{M}' = \int \mathbf{r}' \times \mathbf{f}'(\mathbf{r}')d\mathbf{r}' \quad : \quad \mathbf{M} = \int \mathbf{r} \times \mathbf{f} d\mathbf{r} = \int \left[(\mathbf{r}' \times \mathbf{f}) - (\Delta\mathbf{r} \times \mathbf{f}) \right] d\mathbf{r}, \qquad \text{note } \mathbf{f} = \mathbf{f}'$$
$$\mathbf{M} = \mathbf{M}' - \Delta\mathbf{r} \times \mathbf{F}$$

Or, in matrix form:

$$\begin{pmatrix} \mathbf{F} \\ \mathbf{M} \end{pmatrix} = \begin{pmatrix} 1 & 0 \\ -\Delta\mathbf{r}\times & 1 \end{pmatrix} \begin{pmatrix} \mathbf{F}' \\ \mathbf{M}' \end{pmatrix} \tag{4.2}$$

For a rigid body motion, the kinematics are related by $\boldsymbol{\omega} = \boldsymbol{\omega}'$ and $\mathbf{v} = \mathbf{v}' + \boldsymbol{\omega} \times \Delta\mathbf{r}$:

$$\begin{pmatrix} \mathbf{v} \\ \boldsymbol{\omega} \end{pmatrix} = \begin{pmatrix} 1 & -\Delta\mathbf{r}\times \\ 0 & 1 \end{pmatrix} \begin{pmatrix} \mathbf{v}' \\ \boldsymbol{\omega}' \end{pmatrix} \qquad \text{or} \qquad \begin{pmatrix} \mathbf{v}' \\ \boldsymbol{\omega}' \end{pmatrix} = \begin{pmatrix} 1 & \Delta\mathbf{r}\times \\ 0 & 1 \end{pmatrix} \begin{pmatrix} \mathbf{v} \\ \boldsymbol{\omega} \end{pmatrix} \tag{4.3}$$

Using the convention in Fig. 4-2, Eq. (3.12) becomes

$$\begin{pmatrix} \mathbf{F}' \\ \mathbf{M}' \end{pmatrix} = \{\zeta'\} \begin{pmatrix} \mathbf{v}' \\ \boldsymbol{\omega}' \end{pmatrix} + \{A'\} \tag{4.4}$$

Multiplying Eq. (4.4) with $\begin{pmatrix} 1 & 0 \\ -\Delta\mathbf{r}\times & 1 \end{pmatrix}$ and using Eq. (4.3), we obtain

$$\begin{pmatrix} \mathbf{F} \\ \mathbf{M} \end{pmatrix} = \{\zeta\} \begin{pmatrix} \mathbf{v} \\ \boldsymbol{\omega} \end{pmatrix} + \{A\} \tag{4.5}$$

where

$$\{\zeta\} = \begin{pmatrix} 1 & 0 \\ -\Delta\mathbf{r}\times & 1 \end{pmatrix} \{\zeta'\} \begin{pmatrix} 1 & \Delta\mathbf{r}\times \\ 0 & 1 \end{pmatrix} \qquad \text{and} \qquad \{A\} = \begin{pmatrix} 1 & 0 \\ -\Delta\mathbf{r}\times & 1 \end{pmatrix} \{A'\} \tag{4.6}$$

Here $\{\zeta\}$ and $\{A\}$ are the resistance matrix and the matrix capturing the effect of shear on the helix calculated at the center of the sphere with respect to the inertial frame *oxyz*. Since the sphere is connected to the helix, $\Delta\mathbf{r} = [T_{Euler}]^{tr}(0, 0, a + l\cos(\alpha)/2)$, where $[T_{Euler}]$ is the Euler rotation matrix of the cell body given by Eq. (3.6).

Due to the small Reynolds number of the flow, inertia is negligible and the total forces and torques must equate to zero.

$$\begin{pmatrix} \mathbf{F} \\ \mathbf{M} \end{pmatrix}_{helix} + \begin{pmatrix} \mathbf{F} \\ \mathbf{M} \end{pmatrix}_{sphere} = 0 \tag{4.7}$$

We apply kinematic boundary conditions such that the flagellum is moving together with the head and the flagellum is rotating along the axis of the cell relative to the head:

$$\begin{pmatrix} \mathbf{v} \\ \boldsymbol{\omega} \end{pmatrix}_{helix} = \begin{pmatrix} \mathbf{v} \\ \boldsymbol{\omega} \end{pmatrix}_{sphere} + \begin{pmatrix} 0 \\ \boldsymbol{\omega} \end{pmatrix}_{rel} \tag{4.8}$$

where $\boldsymbol{\omega}_{rel} = [T_{Euler}]^{tr}\ (0,\ 0,\ \omega_{rel})$ is the angular rotation rate of the flagellum relative to the cell body along the axis of the cell.

Substituting Eqs. (4.1) and (4.5) into Eq. (4.7) and employing Eq. (4.8), we obtain

$$\{\zeta\}\left[\begin{pmatrix} \mathbf{v} \\ \boldsymbol{\omega} \end{pmatrix}_{sphere} + \begin{pmatrix} 0 \\ \boldsymbol{\omega} \end{pmatrix}_{rel}\right] + \{A\} + \{\xi\}\begin{pmatrix} \mathbf{v} \\ \boldsymbol{\omega} \end{pmatrix}_{sphere} + \{B\} = 0$$

$$\begin{pmatrix} \mathbf{v} \\ \boldsymbol{\omega} \end{pmatrix}_{sphere} = -\left[\{\zeta\} + \{\xi\}\right]^{-1}\{\zeta\}\begin{pmatrix} 0 \\ \boldsymbol{\omega} \end{pmatrix}_{rel} - \left[\{\zeta\} + \{\xi\}\right]^{-1}\left[\{A\} + \{B\}\right] \tag{4.9}$$

We have seen in chapter 3 that in addition to rotating in a Jeffery orbit, a helix drifts across streamlines, due to its chirality. With the addition of a head, the chirality-dependent forces that lead to a lateral drift also lead to a reorienting torque (Fig. 4-3a). When the bacterium is aligned with the shear flow in the x direction, the same force which results in chirality-dependent drift acts upon the helical flagellum in the z direction. The non-chiral cell head acts as an anchor and thus experiences drag in the opposite direction. This results in a torque on the swimmer (Fig. 4-3a) and reorients the cell away from the x direction (Fig. 4-3b). We saw in chapter 3 that the lateral drift velocity of a typical flagellum due to the chiral force (~ 0.7 μm/s) is much smaller than typical swimming speeds of bacteria (~ 50 μm/s). The magnitude of this lateral drift velocity V is rather small compared to a typical swimming speed of many bacteria. In contrast, we will see that the drift velocity induced by chiral *reorientation* can be of the same order as the swimming speed U. Furthermore, the reorientation induced drift is in the opposite direction to the chiral-force induced drift.

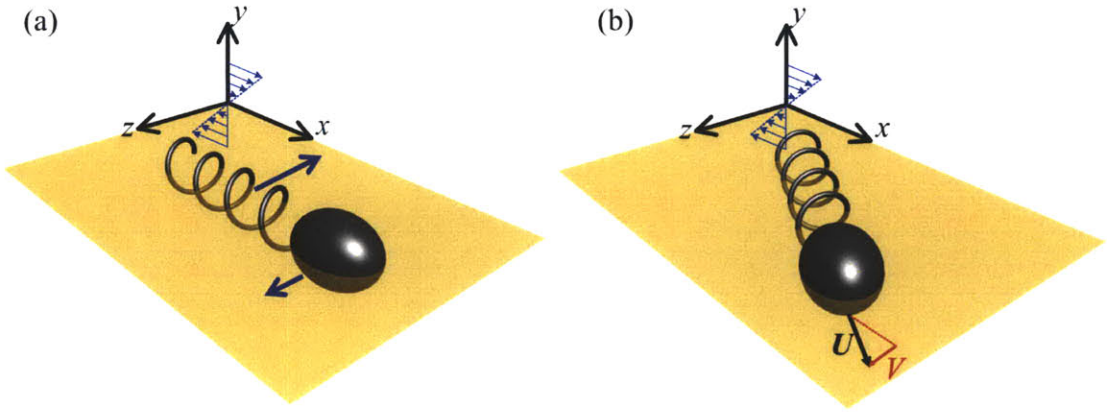

Figure 4-3. a) The chirality-induced lateral drift force on a right-handed helical flagellum and the drag on the cell head lead to a reorienting torque on a bacterium. b) This chiral torque causes a swimming bacterium to preferentially point away from the x direction and thus to experience a net drift velocity V that is of the same order as the swimming velocity U.

To demonstrate that this effect is a direct result of the coupling of chirality, motility and shear, we compare the net drift velocity among three populations: swimming bacteria, non-swimming bacteria, and swimming ellipsoids (hypothetical non-chiral swimmers). As described in chapter 3, the net drift on a chiral object depends on the distribution of the orientation of the object relative to the flow. When the object is preferentially aligned with streamlines, for example due to Jeffery orbits, it has a net drift. When all orientations are equally likely, for example due to strong Brownian rotational diffusion, the net drift is zero. Incorporating the effect of Brownian rotational diffusivity, we solved the Fokker-Plank equation to compute the three-dimensional probability distribution $c(\psi,\theta)$ of the orientations of the bacteria (see also Section 3.2.3):

$$\partial_t c = D_R \nabla^2 c - \nabla \cdot \left(\dot{\boldsymbol{\omega}} c \right) \tag{3.16}$$

where D_R is the Brownian rotational diffusivity and $\dot{\boldsymbol{\omega}} = \dot{\psi}\hat{\mathbf{e}}_\psi + \dot{\theta}\hat{\mathbf{e}}_\theta$.

To model a swimming prolate ellipsoid, we prescribe a constant forward swimming velocity along the ellipsoid's major axis. The angular velocities $\dot{\boldsymbol{\omega}}$ are obtained from the Jeffery orbit angular velocities, Eqs. (3.3) and (3.17). The Brownian rotational diffusivity D_R is estimated by using the Stokes-Einstein equation $D_R = kT/\zeta_{ell}^{T\perp}$, where $\zeta_{ell}^{T\perp}$ is the torsional resistive coefficient of an ellipsoid perpendicular to its major axis (Steinberger et al. 1994):

$$\zeta_{ell}^{T\perp} = \frac{16\pi\mu\left(b_{ell}^2 + a_{ell}^2\right)}{3\left(b_{ell}^2\beta_0 + a_{ell}^2\alpha_0\right)} \tag{4.10}$$

where a_{ell} and b_{ell} are the half major and minor axis length of the ellipsoid, respectively, α_0 and β_0 are given by

$$\alpha_0 = -\frac{2}{e_{ell}^2 a_{ell}} - \frac{1}{e_{ell}^3}\ln\frac{a_{ell}-e_{ell}}{a_{ell}+e_{ell}} \qquad \beta_0 = \frac{a_{ell}}{e_{ell}^2 b_{ell}^2} + \frac{1}{2e_{ell}^3}\ln\frac{a_{ell}-e_{ell}}{a_{ell}+e_{ell}} \tag{4.11}$$

and $e_{ell} = \sqrt{a_{ell}^2 - b_{ell}^2}$ is the ellipsoid's eccentricity.

For both swimming and non-swimming bacteria, $D_R = kT/(\zeta_{55} + \xi_{55})$. Here $\dot{\boldsymbol{\omega}}$ can be obtained from the angular velocities $\boldsymbol{\omega}$ solved in Eq. (4.9) by realizing that (see section 3.1.2 on Euler angles):

$$\begin{pmatrix}\omega_x\\ \omega_y\\ \omega_z\end{pmatrix} = \begin{bmatrix}0 & -\sin\theta & \sin\psi\cos\theta\\ 0 & \cos\theta & \sin\psi\sin\theta\\ 1 & 0 & \cos\psi\end{bmatrix}\begin{pmatrix}\dot{\theta}\\ \dot{\psi}\\ \dot{\phi}\end{pmatrix} \tag{4.12}$$

or

$$\begin{pmatrix}\dot{\theta}\\ \dot{\psi}\\ \dot{\phi}\end{pmatrix} = \begin{bmatrix}-\cot\psi\cos\theta & -\cot\psi\sin\theta & 1\\ -\sin\theta & \cos\theta & 0\\ \operatorname{cosec}\psi\cos\theta & \sin\theta\sin\theta & 0\end{bmatrix}\begin{pmatrix}\omega_x\\ \omega_y\\ \omega_z\end{pmatrix} \tag{4.13}$$

The steady-state solution ($\partial_t c = 0$) for $c(\psi,\theta)$ was obtained numerically (using COMSOL Multiphysics) and the net drift velocity V was computed as

$$V = \int_0^{2\pi}\int_0^{\pi} v_z(\psi,\theta)c(\psi,\theta)\sin\psi\, d\psi\, d\theta \tag{4.14}$$

The net drift velocities of swimming bacteria, non-swimming bacteria, and swimming ellipsoids populations are shown in Fig. 4-4.

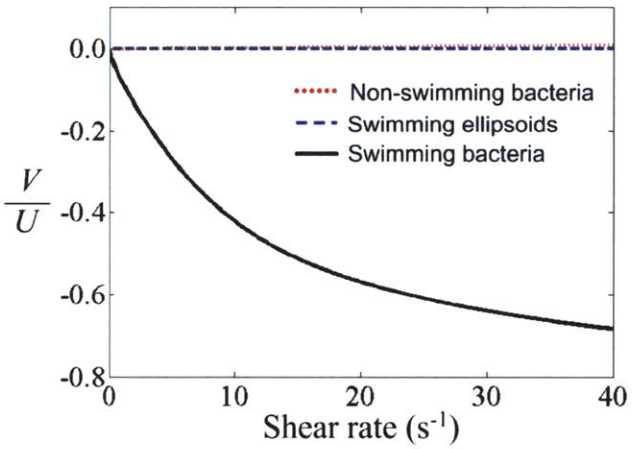

Figure 4-4. Net drift velocity (V) of a population of swimming bacteria (black solid line), swimming ellipsoids (blue dashed line), and non-swimming bacteria (red dotted line) in a simple shear flow. The drift velocities of the three populations were normalized with the swimming speed of bacteria (U = 50 μm/s). The bacteria were modeled by assuming a 1 μm radius spherical head and a left-handed helical flagellum with 4 turns, pitch angle of 41°, and axial length of 10 μm, corresponding to the flagellar bundle of *E. coli*. For swimming bacteria, the angular rotation rate of the flagellum relative to the cell body ω_{rel} = 127 Hz.

In the absence of flow (zero shear rate), all swimmers are uniformly distributed in all orientations and thus have zero net drift velocity (i.e. velocity along the z axis). In the presence of shear, swimming ellipsoids (non-chiral swimmers) undergo Jeffery orbits and preferentially align with the flow (i.e. the x-z plane). Even though swimming ellipsoids are able to swim across streamlines, there is equal probability of swimming in the $+z$ and $-z$ directions. Therefore, the net drift velocity of the ellipsoid population is always zero, regardless of the shear rate or the size of the ellipsoid (Fig. 4-4, dashed blue line). On the other hand, when a population of bacteria is exposed to shear, in addition to undergoing Jeffery orbits, they experience a lateral drift in the $+z$ direction (for a left-handed flagellum) and a chiral torque that preferentially reorients them to point towards the $-z$ direction. Due to the chiral drift force, non-swimming bacteria will drift in the $+z$ direction (red dotted line). Note that the magnitude of the drift velocity due to the chiral drift force is much smaller than a typical swimming speed of a bacterium, as noted at the end of Chapter 3. As detailed above, addition of a head results in a chiral torque and, if bacteria are swimming, this translates to a lateral drift (black solid line) that has opposite sign and considerably larger magnitude compared to the chiral-force induced drift (red dotted line). Therefore, due to the chiral reorientation, swimming bacteria with a left-handed flagellum are predicted to drift considerably in the $-z$ direction (Fig. 4-4). The net drift velocity increases with the shear rate, due to stronger preferential alignment and chiral reorientation at larger shear rates, and can be of the same order as the swimming speed, with $V/U = 9\%$ at $\dot{\gamma} = 1$ s^{-1}, $V/U = 47\%$ at $\dot{\gamma} = 10$ s^{-1}, and $V/U = 63\%$ at $\dot{\gamma} = 30$ s^{-1}.

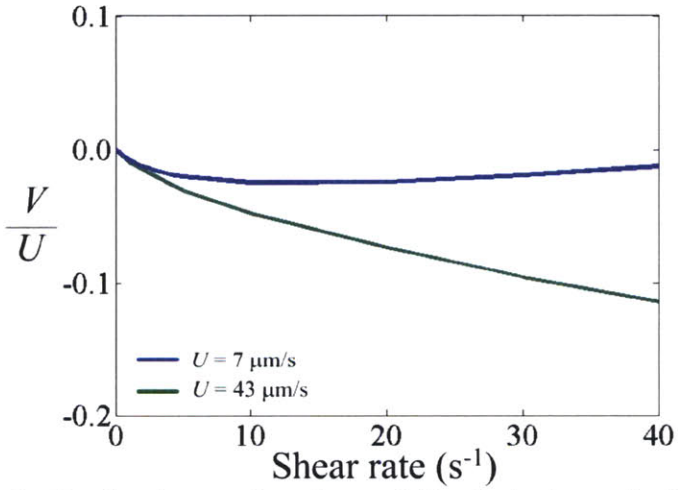

Figure 4-5. Effects of cell swimming speed on the net drift velocity (normalized with average swimming speed) under various shear rates. The model assumes a 0.2 μm radius spherical head and a left-handed helical flagellum with 3 turns, pitch angle of 37°, and axial length of 6 μm, corresponding to the flagellar bundle *B. subtilis*.

The net drift velocity does not increase indefinitely with shear rate, because there is a maximum alignment and reorientation when Brownian diffusivity becomes unimportant (i.e. at large Peclet numbers, $Pe = \dot{\gamma}/D_R >> 1$). However, the net drift velocity will not hit a plateau either. When the shear rate becomes really large, increasing the shear rate will increase the chiral drift force enough that the drift velocity in the $+z$ direction due to the

chiral force on the flagellum becomes of the same order as the drift velocity in the $-z$ direction due to the chiral torque on the entire organism. When this happens, the net drift velocity will decrease. This effect is evident at lower shear rates for slow swimming cells (Fig. 4-5, blue line), compared to faster swimming cells of the same morphology (Fig. 4-5, green line).

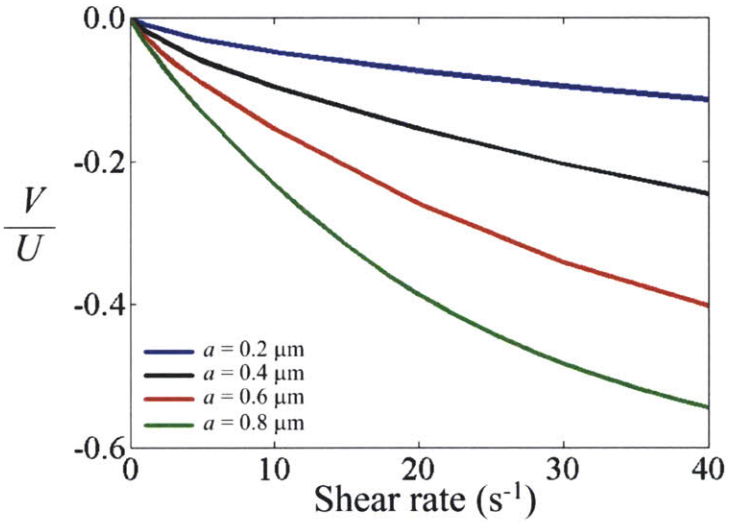

Figure 4-6. Effect of head size on the net drift velocity, normalized with the swimming speed U, as a function of the shear rate. The model assumes a left-handed helical flagellum with 3 turns, pitch angle of 37°, and axial length of 6 μm, corresponding to the flagellar bundle of *B. subtilis*. In all cases, $U = 50$ μm/s.

Because the chiral torque stems from the presence of the head, it is interesting to consider the effect of the head's size on the drift velocity for given swimming speed (Fig. 4-6). We find, as one would expect, that a larger head induces a larger chiral torque and thus a larger net drift velocity. In addition to a larger torque, a larger head also reduces the Brownian rotational diffusivity of the bacterium and thus larger Peclet number for a given shear rate, allowing larger drift velocity for low shear rates.

4.2 The effect of tumbling

The discussion presented above is based on the assumption that the bacteria are smooth swimmers and do not tumble. In other words, they only and always swim forward and disperse by means of Brownian reorientation. Many bacteria, such as *Escherichia coli* and *Bacillus subtilis*, adopt a "run and tumble" swimming strategy. During runs, the bacterium swims along a straight path, and its flagella are bundled together behind the cell. Near the end of a run, one or more motors reverses, and the flagella unwind from the bundle, which allows the cell to change its swimming direction (tumble). Once the motors reverse again, the bundle re-forms, and the cell swims in a new direction, performing a new run.

A Monte Carlo simulation of a population of bacteria was performed. The position $\mathbf{x}_0$ and orientation $\boldsymbol{\theta}_0$ of each bacterium can be obtained as follows:

$$\begin{pmatrix} \mathbf{x}_0 \\ \boldsymbol{\theta}_0 \end{pmatrix}_{t+dt} = \begin{pmatrix} \mathbf{x}_0 \\ \boldsymbol{\theta}_0 \end{pmatrix}_t + \begin{pmatrix} \mathbf{v} \\ \dot{\boldsymbol{\omega}} \end{pmatrix}_t dt + \begin{pmatrix} \mathbf{v}_{rdm} \\ \dot{\boldsymbol{\omega}}_{rdm} \end{pmatrix}_t dt \tag{4.15}$$

where dt is the time step of the simulation, $\mathbf{v}$ is the linear velocity of the bacterium, $\dot{\boldsymbol{\omega}}$ is the angular velocity satisfying Eq. (4.13), $\mathbf{v}_{rdm}$ and $\dot{\boldsymbol{\omega}}_{rdm}$ are the linear and rotational velocities due to Brownian diffusion.

The deterministic velocity of the swimming bacteria is given by Eq. (4.9), which can also be written as

$$\begin{pmatrix} \mathbf{v} \\ \boldsymbol{\omega} \end{pmatrix} = -\left[\{\zeta\} + \{\xi\}\right]^{-1} \begin{pmatrix} \mathbf{F} \\ \mathbf{M} \end{pmatrix}$$

or

$$\begin{pmatrix} \mathbf{v} \\ \boldsymbol{\omega} \end{pmatrix} = \{\mu\} \begin{pmatrix} \mathbf{F} \\ \mathbf{M} \end{pmatrix} \tag{4.16}$$

where $\{\mu\} = \begin{pmatrix} \boldsymbol{\mu}_{\mathbf{FF}} & \boldsymbol{\mu}_{\mathbf{FM}} \\ \boldsymbol{\mu}_{\mathbf{FM}} & \boldsymbol{\mu}_{\mathbf{MM}} \end{pmatrix}$ is the 6x6 symmetric mobility matrix.

The random motion due to Brownian translational and rotational diffusion was modeled by the velocity vectors $\mathbf{v}_{rdm}$ and $\boldsymbol{\omega}_{rdm}$. These random vectors obey the Gaussian distribution characterized by (Makino and Doi 2005)

$$\begin{aligned} \langle \mathbf{v}_{rdm}(t) \rangle &= 0 \qquad \langle \boldsymbol{\omega}_{rdm}(t) \rangle = 0 \\ \langle \mathbf{v}_{rdm}(t) \mathbf{v}_{rdm}(t') \rangle &= 2kT\boldsymbol{\mu}_{\mathbf{FF}} \delta(t-t') \\ \langle \mathbf{v}_{rdm}(t) \boldsymbol{\omega}_{rdm}(t') \rangle &= 2kT\boldsymbol{\mu}_{\mathbf{FM}} \delta(t-t') \\ \langle \boldsymbol{\omega}_{rdm}(t) \boldsymbol{\omega}_{rdm}(t') \rangle &= 2kT\boldsymbol{\mu}_{\mathbf{MM}} \delta(t-t') \end{aligned}$$

where k is the Boltzmann constant, T is the temperature, $\delta(t-t')$ is a delta function, and the notation $\langle\ \rangle$ indicates an integral average over all time. These conditions essentially reinstate the features of Brownian diffusivity: (i) the average linear and angular velocities are zero; (ii) thermal fluctuations lead to Gaussian-distributed random velocity which is uncorrelated in time. The width of the Gaussian distributions is related to the mobilities $\boldsymbol{\mu}$ via the Stokes-Einstein relation $kT\boldsymbol{\mu}$.

These random vectors can be obtained by calculating the eigenvalues and eigenvectors of the mobility matrix $\{\mu\}$. This would give us

$$\begin{pmatrix} \mathbf{v}_{rdm} \\ \boldsymbol{\omega}_{rdm} \end{pmatrix} = rdm_1\, \mathbf{u}_1 + rdm_2\, \mathbf{u}_2 + rdm_3\, \mathbf{u}_3 + rdm_4\, \mathbf{u}_4 + rdm_5\, \mathbf{u}_5 + rdm_6\, \mathbf{u}_6 \tag{4.17}$$

where $\mathbf{u}_i$ (i = 1, 2, ...6) are the eigenvectors and rdm_i are the Gaussian distributed random scalar numbers generated at every time step with a variance of $2kT\hat{\mu}_i$, where $\hat{\mu}_i$ are the corresponding eigen-numbers.

To model run-and-tumble, we calculate the tumbling probability $P_{tumble} = dt/\tau$ (Berg 2004), where τ is the mean run time (~1 s for *E. coli*). We then generate a uniformly distributed random number $R_{uniform}$ at every time step of the simulation. If $P_{tumble} > R_{uniform}$, the cell tumbles, otherwise the cell continues along the current run. The tumble angle is taken from a Gaussian distribution. For *E. coli*, the average change in tumbling angle (measured relative to the current swimming direction) is 68°, with a standard deviation of 39° (Berg and Brown 1972).

We find that the net effect of tumbles is to decrease the drift velocity (Fig. 4-7). Importantly, however, the drift still exists, despite the tumbles. The decrease in net drift is due to the fact that a tumble destroys the alignment induced by shear, increasing randomness and thus favoring a more isotropic distribution of orientations. Therefore, given the same morphology, smooth swimming bacteria (i.e. no tumble) would experience the maximum drift velocity than the ones that tumble. The more frequent they tumble, the smaller drift velocity they experience. In the limit that they always tumble, the net drift velocity will reduce to zero.

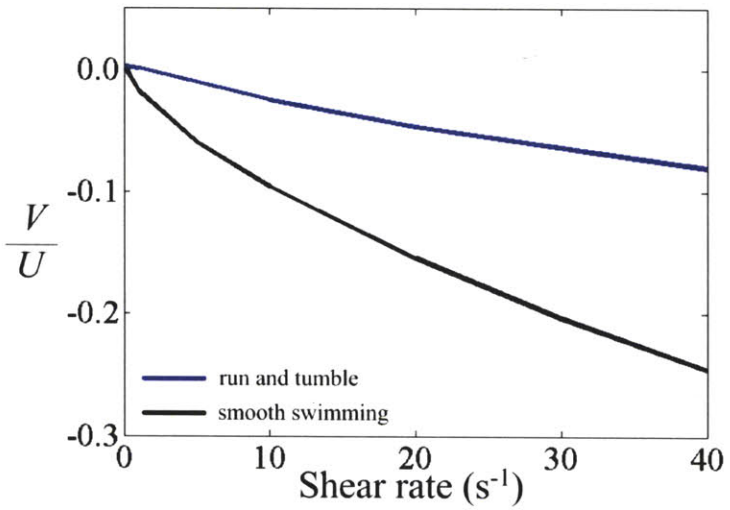

Figure 4-7. The effect of tumbles on the drift velocity. The net drift velocity (V) of a population of smooth-swimming bacteria (black) and run-and-tumble bacteria (blue). Effects of Brownian rotation are included in the model. The bacteria were modeled by assuming a 0.4 μm radius spherical head and a left-handed helical flagellum with 3 turns, pitch angle of 37°, and axial length of 6 μm, corresponding to the flagellar bundle of *B. subtilis*. The angular rotation rate of the flagellum relative to the cell body ω_{rel} = 250 Hz, giving swimming speed U = 50 μm/s. The run-and-tumble swimmer had an average change direction of 68° and a standard deviation of 39° with mean run time τ= 1 s.

4.3 Experimental verification

4.3.1 Experimental setup

We used a smooth-swimming strain of the bacterium *Bacillus subtilis*, strain OI4139 (Szurmant et al. 2004). The cell has an ellipsoidal head with average size of 1×3 μm. During normal swimming mode, the flagella of this bacterium form a 3-turn left-handed helical bundle with axial length of 6 μm and diameter of 480 nm (Fujii et al. 2008). The bacteria are grown using Cap assay minimal media (Zimmer et al. 2002), as described in the Appendix.

To expose bacteria to a shear flow, we used a 110 cm long, serpentine-shaped microfluidic channel (Figs. 4-8a,b), similar but not identical to what done before (see sections 2.1.1 and 3.2.1). In this experiment, we use only one inlet (instead of two) to continuously inject bacteria into the channel. The channel has a rectangular cross section with large aspect ratio (width/height = 1000μm/90μm = $W/H \approx 11$; Fig. 4-8a), such that the flow is uniform across the width, except for a 150 μm thick boundary layer at the sidewalls (Doshi et al. 1978). Across the channel depth (far from the side walls) the flow has a parabolic profile, $u(y) = (3U_F/2)[1-(2y/H)^2]$, where U_F is the average flow speed, leading to a shear rate which varies linearly over depth, $\dot{\gamma}(y) = du/dy = -12yU_F/H^2$. The shear rate is therefore negative in the top half of the channel and positive in the bottom half. We performed experiments at various flow speeds, resulting in shear rates ranging from 0 to 36 s^{-1}.

We imaged the bacteria using phase contrast microscopy with a 40× long-working distance objective (NA = 0.6) and a CCD camera (PCO 1600, Cooke, Romulus, MI). At a fixed location ~ 1 m downstream from the inlet (Fig. 4-8b, blue squared box), 25 sets of 1000 images were recorded at 8.2 ms intervals at a quarter depth, $y = -H/4$ from the midplane. This was repeated for each shear rate. We assayed 11 shear rates: 0, 2, 4, 6, 8, 10, 15, 21, 26, 31, and 36. Six independent replicate experiments were performed, each time using a fresh bacterial culture (each culture was assayed over all shear rates).

Images were analyzed using BacTrack, an in-house cell-tracking Java software developed by Scott Stransky (see Appendix for tracking algorithm and Sekora 2005 for full documentation of BacTrack). BacTrack locates bacteria in each image and track them among two consecutive images (Fig. 4-8c) through a search radius: the maximum distance a bacterium can move between successive frames. Since bacteria were also advected by the flow, different search radius was used for different shear rates. The search radius for each shear rate was determined by adding the corresponding flow speed at $y = -H/4$ with 100 μm s^{-1} and multiply by the time between two frames (8.2 ms). Given the locations of bacteria in each frame obtained through BacTrack, we can calculate the swimming velocity and the net drift velocity through by dividing the distance (displacement) over time between successive frames.

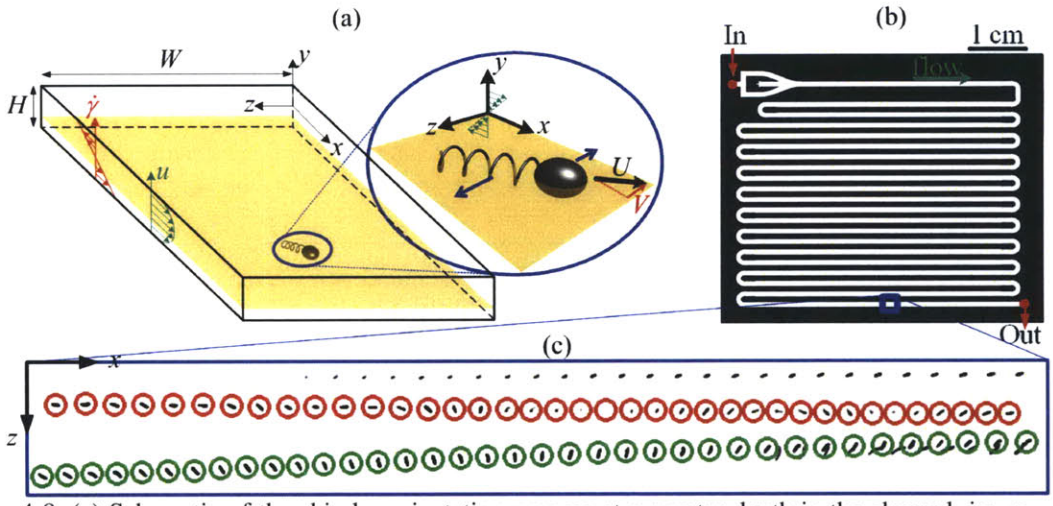

Figure 4-8. (a) Schematic of the chiral reorientation process at a quarter depth in the channel, i.e. $y = -H/4$, for a left-handed flagellum. The microchannel had width W = 1 mm, height H = 90 μm. (b) Microchannel design showing inlet and outlet. Note that only one inlet was used in this experiment. The square refers to the location of data collection and was located 110 cm downstream of the inlet. (c) Two sample trajectories of *B. subtilis* bacteria in a shear flow, imaged at $y = -H/4$. The center of the colored circles corresponds to the locations obtained by the image processing routine.

4.3.2 Experimental results and discussion

Experiments performed at a quarter depth from the bottom, $y = -H/4$, revealed (i) a clear and reproducible net drift velocity in the $-z$ direction, and (ii) a monotonic increase of the absolute drift velocity with increasing shear rates (Fig. 4-9). Both features are in agreement with the theoretical prediction. Also in agreement with theory is the magnitude of the drift velocity, which is of the same order as the swimming speed, with V/U reaching 9% at a shear rate of 10 s^{-1} and 22% at 36 s^{-1}.

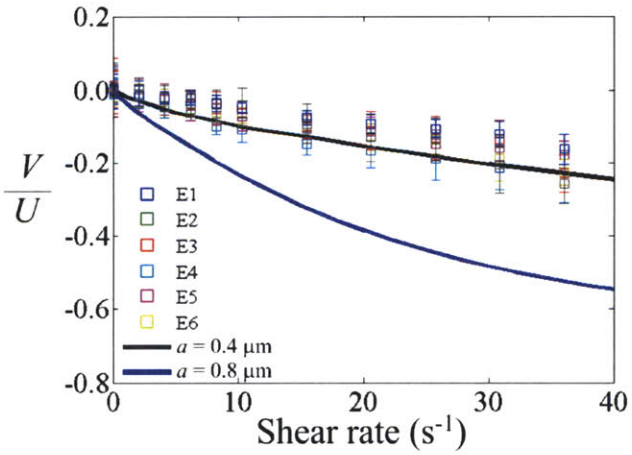

Figure 4-9. Net drift velocity of *B. subtilis* OI4139 under various shear rates at $y = -H/4$, normalized by the mean average swimming speed U = 55 μm s^{-1}. Each set of colored squares indicates a separate batch of bacteria. Six replicates were performed. Solid lines refer to the theoretical prediction assuming a left-handed helical flagellum with 3 turns, pitch angle of 37°, and axial length of 6 μm, and a spherical head of radius 0.4 μm (black line) and 0.8 μm (blue line).

To further verify that the drift was due to chiral reorientation, a separate set of experiments was conducted at a quarter depth form the top, $y = H/4$. Since the shear rate has the same magnitude but opposite sign compared to the depth $y = -H/4$, theory predicts that the net drift at $y = H/4$ should be equal in magnitude but opposite in sign to that observed at $y = -H/4$. These experiments showed that indeed the net drift velocity at both $y = -H/4$ and $y = H/4$ increase in magnitude with increasing shear rate, that they have the same magnitude, and that they of opposite sign (Fig. 4-10). This provides strong confirmation of the predicted mechanism.

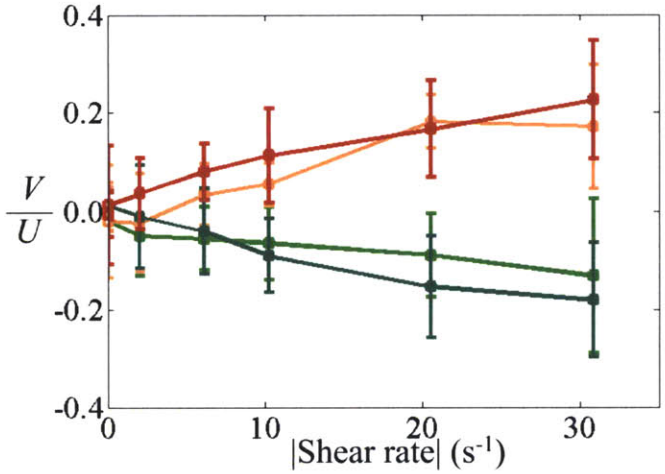

Figure 4-10. Net drift velocity of *B. subtilis* OI4139 under various shear rates at $y = H/4$ and $y = -H/4$, normalized by the mean average swimming speed $U = 55$ μm s^{-1}. Since the shear rates between the top and bottom layer are opposite in sign, we present the absolute values of the shear rate. Two separate sets of experiments (light and dark colors) were conducted at $y = H/4$ (red) and $y = -H/4$ (green). For each case, two replicates were performed. The two experiments at $y = -H/4$ were performed in addition to the ones shown in Fig. 4-9.

B. subtilis has a prolate ellipsoidal body with average size of 1×3 μm. To determine the equivalent spherical radius, we can match the average linear and torsional resistive coefficients between an ellipsoid and a sphere. The linear resistive coefficients parallel and perpendicular to the ellipsoid's major axis are given by (Steinberger et al. 1994):

$$\zeta_{ell}^{L//} = \frac{16\pi\mu}{q_0 + a_{ell}^2 \alpha_0} \qquad \zeta_{ell}^{L\perp} = \frac{16\pi\mu}{q_0 + \beta_0 b_{ell}^2} \tag{4.18}$$

where $q_0 = -\frac{1}{e_{ell}} \ln \frac{a_{ell} - e_{ell}}{a_{ell} + e_{ell}}$

The torsional resistive coefficients are given by:

$$\zeta_{ell}^{T//} = \frac{16\pi\mu}{3\beta_0} \qquad \zeta_{ell}^{T\perp} = \frac{16\pi\mu\left(b_{ell}^2 + a_{ell}^2\right)}{3\left(b_{ell}^2 \beta_0 + a_{ell}^2 \alpha_0\right)} \tag{4.19}$$

where α_0 and β_0 are given by Eq. (4.11)

The average linear resistance $\zeta_{ell}^{L,avg}$ and torsional resistance $\zeta_{ell}^{T,avg}$ over all orientations can be computed as (Berg 1993)

$$\frac{3}{\zeta_{ell}^{L,avg}} = \left(\frac{1}{\zeta_{ell}^{L//}} + \frac{2}{\zeta_{ell}^{L\perp}} \right) \qquad \frac{3}{\zeta_{ell}^{T,avg}} = \left(\frac{1}{\zeta_{ell}^{T//}} + \frac{2}{\zeta_{ell}^{T\perp}} \right) \tag{4.20}$$

Recall that the linear and torsional resistances for a sphere are $C_F = 6\pi\mu a$ and $C_M = 8\pi\mu a^3$, respectively. For a 1×3 ellipsoid, by matching $C_F = \zeta_{ell}^{L,avg}$, the equivalent spherical radius is 0.807 μm. By matching $C_M = \zeta_{ell}^{T,avg}$, we obtain 0.8023 μm. Both conditions give an equivalent spherical radius close to 0.8 μm. Using a spherical head of 0.8 μm radius (Fig 4-9, blue line), the model predicts a larger net drift velocity than what observed in the experiments. It should be noted that the 0.8 μm equivalent radius was obtained by performing a resistance average over the three principal directions (i.e. by assuming that bacterial motion in all directions is equally likely). However, not all directions are equally likely, because bacteria tend to swim along their longitudinal axis. Therefore, one might expect that an equivalent sphere radius close to the minor axis of the ellipsoid (0.5 μm) would be more appropriate to model the head. It turns out that a smaller equivalent spherical head (0.4 μm) was required to be in good agreement with the experiments (Fig. 4-9, black line).

Figure 4-11. Swimming trajectory of *B. subtilis* OI4139 in the absence of flow. Several trajectories show a helical pattern, visualized as a sinusoidal path when viewed from the top.

The discrepancy could be caused by the fact that the trajectories of *B. subtilis* are not straight. Experimental trajectories clearly show that *B. subtilis* performs a helical swimming trajectory, which we shall refer to here as "wiggle" (Fig. 4-11). In a top view, the wiggle appears as a side-to-side oscillation superimposed on otherwise nearly straight swimming segments. These wiggles have been known for a long time for *E. coli* (Berg

2004; Darnton et al. 2007). The wiggle is important in the present context because it could increase the effective rotational diffusivity or decrease the preferential alignment, thus reducing chiral reorientation. However, one should note that this wiggling motion is not random, because the motion is generated by the offset of the flagellar bundle relative to the cell body axis (Darnton et al. 2007). To study the effect of this wiggle on the net drift velocity, we present a new model incorporating the wiggle-dynamics in the next section (section 4.4).

4.4 Modeling cell head elongation and "wiggling"

In addition to *B. subtilis* observed in this experiment, wiggling has also been observed in *E. coli* (Darnton et. al. 2007) and likely in many other species, since perfect alignment between the flagellar bundle and the body axis is unlikely. In general, the cell body is not a sphere and the flagellar bundle does not form exactly at the end-tip of the cell body. In addition, the bundle axis could be at an angle relative to the cell body's major axis. In this section, we will develop a model to incorporate the body elongation and the offset of flagellar bundle relative to the cell body axis.

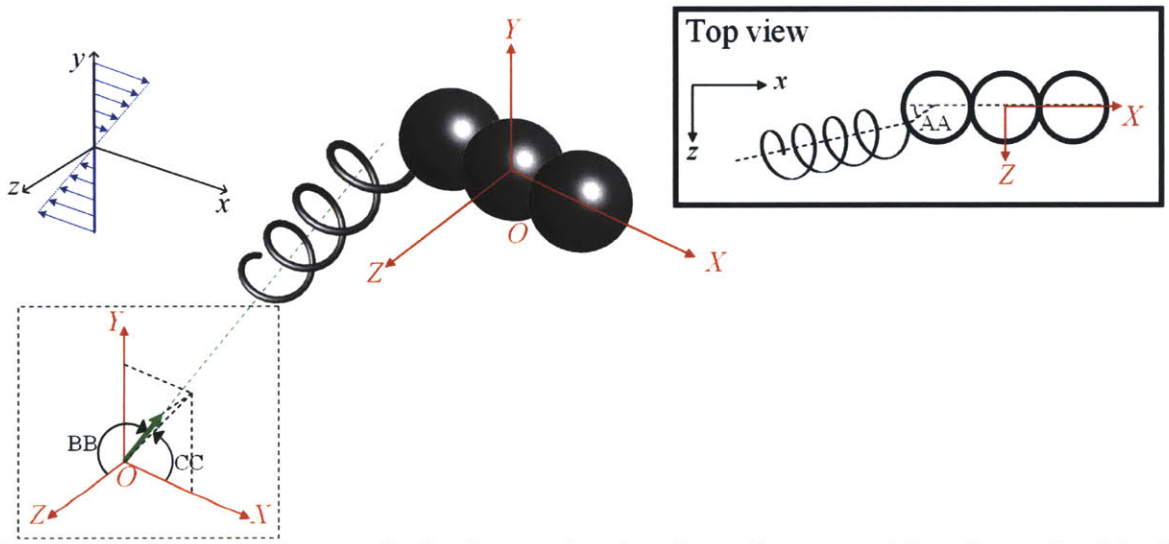

Figure 4-12. Schematic of a generalized swimmers, based on three spheres to model an elongated cell head and on an off-axis flagellar bundle, which induces wiggling. Angle AA denotes the contact point between cell body and the flagellar bundle. Lower inset: Angles BB and CC are the polar and azimuthal angles of the flagellar bundle (thick green arrow) relative to the cell body (body fixed frame *OXYZ*).

For simplicity, we model an elongated cell body as multiple spheres connected in series. Since the average aspect ratio of *B. subtilis* is 1:3, we use three identical spheres connected to one another, as shown in Fig. 4-12. The orientation of the cell body in the inertial frame is determined by the Euler angle rotation matrix $[T_{Euler}]$ (See Fig. 3-3). Three additional angles (AA, BB, and CC) are required to generally define the offset location and orientation of the flagellar bundle relative to the cell body (Fig. 4-12). Angle AA sets the location where the bundle forms. BB and CC are the polar and azimuthal angles determining the orientation of the flagellar bundle relative to the cell body axis (Fig. 4-12).

When AA = 0, the contact point is at the end-tip of the cell body. Also, when AA = 0, there is only one degree of freedom to determine the offset angle (i.e. either BB or CC is needed to determine the off-axis angle).

We shall choose the center of the cell head (i.e. the center of the middle sphere) as the location where we calculate the linear and angular velocities of the bacterium. The dynamics of a swimming bacterium in a shear flow can be obtained by adding the total forces and torques on the helix and the spheres and equating them to zero, as done before (see sections 3.1 and 4.1). The total hydrodynamic forces and torques due to the shear flow on a sphere of radius a and on a helix are given by Eqs. (4.1) and (3.12), respectively. The linear and angular velocities in those equations are computed at the center of the sphere and the helix, respectively. Therefore, we need to calculate the corresponding resistance and shear contribution matrices of the helix and the other two spheres at the center of the middle sphere. This can be obtained by employing Eq. (4.6) (following the identical procedure presented in section 4-1):

$$\{\zeta\} = \begin{pmatrix} 1 & 0 \\ -\Delta\mathbf{r}_{helix}\times & 1 \end{pmatrix}\{\zeta'\}\begin{pmatrix} 1 & \Delta\mathbf{r}_{helix}\times \\ 0 & 1 \end{pmatrix} \qquad \{A\} = \begin{pmatrix} 1 & 0 \\ -\Delta\mathbf{r}_{helix}\times & 1 \end{pmatrix}\{A'\}$$

$$\{\xi\}_{sph\_front/back} = \begin{pmatrix} 1 & 0 \\ -\Delta\mathbf{r}_{sph\_front/back}\times & 1 \end{pmatrix}\{\xi'\}\begin{pmatrix} 1 & \Delta\mathbf{r}_{sph\_front/back}\times \\ 0 & 1 \end{pmatrix}$$

$$\{B\}_{sph\_front/back} = \begin{pmatrix} 1 & 0 \\ -\Delta\mathbf{r}_{sph\_front/back}\times & 1 \end{pmatrix}\{B'\} \tag{4.21}$$

The distance measured from the center of the middle sphere $\Delta\mathbf{r}$ for the helix and the two spheres are given by:

$$\Delta\mathbf{r}_{helix} = [T_{Euler}]^{tr}\{[T_{CC}]^{tr}[T_{BB}]^{tr}(l\cos(\alpha)/2, 0, 0) + [T_{AA}]^{tr}(a, 0, 0) + (2a, 0, 0)\} \tag{4.22}$$

$$\Delta\mathbf{r}_{sph\_front} = [T_{Euler}]^{tr}(-2a, 0, 0) \qquad \Delta\mathbf{r}_{sph\_back} = [T_{Euler}]^{tr}(2a, 0, 0) \tag{4.23}$$

where

$$[T_{AA}] = \begin{bmatrix} \cos AA & 0 & -\sin AA \\ 0 & 1 & 0 \\ \sin AA & 0 & \cos AA \end{bmatrix} \qquad [T_{BB}] = \begin{bmatrix} \cos BB & 0 & -\sin BB \\ 0 & 1 & 0 \\ \sin BB & 0 & \cos BB \end{bmatrix}$$

$$[T_{CC}] = \begin{bmatrix} \cos CC & \sin CC & 0 \\ -\sin CC & \cos CC & 0 \\ 0 & 0 & 1 \end{bmatrix} \tag{4.24}$$

After obtaining the resistance matrices $\{\zeta\}$, $\{\xi_{sph\_front}\}$, $\{\xi_{sph\_mid}\}$, and $\{\xi_{sph\_back}\}$ and the shear contribution matrices $\{A\}$, $\{B_{sph\_front}\}$, $\{B_{sph\_mid}\}$, and $\{B_{sph\_back}\}$, we calculate the total forces and torques on the assembly and equate them to zero.

$$\begin{pmatrix}\mathbf{F}\\ \mathbf{M}\end{pmatrix}_{helix}+\begin{pmatrix}\mathbf{F}\\ \mathbf{M}\end{pmatrix}_{sph\_front}+\begin{pmatrix}\mathbf{F}\\ \mathbf{M}\end{pmatrix}_{sph\_mid}+\begin{pmatrix}\mathbf{F}\\ \mathbf{M}\end{pmatrix}_{sph\_back}=0 \tag{4.25}$$

We apply the following kinematic boundary conditions, expressing the fact that the flagellum is moving together with the head and the flagellum is rotating along its axis relative to the head:

$$\begin{pmatrix}\mathbf{v}\\ \boldsymbol{\omega}\end{pmatrix}_{sph\_front}=\begin{pmatrix}\mathbf{v}\\ \boldsymbol{\omega}\end{pmatrix}_{sph\_back}=\begin{pmatrix}\mathbf{v}\\ \boldsymbol{\omega}\end{pmatrix}_{sph\_mid}=\begin{pmatrix}\mathbf{v}\\ \boldsymbol{\omega}\end{pmatrix}_{head} \tag{4.26}$$

$$\begin{pmatrix}\mathbf{v}\\ \boldsymbol{\omega}\end{pmatrix}_{helix}=\begin{pmatrix}\mathbf{v}\\ \boldsymbol{\omega}\end{pmatrix}_{head}+\begin{pmatrix}0\\ \boldsymbol{\omega}\end{pmatrix}_{rel} \tag{4.27}$$

where $\boldsymbol{\omega}_{rel} = [T_{Euler}]^{tr}\,[T_{CC}]^{tr}\,[T_{BB}]^{tr}\,(0,\,0,\,\omega_{rel})$ is the angular rotation rate of the flagellum relative to the cell body along the axis of the flagella.

After putting everything together and simplifying by combining the resistance matrices of the head into one matrix $\{\zeta\}$ and similarly for the shear contribution matrices into $\{B\}$, Eq. (4.25) becomes

$$\{\zeta\}\left[\begin{pmatrix}\mathbf{v}\\ \boldsymbol{\omega}\end{pmatrix}_{head}+\begin{pmatrix}0\\ \boldsymbol{\omega}\end{pmatrix}_{rel}\right]+\{A\}+\{\xi\}\begin{pmatrix}\mathbf{v}\\ \boldsymbol{\omega}\end{pmatrix}_{head}+\{B\}=0$$

where

$$\{\xi\}=\{\xi\}_{sph\_front}+\{\xi\}_{sph\_mid}+\{\xi\}_{sph\_back}$$

and

$$\{B\}=\{B\}_{sph\_front}+\{B\}_{sph\_mid}+\{B\}_{sph\_back}$$

We can now solve for the linear and angular velocities of the head:

$$\begin{pmatrix}\mathbf{v}\\ \boldsymbol{\omega}\end{pmatrix}_{head}=-\left[\{\zeta\}+\{\xi\}\right]^{-1}\{\zeta\}\begin{pmatrix}0\\ \boldsymbol{\omega}\end{pmatrix}_{rel}-\left[\{\zeta\}+\{\xi\}\right]^{-1}\left[\{A\}+\{B\}\right] \tag{4.28}$$

Because of the off-axis position of the flagellar bundle, one expects a wiggle in the swimming trajectories. To test this, I conducted a simulation tracking the position and orientation of a single bacterium by setting AA=CC=0 and BB=18°, in the absence of shear flow and Brownian motion (Fig. 4-13). As expected, the model produces a helical trajectory, which appears as a sinusoidal path when viewed from the top, in general agreement with the experimental observations (Fig. 4-11). However, using this parameter, the pitch length and the radius of the helical trajectory predicted by the model (1 μm pitch length and 0.4 μm radius) are smaller than those observed in the experiment (4 μm pitch length and 1 μm radius). It turns out that for the parameters of the cell head and flagellar

bundle used in this model (3 spheres of radius 0.5 μm and a left-handed helical flagellum with 3 turns, pitch angle of 37°, and axial length of 6 μm), no combination of offset angles AA, BB, and CC would be able to give a helical trajectory with 4 μm pitch length and 1 μm radius. This suggests that other aspects of the physics are absent in the model. In fact, recently, it was shown that *B. subtilis* could form two flagellar bundle (personal communication with Martin Li, University of Edinburgh). This aspect is not explored in this thesis. Here, we would first like to investigate if wiggle swimming has an effect on the drift velocity.

Using the new model, we first quantify the effect of cell head elongation on the net drift velocity, in the absence of wiggling (i.e. without offset or misalignment in the flagellar bundle, or AA = BB = CC = 0). This model is compared to the earlier, simpler model of a single spherical head. As discussed above, a 1×3 μm ellipsoid has nearly exactly the same mean drag (both translational and rotational) as a 0.8 μm radius sphere. One might expect that an elongated cell body would give rise to more alignment and thus a stronger chiral reorientation, in turn yielding a larger drift velocity. However, the model shows that the two configurations are in good agreement (Fig. 4-14), confirming that a single sphere is a good approximation of an elongated cell head as long as the resistive coefficients are matched. This is not unexpected, because the forces and the torques acting on the body between the two configurations becomes nearly the same.

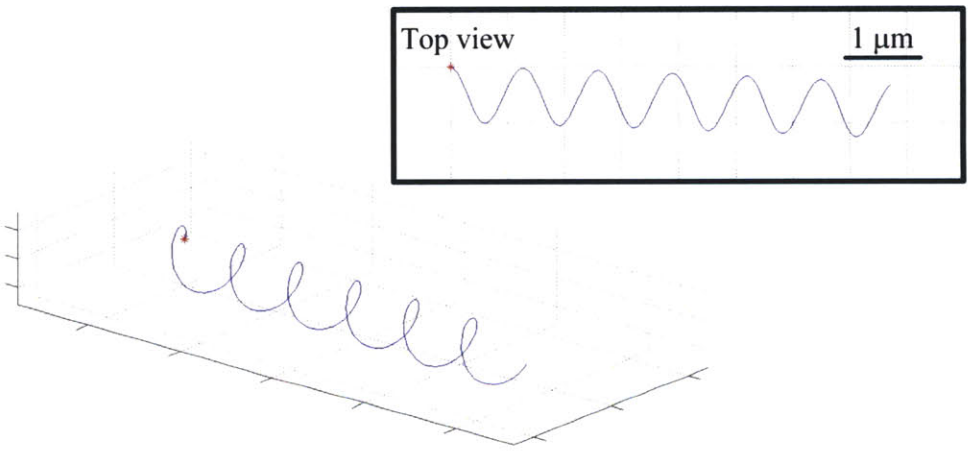

Figure 4-13. Wiggling in the trajectory of a swimming bacterium in the absence of flow. The ellipsoid represents the cell head of the bacterium. The flagellar bundle is offset relative to the cell body axis by 18°. The red point shows the initial position of the bacterium at the start of the simulation and the solid line shows that trajectory of the center of the middle sphere. The inset shows the trajectory as viewed from the top. The model assumes a left-handed helical flagellum with 3 turns, pitch angle of 37°, and axial length of 6 μm, corresponding to *B. subtilis* flagellar bundle and a cell head made of three spherical heads of radius 0.5 μm. The three angles determining the flagella bundle offset are AA = CC = 0 and BB = 18°. Brownian motion was neglected in this simulation.

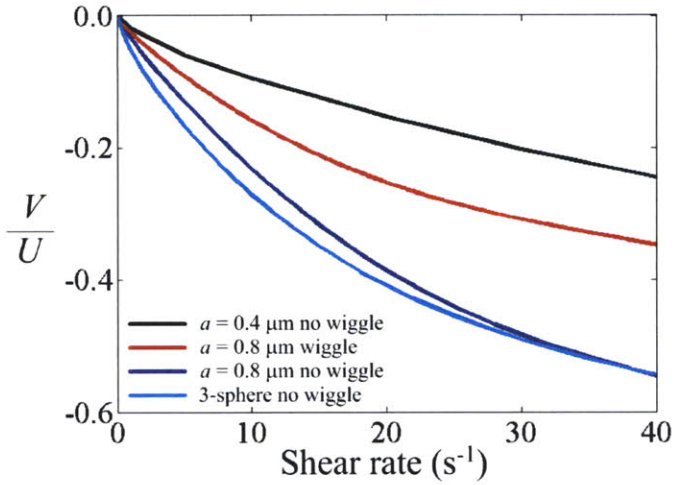

Figure 4-14. Effects of elongation and wiggle on the net drift velocity. The model assumes a left-handed helical flagellum with 3 turns, pitch angle of 37°, and axial length of 6 μm. The black line shows the theoretical prediction that agrees well with the experimental data (see Fig. 4-9). The 3-sphere model was calculated using 3 identical spheres of radius 0.5 μm (cyan). The three angles determining the flagellar bundle offset are AA = CC = 0 and BB = 5° (red).

When we introduce a small offset angle between the body axis and the flagellar bundle (AA = CC = 0, BB = 5°), we see that the net drift velocity decreases significantly (Fig. 4-14, red line). Although the helical trajectory produced by these offset parameters do not match the pitch and radius measured in the experiments, it is clear that wiggle has an equivalent effect in reducing the preferential alignment, thus reducing chiral reorientation. This model proves that wiggling induces a decrease the net drift velocity.

4.5 Bacteria active response to shear

Given that shear is prevalent in many bacterial habitats, one is led to hypothesize that bacterial might have adapted to life in shear. One potential adaptation would be the ability to tune motility depending on flow conditions, for example to conserve energy by shutting down motility at high shear rates. Results in the previous sections have shown that shear can markedly impair swimming, implying a potential waste of propulsion energy for organisms swimming in flow. The ability to adapt motility to flow conditions, however, implies the capability of measuring shear. Larger organisms, including copepods (Strickler and Bal 1973) have been shown to possess the ability to sense velocity gradients, yet nothing is known in this respect regarding bacteria. Whereas we know that bacteria can very accurately sense chemical gradients, nothing is known about their ability to sense velocity gradients. Here, we investigate for the first time whether bacteria can sense velocity gradient, by conducting a dedicated set of experiments to measure whether motility changes in response to shear.

To test this, we have designed and carried out novel experiments to determine if bacteria change swimming behavior (in particular, speed) after being exposed to high shear. We investigated four different bacterial strains from different natural environments: *Escherichia coli* (human gut), *Pseudoalteromonas haloplanktis* (coastal ocean),

Pseudomonas aeruginosa (soil and human respiratory system), and *Bacillus subtilis* (soil). We use the microchannel set-up described in section 4.2, which we filled with a suspension of bacteria before the onset of the experiments. We begin by recording a movie at a location close to the inlet, at a quarter depth from the bottom (y = -H/4). We then expose bacteria to a shear flow having a mean shear 500 s^{-1} for 9 minutes using a programmable syringe pump (PHD 2000 Programmable, Harvard Apparatus, Holliston, MA). Since we are probing motility changes in response to shear, we are only interested in the mean value of shear, instead of the precise shear value at a given location. Shear rate of 500 s^{-1} is small enough to keep the Reynolds number of the bacteria below unity (Re = $\dot{\gamma}L^2/\nu = 0.05$, using characteristic length of a bacterium including its flagella L = 10 μm), but much larger than typical shear rates experienced in their natural habitat. Imposing them to large shear rates would ensure their response if they are able to sense velocity gradient. Due to the finite length of the microchannel, we program the syringe pump to alternate between the "infuse" and "refill" mode, so that the same bacteria are retained in the microchannel. Alternating between these two modes would alternate the flow directions and thus the sign of shear. However, here, we are only interested in the magnitude of the shear and not the sign. We then acquired movies every 10 s for 300 s, and analyzed them to quantify swimming speed. This was done first by locating and tracking the positions of bacteria using BacTrack. Given the locations in each frame, we can then calculate the speed by dividing the distance (displacement) over time between successive frames.

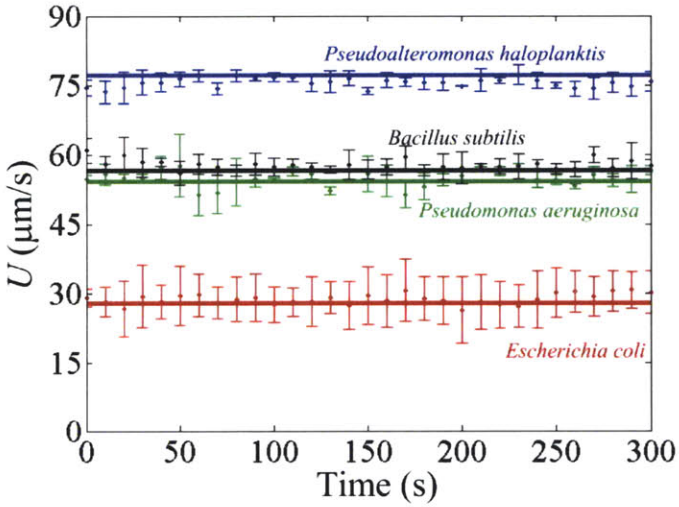

Figure 4-15. Time evolution of the mean swimming speed of a bacterial population after exposure to a shear rate of 500 s^{-1} for 9 minutes. Colors refer to *Pseudoalteromonas haloplanktis* (blue), *Bacillus subtilis* (black), *Escherichia coli* (green), and *Pseudomonas aeruginosa* (red). Solid lines refer to the values before shear exposure.

The mean swimming speeds of all bacteria probed in this experiment do not change after exposure to strong shear (Fig. 4-15). These results show that bacteria do not respond to shear by changing their motility. However, this does not conclude that bacteria are not able to sense and/or response to velocity gradient. There could be other ways they might respond that are not assayed in this experiment, for example by releasing chemical compounds, changing metabolic rate, or self-dividing (reproduction).

4.6 Summary

We presented a complete model based on resistive force theory to study the dynamics of a swimming flagellated bacterium in a simple shear flow. We discussed that the presence of the cell head results not only in a lateral drift, but also in a reorienting torque. Due to this reorientation, bacteria swim with a preferential drift perpendicular to the shear plane. We showed that the magnitude of the drift velocity is in the same order of the swimming speed. We learned that run and tumble swimming strategy and wiggle swimming behaviour reduce the net drift velocity. Experiments by exposing motile soil bacteria *Bacillus subtilis* in microfluidic shear flows reveal a good agreement with the theoretical prediction. Finally, further experiments suggest that bacteria do not actively respond to shear, which confirms that the chiral reorientation process is a purely passive hydrodynamic effect.

The current theoretical model could be improved. We are not able to match the helical trajectories observed in the experiments. One could pursue modeling two flagellar bundles and investigate a set of offset angles that would give helical trajectory that matches the observation.

Chapter 5

Summary and conclusion

This thesis explored the coupling between bacterial motility and ambient fluid flow. In chapter 2, we presented a microfluidic setup to generate vortices on scales relevant to microbial movement, while at the same time tracking responses of individual swimming microorganisms. We illustrated the ability of the setup to yield quantitative single-cell information on the behaviour of microbes exposed to a recirculating shear flow. We applied this setup to the marine bacterium *P. haloplanktis* and the marine alga *D. tertiolecta*. The experiments suggest that bacteria will be mostly advected and aligned in a turbulent flow, whereas motile algae can overcome mild turbulence levels. Furthermore, the experiments also suggest that *P. haloplanktis* swimming trajectories are not affected under typical turbulent conditions in the open ocean, whereas their trajectories are significantly aligned with the flow under coastal ocean and breaking waves turbulence.

Since most natural flow fields are experienced simply as shear by bacteria, we developed a mathematical model to study the microhydrodynamics of a flagellated bacterium in a simple shear flow. We studied the hydrodynamics of the head and the flagellum separately, neglecting the interactions between the two. In chapter 3, we presented the dynamics of a helix in a simple shear flow and found that the helix drifts across streamlines due to its chiral morphology. We verified this prediction by exposing a strain of non-motile helical bacteria, *Leptospira biflexa flaB* mutant, to a plane parabolic shear flow. Experiments showed that the drift velocity was in good agreement with that computed from the model. The residual discrepancy might be associated with the flexibility of the spirochetes and irregularities in their geometry, which could be explored in future investigations. We discussed the application of such a microfluidic setup in separation processes of chiral particles, which are relevant to agricultural and pharmaceutical industries.

After understanding the physics of a helix in shear, we discussed the dynamics of a swimming flagellated bacterium in a simple shear flow in chapter 4 through modeling and experiments. We showed that the presence of the cell head results in a reorienting torque. This causes bacteria to swim at an angle to the shear plane. Our model predicted that the streamline crossing velocity (the average velocity perpendicular to the streamline) is of the same order as the swimming speed. We learned that a run and tumble swimming strategy and the off-axis orientation of the flagellar bundle cause a 'wiggle' in the swimming trajectories, reducing the streamline crossing velocity. Experiments in which smooth swimming *Bacillus subtilis* bacteria were exposed to microfluidic shear flows gave good agreement with the theoretical prediction. The wiggling trajectory produced by the theoretical model matched the experiments qualitatively. However, we were not able to produce a trajectory that matches the observations. Improvements to the model, such as the incorporation of two flagellar bundles (recently observed at the University of Edinburgh; Martin Li, pers. comm.), could reduce the discrepancy. Further experiments suggest that

bacteria do not actively respond to shear, confirming that the observations regarding chiral reorientation are a purely passive hydrodynamic effect.

This thesis provides a fundamental understanding of the hydrodynamic effects of shear on swimming bacteria. Our findings contribute to our understanding of bacterial transport in the natural environment. Since we expect that this hydrodynamic reorientation can significantly affect chemotaxis, it is important to understand under what environmental conditions chiral reorientation affects chemotactic motility. For example, one could study the dispersion of a bacterial population through direct numerical simulations (DNS) by coupling realistic flow fields (e.g. turbulence in the ocean or groundwater flow in soil) with the microhydrodynamic effect of chiral reorientation.

Our understanding of the effects of flow on swimming bacteria is far from comprehensive and there is ample scope for future work. While the model has successfully been validated against experiments, there are still discrepancies between the theory and observations. The model presented here is based on a rigid body assumption, whereas in reality cells can be flexible. The interaction between the external forces due to a shear flow and the elastic flagellum could change the shape of the bacteria (Kim and Powers 2005). Furthermore, recent work reveals that *B. subtlis* can form two flagellar bundles (Martin Li, pers. comm.). A theoretical model incorporating cell elasticity and/or two flagellar bundles could potentially resolve the discrepancy between the experimental observations and the current model.

In addition, the present study is limited to a shear flow away from a surface. The behavior of bacteria near surfaces is a fundamental determining factor in biofilm formation, where cell attachment occurs mostly under flow conditions. When shear flows occur near boundaries, the additional hydrodynamic effects of the wall on motility must be accounted for. In the presence of shear, *E. coli* was observed to preferentially swim upstream in a microfluidic channel (Hill et al. 2007). However, our understanding of how shear at boundaries affects swimming and attachment is primitive at best. One could study this by extending the current model based on resistive force theory to incorporate boundary effects, by making the resistive force coefficients a function of the distance from the boundary.

The calculation of instantaneous dynamics, demonstrated in this work, is only a first step towards understanding chemotactic behavior. Although previous work (Bowen et al. 1993; Luchsinger et al. 1999; Bearon and Pedley 2000; Bearon 2003; Locsei and Pedley 2008) has demonstrated an effect of shear on chemotaxis, the interaction of the shear flow with the chiral morphology of bacterial flagella was not included in the analysis. Experimentally, one could study bacterial chemotaxis in shear flow using a microfluidic setup that can generate shear flows and steady linear concentration gradients (see Ahmed et al. 2010a), to determine whether shear hinders or favors chemotaxis.

Bibliography

Ahmed, T., T. S. Shimizu, and R. Stocker. 2010a. Bacterial chemotaxis in linear and nonlinear steady microfluidic gradients. Nano Lett. 10: 3379-3385.

Ahmed, T., T. S. Shimizu, and R. Stocker. 2010b. Microfluidics for bacterial chemotaxis. Integr. Biol. 2, 604-629.

Ahuja, S. 1997. Chiral Separations: Applications and Technology (American Chemical Society, Washington, DC).

Azam, F. 1998. Microbial control of oceanic carbon flux: The plot thickens. Science 280: 694-696.

Barbara, G. M. and J. G. Mitchell. 2003. Marine bacterial organisation around point-like sources of amino acids. Fems Microbiol. Ecol. 43:99–109.

Bearon, R. N. 2003. An extension of generalized Taylor dispersion in unbounded homogeneous shear flows to run-and-tumble chemotactic bacteria. Phys. Fluids, 15:1552–1563.

Bearon, R. N. and T. J. Pedley. 2000. Modelling run-and-tumble chemotaxis in a shear flow. Bull. Math. Biol. 62:775–791.

Berg, H. C. 1993. Random Walks in Biology. Princeton University Press, Princeton, New Jersey.

Berg, H. C. 2004. E. coli in Motion. Springer-Verlag, New York.

Berg, H. C., D. A. Brown. 1972. Chemotaxis in Escherichia coli analysed by threedimensional tracking. Nature 239: 500–504.

Blackburn, N., T. Fenchel, and J. Mitchell. 1998. Microscale nutrient patches in planktonic habitats shown by chemotactic bacteria. Science 282: 2254-2256.

Bowen, J. D., K. D. Stolzenbach, and S. W. Chisholm. 1993. Simulating bacterial clustering around phytoplankton cells in a turbulent ocean. Limnol. Oceanogr. 38: 36-51.

Bray, D. 2001. Cell Movements: From Molecules to Motility, 2nd ed. Garland Publishing, Inc., New York.

Brennen, C. and H. Winet. 1977. Fluid mechanics of propulsion by cilia and flagella Annu. Rev. Fluid Mech. 9:339-98.

Brenner, H. 1964. The Stokes resistance of an arbitrary particle-III. Chem. Eng. Sci. 19: 631-651.

Bretherton, F. P. and L. Rothschild. 1961. Rheotaxis of Spermatozoa. Proc. R. Soc. Lond. B. 153: 490-502.

Chen, P. and C.-H. Chao. 2007. Lift forces of screws in shear flows. Phys. Fluids 19: 017108.

Childress, S. 1981. Mechanics of swimming and flying. Cambridge University Press, Cambridge.

Cho, B. S., T. G. Schuster, X. Zhu, D. Chang, G. D. Smith, and S. Takayama. 2003. Passively driven integrated microfluidic system for separation of motile sperm. Anal. Chem. 75: 1671-1675.

Crittenden, J. C., R. R. Trussell, D. W. Hand, K. J. Howe, and G. Tchobanoglous. 2005. Water Treatment - Principles and Design (2nd Edition). John Wiley & Sons, Hoboken, New Jersey.

Darnton, N. C., L. Turner, S. Rojevsky, and H. C. Berg. 2007. On torque and tumbling in swimming *Escherichia coli*. J. Bacteriol. 189: 1756-1764.

Davidson, P. A. 2004. Turbulence: An introduction for Scientists and Engineers. Oxford University Press, New York.

De Gennes, P. G. 1999. Mechanical selection of chiral crystals. Europhys. Lett. 46: 827-831.

Di Carlo, D., D. Irimia, R. G. Tompkins, and M. Toner. 2007. Continuous inertial focusing, ordering, and separation of particles in microchannels. Proc. Natl. Acad. Sci. U.S.A. 104: 18892-18897.

DiLuzio, W. R., L., Turner, M. Mayer, P. Garstecki, D. B. Weibel, H. C. Berg, and G. M. Whitesides. 2005. Escherichia coli swim on the right-hand side. Nature 435: 1271-1274.

Doshi, M. R., P. M. Daiya, and W. N. Gill. 1978. Three dimensional laminar dispersion in open and closed rectangular conduits. Chem. Eng. Sci, 33:795-804.

Eggersdorfer, B. and D. P. Hader. 1991. Phototaxis, gravitaxis and vertical migrations in the marine dinoflagellate prorocentrum-micans. FEMS Microbiol. Ecol. 85: 319-326.

Fujii, M., S. Shibata, and S.-I. Aizawa. 2008. Polar, peritrichous, and lateral flagella belong to three distinguishable flagellar families. J. Mol. Biol. 379: 273-283.

Gray, J. and G. J. Hancock. 1955. The propulsion of sea-urchin spermatozoa. J. Exp. Biol. 21: 802-814.

Hancock, G. J. 1953. The self-propulsion of microscopic organisms through liquids. Proc. R. Soc. Lond. A. 217: 96-121.

Happel, J. and H. Brenner. 1965. Low Reynolds Number Hydrodynamics. Prentice-Hall, Englewood Cliffs, NJ.

Higdon, J. J. L. 1985. Stokes flow in arbitrary two-dimensional domains: shear flow over ridges and cavities. J. Fluid Mech. 159: 195-226.

Hill, J., O. Kalkanci, J. L. McMurry, and H. Koser. 2007. Hydrodynamic surface interactions enable *Escherichia coli* to seek efficient routes to swim upstream. Phys. Rev. Lett. 98: 068101.

Howard, D.W., E. N. Lightfoot, and J. O. Hirschfelder. 1976. The Hydrodynamic Resolution of Optical Isomers. AIChE J. 22: 794-798.

Howell, P. B., D. R. Mott, J. P. Golden, and F. S. Ligler. 2004. Design and evaluation of a Dean vortex-based micromixer. Lab Chip 4: 663-669.

Hui, Y. H. 2006. Handbook of food science, technology, and engineering volume 2. CRC Press, Boca Raton, FL.

Jeffery, G. B. 1922. The motion of ellipsoidal particles immersed in a viscous fluid. Proc. R. Soc. Lond. 102: 161-179.

Kang, K., L. J. Lee, and K.W. Koelling. 2005. High shear microfluidics and its application in rheological measurement. Exp. Fluids 38: 222-232.

Karp-Boss, L., E. Boss, and P. A. Jumars. 1996. Nutrient fluxes to planktonic osmotrophs in the presence of fluid motion. Oceanogr. Mar. Biol., Ann. Rev. 34: 71-107.

Karp-Boss, L., E. Boss, and P. A. Jumars. 2000. Motion of dinoflagellates in a simple shear flow. Limnol. Oceanogr. 45: 1594-1602.

Kessler, J. O. 1985. Hydrodynamic focusing of motile algal cells. Nature 313: 218.

Kim, M.-J. and T. R. Powers. 2005. Deformation of a helical filament by flow and electric or magnetic fields. Phys. Rev. E. 71: 021914.

Kim, Y.-J. and W. J. Rae. 1991. Separation of screw-sensed particles in a homogeneous shear field. Int. J. Multiphase Flow 17: 717-744.

Kiørboe, T. and G. A. Jackson. 2001. Marine snow, organic solute plumes, and optimal chemosensory behavior of bacteria. Limnol. Oceanogr. 46: 1309-1318.

Kostur, M., M. Schindler, P. Talkner, and P. Hänggi. 2006. Chiral separation in microflows. Phys. Rev. Lett. 96: 014502.

Kozu, H., I. Kobayashi, M. Nakajima, K. Uemura, S. Sato, and S. Ichikawa. 2010. Analysis of flow phenomena in gastric contents induced by human gastric peristalsis using CFD. Food Biophys. 5: 330-336.

Kunze, E., J. F. Dower, I. Beveridge, R. Dewey, and K. P. Bartlett. 2006. Observations of biologically generated turbulence in a coastal inlet. Science 313: 1768-1770.

Lauga, E., W. R. DiLuzio, G. M. Whitesides, and H. A. Stone. 2006. Swimming in circles: motion of bacteria near solid boundaries. Biophys. J. 90: 400-412.

Lauga, E. and T. R Powers. 2009. The hydrodynamics of swimming microorganisms. Rep. Prog. Phys. 72: 096601.

Lazier, J. R. N. and K. H. Mann. 1989. Turbulence and the diffusive layers around small organism. Deep-Sea Res. 36: 1721-1733.

Liu, R. H., M. A. Stremler, K. V. Sharp, M. G. Olsen, J. G. Santiago, R. J. Adrian, H. Aref, and D. J. Beebe. 2000. Passive mixing in a three-dimensional serpentine microchannel. J. Microelectromech. Syst. 9: 190-197.

Locsei, J. T. and T. J. Pedley. 2009. Run and tumble chemotaxis in a shear flow: the effect of temporal comparisons, persistence, rotational diffusion, and cell shape. Bull. Math. Biol. 71: 1089-1116.

Luchsinger, R. H., B. Bergersen, and J. G. Mitchell. 1999. Bacterial swimming strategies and turbulence. Biophys. J. 77: 2377-2386.

MacIntyre, S., K. M. Flynn, R. Jellision, and J. R. Romero. 1999. Boundary mixing and nutrient fluxes in Mono Lake, California. Limnol. Oceanogr. 44: 512–529.

MacIntyre, S., J. R. Romero, and G. W. Kling. 2002. Spatial–temporal variability in the surface layer deepening in an embayment of Lake Victoria, East Africa. Limnol. Oceanogr. 47: 656–671.

Marcos, H. C. Fu, T. R. Powers, and R. Stocker. 2009. Phys. Rev. Lett. 102: 158103.

Marcos and R. Stocker. 2006. Limnol. Oceanogr.: Methods, 4:392–398.

Makino, M., L. Arai, and M. Doi. 2008. Shear Migration of Chiral Particle in Parallel-Disk. J. Phys. Soc. Jpn. 77: 064404.

Makino, M. and M. Doi. 2005. Migration of twisted ribbon-like particles in simple shear flow. Phys. Fluids 17: 103605.

Mead, K. S. and M. W. Denny. 1995. The effects of hydrodynamic shear stress on fertilization and early development of the purple sea urchin *Strongylocentrotus purpuratus*. Biol. Bull. 188: 46-56.

Meinhart, C. D., S. T. Wereley, and M. H. B. Gray. 2000. Volume illumination for two-dimensional particle image velocimetry. Meas. Sci. Technol. 11: 809-814.

Park, T. H. and M. L. Shuler. 2003. Integration of cell culture and microfabrication technology. Biotechnol. Prog. 19: 243-253.

Picardeau, M., A. Brenot, and I. S. Girons. 2001. First evidence for gene replacement in *Leptospira* spp. Inactivation of *L. biflexa flaB* results in non-motile mutants deficient in endoflagella. Mol. Microbiol., 40: 189-199.

Purcell, E. M. 1977. Life at Low Reynolds Number. Am. J. Phys. 45: 3-11.

Ramia, M., D. L. Tullock, and N. Phan-Thien. 1993. The role of hydrodynamic interaction in the locomotion of microorganisms. Biophys. J. 65:755–778.

Riffel, J. A. and Zimmer, R. K. 2007. Sex and flow: the consequences of fluid shear for sperm–egg interactions. J. Exp. Biol. 210: 3644-3660.

Rothschild, B. J. and T. R. Osborn. 1988. Small-scale turbulence and plankton contact rates. J. Plankton Res. 10: 465-474.

Scriba, G. K. E. 2008. Cyclodextrins in capillary electrophoresis enantioseparations – Recent developments and applications. J. Sep. Sci. 31: 1991-2011.

Sekora, M. D. 2005. Tactic behaviors in bacterial dynamics. Thesis (S. B.), Massachusetts Institute of Technology, Cambridge, MA.

Seymour, J. R., Marcos, and Stocker, R. 2007. Chemotactic response of marine micro-organisms to micro-scale nutrient layers. J. Visualized Exp., 4th issue: http://www.jove.com/Details.htm?ID=203&VID=175.

Seymour, J. R., J. G. Mitchell, L. Pearson, and R. Waters. 2000. Heterogeneity in bacterioplankton abundance from 4.5 millimetre resolution sampling. Aquat. Microb. Ecol. 22:143-153.

Shelby, J. P., D. S. W. Lim, J. S. Kuo, and D. T. Chiu. 2003. High radial acceleration in microvortices. Nature 425: 38.

Sjoblad, R. D., I. Chet, and R. Mitchell. 1978. Quantitative assay for algal chemotaxis. Appl. Environ. Microbiol. 36: 847-850.

Shen, C. and J. M. Floryan. 1985. Low Reynolds number flow over cavities. Phys. Fluids 28: 3191-3202.

Steinberger, B., N. Petersen, H. Petermann, and D. G. Weiss. 1994. Movement of magnetic bacteria in time-varying magnetic fields. J. Fluid Mech. 273: 189-211.

Stocker, R., J. R. Seymour, A. Samadani, D. E. Hunt, and M. F. Polz. 2008. Rapid chemotactic response enables marine bacteria to exploit ephemeral microscale nutrient patches. Proc. Natl. Acad. Sci. U.S.A. 105: 4209-4214.

Strickler, J.R., and A. L. Bal. 1973. Setae of the first antennae of the copepod Cyclops scutifer (Sars): their structure and importance. Proc. Nat. Acad. Sci. USA, 70: 2656-2659.

Stroock, A. D., S. K. W. Dertinger, A. Ajari, I. Mezić, H. A. Stone, and G. M. Whitesides. 2002. Chaotic mixer for microchannels. Science 295: 647-651.

Sudarsan, A. P. and V. M. Ugaz. 2006. Multivortex micromixing. Proc. Nat. Acad. Sci. USA, 103: 7228-7233.

Szurmant, H., T. Muff, and G. W. Ordal. 2004. *Bacillus subtilis* CheC and FliY Are Members of a Novel Class of CheY-P-hydrolyzing Proteins in the Chemotactic Signal Transduction Cascade. J. Biol. Chem. 279: 21787-21792.

Trevelyan, B. J. and S. G. Mason. 1951. Particle motions in sheared suspensions. I. Rotations. J. Col. Sci. 6: 354-367.

Visser, A. W. and Jonnson, P. R. 2000. On the reorientation of non-spherical prey particles in a feeding current. J. Plankton Res. 22: 761-777.

Weeks, B. S. and I. E. Alcamo. 2008. Microbes and Society. Jones and Bartlett Publishers, Sudbury, MA.

Wheelis, M. 2008. Principles of Modern Microbiology. Jones and Bartlett Publishers, Sudbury, MA.

Whitesides, G. M., E. Ostuni, S. Takayama, X. Jiang, and D. E. Ingber. 2001. Soft Lithography in biology and biochemistry. Annu. Rev. Biomed. Eng. 3: 335-373.

Willey, J. M., L. M. Sherwood, and C. J. Woolverton. 2008. Prescott, Harley, and Klein's Microbiology 7th ed. McGraw-Hill, New York, NY.

Wolgemuth, C.W., N.W. Charon, S. F. Goldstein, and R. E. Goldstein. 2006. The flagellar cytoskeleton of the spirochetes. J. Mol. Microbiol. Biotechnol. 11: 221-227

Yamazaki, H., D. L. Mackas, and K. L. Denman. 2002. Coupling small-scale physical processes with biology. The Sea 12: 51-112.

Yu, Z. T. F., Y.-K. Lee, M. Wong, and Y. Zohar. 2005. Fluid flows in microchannels with cavities. J. Microelectromech. Syst. 14: 1386-1398.

Zimmer, M. A., Szurmant, H., Saulmon, M. M., Collins, M. A., Bant, J. S., and Ordal, G. W. 2002. The role of heterologous receptors in McpB-mediated signalling in *Bacillus subtilis* chemotaxis. Mol. Microbiol. 45: 555–568.

Appendix

Growth media recipe for *Pseudoalteromonas haloplanktis*

1% TSB (1 L)
10 grams of TSB
25 grams of NaCl
1L of mQ water
Autoclave before use.

Glycerol Stocks
20% glycerol final concentration

Growth Protocol
Inoculate 1:10 (from glycerol stock) in the growth media at room temperature with shaking at 150 rpm for 15 hours.

Growth Media recipe for *Leptospira biflexa* (modified from Current Protocols in Microbiology) Current Protocols in Microbiology (2007) 12E.4.1-12E.4.12

Albumin supplement (200 mL)
Dissolve 10 g Bovine Serum Albumin (BSA) into 50 mL distilled water with stirring (~30 min). Add the following:
1 mL 1.5% (w/v) $MgCl_2.6H_2O$
1 mL 0.4% (w/v) $ZnSO_4.7H_2O$
1 mL 1.5% (w/v) $CaCl_2.2H_2O$
1 mL 0.02% (w/v) vitaimin B12
1 mL 10% (w/v) pyruvic acid (prepared from sodium salt)
0.4 g glycerol (~0.4 mL)
1.25 g Tween 80 (~1.25 mL)
Adjust final volume to 100 mL with H_2O
Sterilize by filtration through a 0.22-μm filter
Store indefinitely at -20°C

EMJH, base (1.6 L)
1.8 g Na_2HPO_4
0.54 g KH_2PO_4
1.8 g NaCl
0.45 g NH_4Cl
0.009 g thiamine chloride
Add H_2O to 1.6 L

EMJH liquid medium (1 L)
800 mL EMJH base
100 mL albumin supplement (see recipe above)
100 mL 0.5% (w/v) $FeSO_4.7\ H_2O$ to final concentration of 0.05% (w/v)
Adjust pH to 7.4 with NaOH or HCl as necessary
Sterilize by filtration through a 0.22-μm filter
Divide into aliquots as needed for experiments
Store up to 2 months at 4°C

Glycerol Stocks
5% glycerol final concentration

Growth Protocol
Inoculate 1:10 (from glycerol stock) in EMJH liquid medium at 30°C with shaking at 80 rpm for 3 to 4 days.

Minimal Media Growing Protocol for *Bacillus subtilis*

1. Streak out cells o/n on a TBAB plate, grow overnight at 30 C.
2. Start 5ml day culture in Cap Assay Minimal (CAM) with a starting $OD_{600} = 0.030$.
   (add 1mM IPTG for smooth swimming strain OI4139)
   Scrape the cells off the plate, and re-suspend them in 500 µL of CAM. Take the OD_{600} of the cell suspension, and dilute them so that the final concentration in the 5 mL culture is at an $OD_{600} = 0.030$.
3. Grow until $OD_{600} = 0.40$ (around 5 hours) at 37 C, shaking at 250 rpm.
4. Add 50µL 5% Glycerol, 0.5M Na-lactate (filter sterilized).
5. Shake for additional 15 minutes.

Glycerol Stocks

1. Streak out cells o/n on a TBAB plate, grow overnight at 30 C.
2. Pick a single colony from the plate, and grow in a 3 mL culture of LBr for 6 hours.
3. Add 900 µL of glycerol (or 300 µL DMSO).
4. Freeze in a -80 C freezer. The stocks should be good for many years.

Solutions

Cap Assay Minimal (1L)

50mM KPO_4 (6.805 g KH_2PO_4 + 8.71 g K_2HPO_4) pH=7
1mM $MgCl_2$ (0.203 g $MgCl_2.H_2O$)
1mM NH_4SO_4
1:1000 Sporulation Salts
Autoclave
for every 20ml, add:
60µL HMT (5 mg/mL each of histidine, methionine and tryptophan, filter sterilized)
200µL TBr
200µL 1M Sorbitol (filter sterilized)

LBr

10 g Tryptone
5 g Yeast Extract
5 g NaCl
qs to 1 L water
autoautoclave

TBr

10 g Tryptone
5 g NaCl
qs to 1 L water
autoclave

Tryptose Blood Agar Plates
33 g Tryptose Blood Agar
3 g Agar
qs to 1L water
autoclave

1X Sporulation Salts
0.14M $CaCl_2$
0.01M $MnCl_2$
0.20M $MgCl_2$

BacTrack particle tracking algorithm – adopted from Sekora 2005.

Basic Rule:

1. Each child (particle in frame n+1) comes from one parent (particle in frame n).
2. Each parent begets one child.

Algorithm:

1. Locate particles in frame n (parent particles) and frame n+1 (child particles).
2. Define a cutoff radius (the search radius): R, the maximum distance an object can move between successive frames.
3. Consider all particle pairs (parent from frame n, child from frame n+1). Compute distances for all pairs. Throw out all pairs whose distance exceeds R.
4. Consider one parent particle at a time. There are three possibilities:
   - 4a. Parent has no children: when no child-particle is within the search radius of that parent (for example the particle could have gone out of focus). The trajectory ends for that parent.
   - 4b. Parent has one and only one child: when one and only one child-particle is within the search radius of that parent. In this case, one needs to check if the child could have more than one parent. There are two possibilities:
     - $4b_1$. Child has only one parent: consider this a match. The parent and the child are the same particle.
     - $4b_2$. Child has more than one parent: end the trajectory of that parent.
   - 4c. Parent has more than one child: when more than one child-particle is within the search radius of that parent. The trajectory ends for that parent. This case is analogous to $4b_2$.
5. After one cycles through all of the parents, there will be some children left without a parent. Those children are new trajectories (for examples, particles coming in focus).
6. Repeat the process for the next exposure starting from Step 2.